Valence fluctuations and disorder effects in strongly correlated electronic systems

A Thesis

Submitted For the Degree of

DOCTOR OF PHILOSOPHY

in the Faculty of Science

by

Pramod Kumar

THEORETICAL SCIENCES UNIT
JAWAHARLAL NEHRU CENTRE FOR ADVANCED SCIENTIFIC RESEARCH
Bangalore – 560 064

DECEMBER 2013

DECLARATION

I hereby declare that the matter embodied in the thesis entitled "**Valence fluctuations and disorder effects in strongly correlated electronic systems**" is the result of investigations carried out by me at the Theoretical Sciences Unit, Jawaharlal Nehru Centre for Advanced Scientific Research, Bangalore, India under the supervision of Prof. N. S. Vidhyadhiraja and that it has not been submitted elsewhere for the award of any degree or diploma.

In keeping with the general practice in reporting scientific observations, due acknowledgement has been made whenever the work described is based on the findings of other investigators.

Pramod Kumar

CERTIFICATE

I hereby certify that the matter embodied in this thesis entitled "**Valence fluctuations and disorder effects in strongly correlated electronic systems**" has been carried out by Mr. Pramod Kumar at the Theoretical Sciences Unit, Jawaharlal Nehru Centre for Advanced Scientific Research, Bangalore, India under my supervision and that it has not been submitted elsewhere for the award of any degree or diploma.

Prof. N. S. Vidhyadhiraja
(Research Supervisor)

Abstract

In this thesis, we have carried out theoretical investigations of valence fluctuations and disorder effects in strongly correlated electron systems, focusing on heavy fermion materials in particular. The theoretical framework that we have employed is that of dynamical mean field theory (DMFT), which allows the mapping of a lattice model to a self-consistently determined effective impurity problem. We have extended, implemented and applied the semi-analytical, local moment approach to solve the impurity model. The first three chapters have a common theme – namely valence fluctuations driven crossovers and transitions. The periodic Anderson model, a paradigm to understand heavy fermions in rare-earth systems, has been employed in the first chapter to study a valence crossover, and the manifestation of this crossover in optical and transport properties. A detailed comparison to DC and optical transport of several Cerium and Ytterbium based materials yields excellent agreement. The valence crossover investigated in the first chapter can be transformed to valence transitions with an additional term, i.e inter-orbital Coulomb interaction term in the PAM Hamiltonian, leading to an *extended* periodic Anderson model, that is investigated in chapter two. A valence fluctuations driven quantum critical point is found to exist in realistic parameter regimes. In order to access real systems, one must be able to deal with orbital degeneracy and inter-orbital correlations. Thus, in the third chapter, we have combined a multi-orbital

local moment approach with dynamical mean field theory to study the degenerate multi-orbital periodic Anderson model.

The second theme in the thesis is disorder effects in heavy fermions. In the fourth chapter, we have derived a Feenberg renormalised perturbation series based dynamical coherent potential approximation within the framework of dynamical mean field theory. The local moment approach has been used as an impurity solver. Our approach captures the crossover from coherent lattice to single impurity behaviour with increasing substitutional disorder. Such a crossover is, naturally, reflected in optical and transport properties. In the final chapter, we outline a new route to non-Fermi liquid behaviour in substitutionally disordered heavy fermions arising from the self averaging of impurity scattering. We have carried out a detailed analysis of such non-Fermi liquid behaviour, both analytically (in the concentrated and dilute limits), and numerically (for complete range of disorder), at low frequencies and temperatures. The relevance of our results for understanding deviations from Fermi liquid behaviour in a large range of heavy fermions and transition metal oxide materials has been pointed out.

Acknowledgements

I would first like to thank my advisor, Prof. N. S. Vidhyadhiraja, for providing great PhD problems and all the guidance throughout the process. He is great as a teacher and mentor. It has been a true privilege to have him as my advisor.

I am also thankful to Prof. H. R. Krishnamurthy, Prof. V. B. Shenoy of IISc and Prof. David Logan from University of Oxford, UK for fruitful and productive discussions. I would also like to extend my gratitude to faculty members of theoretical sciences unit, Prof. Shobhana Narasimhan, Prof. U. V. Waghmare, Prof. S. K. Pati, Prof. Subir K. Das and Dr. Kavita Jain. My graduate student friends have contributed equally to my academic and social life at JNCASR, and I would like to thank some of them: Varun, Kanchan, Sananda, and Yogi. I am thankful to my group members, especially Dasari and Himadri for wonderful scientific discussions and technical help. I acknowledge CSIR India, JNCASR, I2CAM USA, and ICTP Italy for providing generous financial support to my research.

Finally, I would like to thank my family and fiancèe Neha, for all their support during my graduate life.

Contents

List of Figures

List of acronyms

- **BL:** Bethe lattice
- **DMFT:** dynamical mean field theory
- **EPAM:** extended periodic Anderson model
- **FL:** Fermi liquid
- **FWHM:** full width at half-maximum
- **HCL:** hypercubic lattice
- **HM:** Hubbard model
- **IPT:** iterated perturbation theoery
- **LMA:** local moment approach
- **PAM:** periodic Anderson model
- **RNIL:** renormalized non-interacting limit
- **RPA:** random phase approximation

- **SB:** slave-Boson
- **SIAM:** single impurity Anderson model
- **nFL:** non-Fermi liquid

Chapter 1

Introduction

1.1 Strongly correlated systems

Strongly correlated electronic systems, whose physical properties are strongly governed by strong and local Coulomb interaction have been a subject of intense study in the field of modern condensed matter science. There are a large number of strongly correlated materials: those that exist naturally and others that can be synthesized. A few examples of such systems are transition metal oxides, heavy fermions, and artificially engineered systems like ultra-cold atoms. Heavy fermion compounds/alloys [1, 2], systems of central theme of the present thesis, have generated much interest in past two decades because of interesting physical properties like Kondo effect [3], quantum criticality [4,5], valence fluctuation driven Kondo collapse and unconventional superconductivity [6], and disorder driven non-Fermi-liquid behaviour [7,8]. These phenomena arise mainly due to the presence of strongly correlated electrons [3,9,10], that belong to partially filled, highly localized f- orbitals characterized by large ratios of Coulomb interaction to bandwidth.

Rare earth based f- heavy fermions have effective masses that are $10 - 1000$

times the bare electron mass. The specific heat coefficient, which is inversely proportional to effective mass ($\gamma \propto 1/m*$), of a few heavy fermion alloys e.g. $CeCu_2Si_2$, $CeCu_6$ and $CeAl_3$ are 1100 mJ/mol K^2, 1600 mJ/mol K^2 and 1620 mJ/ mol K^2 [11]. For comparison, the specific heat coefficient of Copper, a conventional normal metal, is 1 mJ/mol K^2. The other important class of rare earth based intermetallic systems are Kondo insulators. A few examples are $Ce_3Bi_4Pt_3$, SmB_6, YbB_{12} and CeRhAs [9, 12, 13]. These materials have a characteristic low energy scale that coincides with the excitation gap and is proportional to the Kondo scale $(10 - 100K)$. The emergence of a low energy scale in these kind of systems is widely believed to be due to screening of localised f- moments in the lattice by itinerant conduction electrons [3]. These materials show various interesting emergent physical phenomena at low temperatures as a direct result of screening of f-moments by electrons in the conduction orbitals. The low temperature resistivity of heavy fermions increases with decrease in temperature reaching a coherence peak (proportional to Kondo scale) and subsequently decreases with further decrease in temperature. The magnetic susceptibility follows the Curie-Weiss law ($\chi(T) = \frac{C}{T+\theta}$) at high temperatures, while the low temperature behaviour is Pauli like. One of the very important features of these systems is adiabatic continuity. To illustrate this concept, we can focus on the DC resistivity of $CeAl_3$ below 0.3K [14] which displays a T^2 form and is hence similar to Copper [15]. The only difference is coefficient of resistivity, which is larger for $CeAl_3$ by three orders of magnitude than Copper. The above observation leads to the conclusion that physical laws obeyed by weakly correlated materials can be equally valid for strongly correlated systems, but with a renormalization factor. In order to understand the various complex phenomena in strongly correlated electronic systems, microscopic model Hamiltonians are studied, which we will discuss in next section.

1.2 Microscopic model Hamiltonians

The periodic Anderson model (PAM) is one of the simplest models representing a paradigm for understanding the physics of heavy-fermion compounds. In standard notation, the Hamiltonian for the PAM is given by

$$\hat{H} = \epsilon_c \sum_{i\sigma} c^\dagger_{i\sigma} c_{i\sigma} - t \sum_{(i,j),\sigma} (c^\dagger_{i\sigma} c_{j\sigma} + \text{h.c.}) + V \sum_{i\sigma} (f^\dagger_{i\sigma} c_{i\sigma} + \text{h.c.}) + \sum_{i\sigma} \left(\epsilon_f + \frac{U}{2} f^\dagger_{i\bar{\sigma}} f_{i\bar{\sigma}} \right) f^\dagger_{i\sigma} f_{i\sigma} \tag{1.1}$$

The first two terms describe the c-orbital energy (ϵ_c) and the kinetic energy of the conduction band arising from nearest neighbour hopping t, which is scaled as $t \propto \frac{t^*}{\sqrt{Z_c}}$ (t^* is the unit of energy) in the large dimension limit where the coordination number $Z_c \to \infty$. We choose the hyper cubic lattice in our calculations, for which the non-interacting density of states is given by $\rho_0(\epsilon) = \exp(-\epsilon^2/t_*^2)/t_*\sqrt{\pi}$ is an unbounded Gaussian [16]. The hybridization between the c- and f- electrons is represented by the third term (V) and is responsible for making otherwise localised f- electrons itinerant. The last term is f- orbital site energy (ϵ_f) and the on-site Coulomb repulsion U for two f- electrons of opposite spin. We can define an asymmetry parameter $\eta = 1+2\epsilon_f/U$. The system is in particle-hole symmetric limit for $\epsilon_c = 0$ and $\eta = 0$ and has Kondo insulating ground state ($n_f+n_c = 2$ with $n_f = 1$ and $n_c = 1$ ($n_f = \sum_\sigma \langle f^\dagger_{i\sigma} f_{i\sigma} \rangle$ and $n_c = \sum_\sigma \langle c^\dagger_{i\sigma} c_{i\sigma} \rangle$)). A finite value of either $\epsilon_c = 0$ and η introduces asymmetry. For $\epsilon_c \neq 0$ and $\eta \sim 0$, the system is in Kondo lattice regime, while for $\epsilon_c \neq 0$ and $\eta \sim 1$, the system would be in the mixed valent metallic regime. We will return to the PAM shortly and discuss other important details about the model. But before that, we will discuss another fundamental model, namely the single impurity Anderson model (SIAM) [17], required to understand

the dilute and high temperature regimes ($T > T_K$) of heavy fermions. The SIAM can be expressed in standard second quantization notation as

$$\hat{H} = \sum_{\mathbf{k},\sigma} \epsilon_{\mathbf{k}} c^{\dagger}_{\mathbf{k}\sigma} c_{\mathbf{k}\sigma} + V \sum_{\mathbf{k}\sigma} (f^{\dagger}_{\sigma} c_{\mathbf{k}\sigma} + H.c.) + \sum_{\sigma} (\epsilon_f + \frac{U}{2} f^{\dagger}_{\bar{\sigma}} f_{\bar{\sigma}}) f^{\dagger}_{\sigma} f_{\sigma} \tag{1.2}$$

where the first term is a conduction band with dispersion ϵ_k. The second term is hybridization of the impurity f- electron with the conduction band. The third term is orbital energy of impurity electrons. The last term is the on-site Coulomb repulsion between impurity f- electrons. A Schrieffer-Wolff [18] transformation of the above SIAM eliminates local charge fluctuations, and leads to the Kondo model, that can be represented as

$$\hat{H}_K = H_c + H_{ex} \equiv \sum_{\mathbf{k}\sigma} \epsilon_{\mathbf{k}} c^{\dagger}_{\mathbf{k}\sigma} c_{\mathbf{k}\sigma} + \sum_{\mathbf{k},\mathbf{k}',\alpha\beta} J(\mathbf{k},\mathbf{k}') c^{\dagger}_{\mathbf{k}\alpha} \sigma_{\alpha\beta} c_{\mathbf{k}'\beta} \cdot \mathbf{S} \tag{1.3}$$

where

$$J(\mathbf{k},\mathbf{k}') = -\frac{V^2 U}{2(\epsilon_{\mathbf{k}} - \epsilon_f)(\epsilon_{\mathbf{k}} - (\epsilon_f + U))} + \mathbf{k} \leftrightarrow \mathbf{k}' \tag{1.4}$$

and S is local impurity spin. The parameter regime $Ut_*/V^2 \gg 1, \epsilon_f < \epsilon_F$ and $\epsilon_f + U > \epsilon_F$ corresponds to the condition for local moment formation. J is the effective exchange coupling between localised spin of the impurity and the conduction electrons and is antiferromagnetic in nature (ϵ_F is the Fermi level). It has been shown from Bethe ansatz [19] and numerical renormalization group [20] that the impurity local moment gets screened at low temperatures ($T \ll$ Kondo temperature T_K). The Kondo scale is exponentially small; $T_K \propto \exp(-\alpha U/V^2)$. The screening of the local moment at $T \sim T_K$ is evident as a dip in the resistivity and saturation of susceptibility of dilute magnetic alloys with lowering the tem-

perature. For $T \gg T_K$, screening effects are washed out by thermal fluctuations and the f- moments act as free spins (so $\chi_{imp} \sim \frac{1}{T}$). The dynamics and scaling behaviour in the single impurity Anderson model is captured to great accuracy by the recently developed local moment approach (LMA) [21,22]. The details of LMA will be discussed in section 1.3. Now, we return back to the PAM and discuss our theoretical approach followed in this thesis to solve the model.

Our main aim in the thesis is to calculate single particle spectral functions, $D(\omega)$ of c- and f- electrons and subsequently the optical and transport properties in various regimes of the periodic Anderson model.

1.3 Dynamical mean field theory and local moment approach

Several theoretical approaches have been employed to solve the PAM. Some of them are – Hartree-Fock approximation [23], alloy analogy approximation [24], Gutzwiller variational approach [25], slave boson approach [26–28] etc. The periodic Anderson model has been solved exactly in one dimension only [29]. In the various theoretical techniques mentioned above, dynamical quantum fluctuations have not been incorporated. A few other popular theoretical tools for solving the PAM are dynamical mean field theory (DMFT) [16, 30], extended DMFT [31], cluster expansions [32], finite size simulations [33] etc. Within the framework of DMFT [16, 30], the self-energy becomes purely local or momentum independent, which simplifies the problem significantly, while retaining the competition between itinerancy and localization in a non-trivial way. The momentum independence of the self-energy implies that we can view lattice problems as locally self-consistent

impurity problems, hence the solution of PAM, for instance reduces to that of a SIAM with a self-consistent hybridization. The various impurity solvers that have been adapted to solve the effective impurity problem are numerical renormalization group [34], quantum Monte-Carlo [35], exact diagonalization [36], perturbation theory methods such as iterated perturbation theory [37], local moment approaches [38], and slave-particle approaches [39] etc. The Kondo lattice regime within the PAM has been investigated heavily by [22, 34, 38, 40–42] within DMFT and cluster extensions ignoring the d−f repulsion effects.

The local retarded Green's functions for f- and c- electrons within DMFT in the paramagnetic phase are given by

$$G^f(\omega;T) = \left[\omega^+ - \epsilon_f - \Sigma_f(\omega;T) - \frac{V^2}{\omega^+ - \epsilon_c - S(\omega)}\right]^{-1} \tag{1.5}$$

$$G^c(\omega;T) = \left[\omega^+ - \epsilon_c - S(\omega) - \frac{V^2}{\omega^+ - \epsilon_f - \Sigma_f(\omega;T)}\right]^{-1}. \tag{1.6}$$

The retarded self-energy $\Sigma_f(\omega;T)$ is momentum independent within DMFT. $S(\omega)$ is the Feenberg self-energy [43] and is a functional of $G^c(\omega;T)$. The mapping of PAM to SIAM within DMFT yields the following equations [38, 44]:

$$G^c(\omega;T) = H[\gamma] = \int_{-\infty}^{\infty} \frac{\rho_0(\epsilon)}{\gamma(\omega;T) - \epsilon} = \frac{1}{\gamma(\omega;T) - S(\omega)} \tag{1.7}$$

where $H[\gamma]$ denotes the Hilbert transform of γ with respect to the non-interacting density of states $\rho_0(\epsilon)$ and $\gamma(\omega;T) = \omega^+ - \epsilon_c - V^2[\omega^+ - \epsilon_f - \Sigma_f(\omega;T)]^{-1}$. Our choice of the non-interacting density of states is either a bounded semi-ellipse, appropriate for a Bethe lattice (BL), or an unbounded Gaussian, which is appropriate for a

hypercubic lattice (HCL).

$$\rho_0(\epsilon) = \begin{cases} \frac{2}{\pi t^*}\sqrt{1-\frac{\epsilon^2}{t^{*2}}} & \text{if } |\epsilon| \leq t^* \text{ ; BL} \\ \frac{1}{\sqrt{\pi}t^*}\exp(-\epsilon^2/t^{*2}) & \text{; HCL} \end{cases}$$

Given a self-energy, one can use Eq. 1.7 to find $G^c(\omega;T)$, and hence $S(\omega)$. Then from Eq. 1.5, one can get the f-Green's function as well. However, the main challenge is to obtain the self-energy. This is where DMFT plays an important role. Since the lattice model can be mapped onto an impurity model, what then remains to be solved is the effective impurity problem. Basically, a single correlated impurity is embedded in a non-interacting host that is determined self-consistently. The host is characterized by the non-interacting density of states $\rho_0(\epsilon)$ and a hybridization $\Delta(\omega) = V^2/(\omega^+ - \epsilon_c - S(\omega))$. Thus the non-interacting propagator that can be used to construct the self-energy for the impurity problem is given by the Dyson's equation:

$$\mathcal{G}(\omega) = \left[\left(G^f(\omega)\right)^{-1} + \Sigma_f(\omega)\right]^{-1} \tag{1.8}$$

$$= \left[\omega^+ - \epsilon_f - \Delta(\omega)\right]^{-1} . \tag{1.9}$$

The new self-energy thus obtained will yield a new $S(\omega)$ from Eq. 1.7 and this self-consistency cycle continues until convergence is achieved.

However, the problem is easier said than done. There is no simple and exact prescription to calculate the self-energy of a general impurity model. Exact methods are necessarily elaborate and expensive and include numerical renormalization group, exact diagonalization and quantum Monte-Carlo. There exist several semi-analytical methods based on diagrammatic perturbation theory such as fluctuation exchange, non-crossing approximation, iterated perturbation theory and local mo-

ment approach (LMA).

In this thesis, we have employed the LMA as the impurity solver within DMFT. The LMA is a quantum many-body diagrammatic perturbation theory based approach developed by Logan and co-workers [21] for the single-impurity Anderson model. This approach has been benchmarked extensively against methods such as Bethe Ansatz [21] and numerical renormalization group [45]. Excellent quantitative agreement has been found, thus providing justification for its use as an impurity solver within DMFT. Further advantages of using LMA are that, real frequency quantities are obtained directly with reasonable computational expense at all temperatures and interaction strengths.

Previously, the local moment approach(LMA) within the DMFT framework has been used to understand the PAM in the Kondo lattice (KL) limit [38, 40, 41]. The main focus in these works was on universality and scaling in dynamics and transport. A single low energy scale was found to characterize the spectra and transport in the Kondo lattice regime [38]. We will briefly discuss the local moment approach and its implementation below.

There are three key elements of LMA.

i. Local moments: In usual perturbation theories, the starting point is the non-interacting limit. However, in LMA, the starting point is the unrestricted Hartree-Fock (UHF), symmetry broken, static mean field solutions corresponding to $\mu = \pm|\mu|$ and denoted as 'A'/'B' respectively. Thus, the propagators used to construct the self-energy will be

$$\mathcal{G}_{\alpha\sigma}(\omega) = \left[\omega^{+} - \epsilon_i + \alpha\sigma x - \frac{V^2}{\omega^{+} - \epsilon_c - S(\omega)}\right]^{-1} \tag{1.10}$$

where $\alpha = +1$ (for 'A' type solution ($\mu = |\mu|$)) or -1 (for 'B' type solution

$(\mu = -|\mu|)$), $\epsilon_i = \epsilon_f + U\bar{n}_f/2$ and $x = U|\bar{\mu}|/2$.

At the mean-field level, the average occupancy and local moment are found by

$$\bar{n}_f = \int_{-\infty}^{0} d\omega \left[\mathcal{D}_{A\uparrow}(\omega) + \mathcal{D}^{f/c}_{A\downarrow}(\omega)\right] \tag{1.11}$$

$$|\bar{\mu}| = \int_{-\infty}^{0} d\omega \left[\mathcal{D}^{f}_{A\uparrow}(\omega) - \mathcal{D}^{f}_{A\downarrow}(\omega)\right] \tag{1.12}$$

where $\mathcal{D}_{\alpha\sigma}(\omega) = -\frac{1}{\pi}\mathrm{Im}\mathcal{G}_{\alpha\sigma}(\omega)$. In the absence of a magnetic field, the following symmetry holds: $\mathcal{G}_{A\sigma}(\omega) = \mathcal{G}_{B\bar{\sigma}}(\omega)$. Since, we can always find the quantities corresponding to the 'B' solution by this symmetry, we will drop this 'pseudo-spin' index and work with only the 'A' solutions.

ii. Two self-energy description: The broken symmetry starting point necessitates a two-self-energy description. The LMA builds two self-energies corresponding to each of the two UHF symmetry broken mean-field solutions. The self-energies are constructed diagrammatically from the mean field propagators given by Eq. 1.10. In practice, the diagrams that are chosen to describe the Kondo effect are those that represent spin-flip processes to all orders. The transverse spin polarization propagator is constructed by a random phase approximation sum of the bare polarization bubble in the particle-hole channel, and is given by

$$\Pi^{\sigma-\sigma}(\omega) = \frac{{}^{0}\Pi^{\sigma-\sigma}(\omega)}{1 - U\,{}^{0}\Pi^{\sigma-\sigma}(\omega)}, \tag{1.13}$$

where the bare bubble is given by

$${}^{0}\Pi^{\sigma-\sigma}(\omega) = i\int_{-\infty}^{\infty} \frac{d\omega_1}{2\pi}\mathcal{G}^{T}_{-\sigma}(\omega_1)\mathcal{G}^{T}_{\sigma}(\omega_1 - \omega)\,, \tag{1.14}$$

and $\mathcal{G}^{T}_{\sigma}(\omega)$ is the time ordered counterpart of $\mathcal{G}_{\sigma}$ given in Eq. 1.10. In prac-

tice, we calculate the imaginary part of retarded *bare* polarisation $\mathrm{Im}^0\Pi^{\sigma-\sigma}(\omega)$ propagator as follows:

$$\frac{1}{\pi}\mathrm{Im}^0\Pi^{\sigma-\sigma}(\omega) = \int_{-\infty}^{\infty} d\omega_1\, \mathcal{D}_{\downarrow}(\omega_1)\mathcal{D}_{\uparrow}(\omega_1-\omega)\left[\theta(\omega_1-\omega)-\theta(\omega_1)\right]\,, \qquad (1.15)$$

where $\mathcal{D}_\sigma(\omega) = -\frac{1}{\pi}\mathrm{Im}\mathcal{G}_\sigma(\omega)$. The real part is calculated using Kramers-Kronig transformation as a principal value integral:

$$\mathrm{Re}^0\Pi^{\sigma-\sigma}(\omega) = -\mathcal{P}\int_{-\infty}^{\infty} d\omega_1 \frac{\mathrm{Im}^0\Pi^{\sigma-\sigma}(\omega_1)}{\omega-\omega_1}\,. \qquad (1.16)$$

The ${}^0\Pi^{\sigma-\sigma}(\omega)$ found in this way is converted to a time-ordered form simply by multiplying the imaginary part by $\mathrm{sgn}(\omega)$, and then used in Eq. (1.13)to get the RPA sum. The resulting $\Pi^{\sigma-\sigma}(\omega)$ is time-ordered, and thus, its imaginary part is positive-definite. This is then used in finding the imaginary part of the retarded part of the self-energy as follows.

The retarded self-energy within LMA can be written as sum of static and dynamical parts as [21]

$$\tilde{\Sigma}_\sigma(\omega) = \frac{U\bar{n}}{2} - \sigma\frac{U|\bar{\mu}|}{2} + \Sigma_\sigma(\omega). \qquad (1.17)$$

The dynamical part of the retarded self-energy in the Eq. (1.17) is given by

$$\Sigma_\sigma(\omega) = U^2\int_{-\infty}^{\infty}\frac{d\omega_1}{2\pi i}\mathcal{G}_{-\sigma}(\omega-\omega_1)\Pi^{\sigma\,-\sigma}(\omega_1). \qquad (1.18)$$

In practice, we calculate the imaginary part of the retarded self-energy, which

can be written as follows

$$\frac{1}{\pi}\mathrm{Im}\Sigma_\sigma(\omega) = -U^2 \int_{-\infty}^{\infty} d\omega_1 \; [\theta(-\omega_1)\theta(\omega+\omega_1) + \theta(\omega_1)\theta(-\omega-\omega_1)] \\ \mathcal{D}_{\bar{\sigma}}(\omega+\omega_1)\mathrm{Im}\Pi^{\sigma\bar{\sigma}}(\omega_1)\,. \tag{1.19}$$

Using the Kramers-Kronig transformation, we can finally find the real part of retarded self-energy.

iii. Symmetry restoration at zero temperature: The static mean field solutions are known to break adiabatic continuity to the non-interacting limit. However, once the dynamics is built in using the two self-energy prescription, a self-consistent restoration of broken symmetry, inherent at mean field level, can be carried out. The local moment μ is taken as a free parameter and is found using the symmetry restoration condition (for a derivation, please see Ref. [21]):

$$\mathrm{Re}\Sigma_\uparrow(0) - \mathrm{Re}\Sigma_\downarrow(0) = U|\bar{\mu}|. \tag{1.20}$$

The two-self-energy description can now be connected back to the usual single-self-energy description as follows. The spin-dependent c-Green's functions are given by

$$G^c_\sigma(\omega) = \frac{1}{\gamma_\sigma(\omega) - S(\omega)} \tag{1.21}$$

where $\gamma_\sigma(\omega) = \omega^+ - \epsilon_c - V^2/[\omega^+ - \epsilon_f - \tilde{\Sigma}_\sigma(\omega)]$. By summing the spin-dependent Green's functions to get the full $G^c(\omega)$ and using Eqs. 1.6 and 1.7, we get

$$\gamma(\omega;T) = \frac{2\gamma_\uparrow(\omega;T)\gamma_\downarrow(\omega;T) - S(\omega)\left(\gamma_\uparrow(\omega;T) + \gamma_\downarrow(\omega;T)\right)}{\gamma_\uparrow(\omega;T) + \gamma_\downarrow(\omega;T) - 2S(\omega)}\,. \tag{1.22}$$

This allows us to obtain the single self-energy $\Sigma_f(\omega)$ as

$$\Sigma_f(\omega) = \omega^+ - \epsilon_f - \frac{V^2}{\omega^+ - \epsilon_c - \gamma(\omega)}\,. \tag{1.23}$$

Finally, using Eq. 1.5, we can also find the f-Green's function. For a Fermi liquid, the Luttinger's integral theorem given by

$$I_L(\epsilon_i; x) = \mathrm{Im}\int_{-\infty}^{0} \frac{d\omega}{\pi}\frac{\partial\Sigma_f(\omega)}{\partial\omega}G^f(\omega) = 0. \tag{1.24}$$

needs to be satisfied explicitly in general, except for the p-h symmetric case, where it is automatically satisfied. Thus, the ϵ_i in the bare propagators Eq. 1.10 is taken to be an unknown parameter to be found by satisfying the Luttinger's theorem.

Next, we discuss briefly the finite temperature LMA implementation which has been discussed in detail in [46] and [47]. At finite temperature, the imaginary part of bare polarisation propagator (Eq. (1.11)) modifies to

$$\mathrm{Im}^0\Pi_{AA}^{\sigma-\sigma}(\omega^+, T) = \int_{-\infty}^{\infty} d\omega_1 \mathcal{D}_{\downarrow}(\omega_1)\mathcal{D}_{\uparrow}(\omega_1 - \omega)[n_F(\omega_1 - \omega) - n_F(\omega_1)] \tag{1.25}$$

where $n_F(\omega) = (1 + \exp(\beta\omega))^{-1}$ is the Fermi function and $\beta = 1/T$ is the inverse temperature. Finally, the imaginary part of self-energy (Eq. (1.19)) at finite temperature gets modified as follows:

$$\begin{aligned}\mathrm{Im}\Sigma_\sigma(\omega^+, T) = &-U^2\int_{-\infty}^{0} d\omega_1\,\mathrm{Im}\Pi^{\sigma-\sigma}(\omega_1; T)\mathcal{D}_{-\sigma}(\omega_1 + \omega)\left[1 - n_F(\omega_1 + \omega; T)\right] \\ &-U^2\int_{0}^{\infty} d\omega_1\,\mathrm{Im}\Pi^{\sigma-\sigma}(\omega_1; T)\mathcal{D}_{-\sigma}(\omega_1 + \omega)\left[n_F(\omega_1 + \omega; T)\right]\,.\end{aligned} \tag{1.26}$$

One important point to mention here is that symmetry restoration condition is satisfied solely at zero temperature. Numerical implementation of LMA is carried

out at zero temperature (T=0) and symmetry restoration condition is satisfied. Zero temperature converged data is used for finite temperatures.

1.4 Transport

Since within DMFT, vertex corrections are absent [16], the single-particle Green's functions are sufficient within the Kubo formalism to obtain transport quantities such as DC resistivity and optical conductivity. The expressions have been derived previously [40]. The expression for the real part of optical conductivity is given by

$$\sigma(\omega;T) = \frac{\sigma_0}{2\pi^2}\int_{-\infty}^{\infty} d\omega\, \frac{n_F(\omega) - n_F(\omega+\omega)}{\omega} \\ \mathrm{Re}\left[\frac{G_c^*(\omega) - G_c(\omega+\omega)}{\gamma(\omega+\omega) - \gamma^*(\omega)} - \frac{G_c(\omega) - G_c(\omega+\omega)}{\gamma(\omega+\omega) - \gamma(\omega)}\right] \tag{1.27}$$

where $\sigma_0 = 4\pi e^2 t^2 a^2 n/\hbar$ for lattice constant a, electronic charge e, and electron density n and $\gamma(\omega) = S(\omega) - \frac{1}{G_c(\omega)}$.

By carrying out a Kramers-Kronig transform of the $\sigma(\omega;T)$ we can get $\sigma'(\omega;T)$, and then the complex optical conductivity, $\bar{\sigma}(\omega;T)$, can be obtained as $\sigma(\omega;T) + i\sigma'(\omega;T)$. The optical scattering rate [48] is defined as $M^{-1}(\omega;T) = \mathrm{Re}(1/\bar{\sigma}(\omega;T))$. The explicit expression for DC conductivity and thermopower coefficient are obtained by considering the $\omega \to 0$ limit of the above equation and can be written as

$$\sigma_{DC} = \int_{-\infty}^{\infty} d\omega \left(-\frac{dn_F}{d\omega}\right)\tau(\omega) \tag{1.28}$$

$$Q_{DC} = \frac{Q_0}{T\sigma_{DC}}\int_{-\infty}^{\infty} d\omega\, \omega \left(-\frac{dn_F}{d\omega}\right)\tau(\omega) \tag{1.29}$$

where $Q_0 = -\frac{1}{e}$; $\tau(\omega) = \frac{\sigma_0}{2\pi^2}\mathrm{Re}[\frac{\pi D_c(\omega)}{\mathrm{Im}\gamma(\omega)} + 2(1-\gamma(\omega)G_c(\omega)]$ and $D_c(\omega) = -\mathrm{Im}G_c(\omega)/\pi$

is the spectral function of the retarded $c-$Green's function $G_c(\omega)$.

1.5 Thesis overview

The thesis has been divided into five chapters with two broad themes. Chapters one to three deal with valence fluctuations and chapters four and five focus on disorder effects in heavy fermions. The five chapters are summarized below.

Many heavy fermion materials are known to crossover from the Kondo lattice regime to the mixed valence regime or vice versa as a function of pressure or doping. In the first chapter, we study this crossover theoretically by employing the periodic Anderson model within the framework of the dynamical mean field theory. Changes occurring in the dynamics and transport across this crossover are highlighted. As the valence is decreased (increased) relative to the Kondo lattice regime, the Kondo resonance broadens significantly, while the lower (upper) Hubbard band moves closer to the Fermi level. The resistivity develops a two peak structure in the mixed valence regime: a low temperature coherence peak and a high temperature Hubbard band peak. These two peaks merge, yielding a broad soft maximum upon decreasing the valence further. The optical conductivity likewise exhibits an unusual absorption feature (shoulder) in the deep mid-infrared region, which grows in intensity with decreasing valence. The involvement of the Hubbard bands in DC transport and of the effective f-level in the optical conductivity are shown to be responsible for the anomalous transport properties. A two-band hybridization-gap model, which neglects incoherent effects due to many-body scattering, commonly employed to understand the optical response in these materials is shown to be inadequate, especially in the mixed valence regime. Comparison of theory with experiment carried out for (a) DC resistivities of $CeRhIn_5$, $Ce_2Ni_3Si_5$, $CeFeGe_3$

and $YbIr_2Si_2$, (b) pressure dependent resistivity of $YbInAu_2$ and $CeCu_6$, and (c) optical conductivity measurements in $YbIr_2Si_2$ yields excellent agreement.

Novel quantum criticality driven by valence fluctuations has been proposed as the explanation for the experimental observations in certain materials such as $CeCu_2Si_2$ and $YbRh_2Si_2$. The minimal periodic Anderson model is unable to account for valence transitions. Hence, in third chapter, we investigate the extended periodic Anderson model (EPAM), which includes a Coulomb repulsion (U_{fc}) between conduction (c) and localised electrons (f), using a static mean-field as well as the local moment approach (LMA) within dynamical mean field theory (DMFT). Our objective is to develop an understanding of quantum phase transitions due to valence fluctuations. We show that, in specific parameter regimes of the EPAM, a quantum critical point (QCP) governed by valence fluctuations exists. The signature of this novel QCP is a divergence of the valence susceptibility at a critical U_{fc}, unaccompanied by a vanishing of the Fermi liquid scale.

The dynamics of f- orbitals and conduction bands in heavy fermions is usually represented by a single non-degenerate orbital hybridizing with a single conduction band in the periodic Anderson model Hamiltonian. However, the real f- orbital is highly degenerate, and hence multi-orbital effects must be properly accounted. In chapter three, we have embedded a multi-orbital extension of the local moment approach within DMFT to investigate the degenerate PAM including inter-orbital correlations. In parallel to the multi-orbital single-impurity case, we find two low energy scales, corresponding to intra and inter-orbital correlations. We focus on the signatures of these two scales in spectra and transport, and highlight the differences with the single-orbital case.

In the fourth chapter, we have investigated the effect of Kondo-hole type sub-

stitutional disorder on the dynamics and transport properties of heavy fermion systems. We employ the periodic Anderson model within the framework of coherent potential approximation and dynamical mean field theory. The crossover from lattice coherent behaviour to an incoherent single-impurity behaviour is reflected in all aspects: a highly frequency (ω) dependent hybridization becomes almost flat; the coherence peak in resistivity (per impurity) gives way to a Hammann form that saturates at low temperature (T); the Drude peak and the mid-infrared peak in the optical conductivity vanish almost completely. The zero temperature resistivity can be captured in a closed form expression, and we show how the Nordheims rule gets strongly modified in these systems. The thermopower changes sign with increasing disorder, and exhibits a characteristic peak for all disorder values. The location of this peak is shown to correspond to the low energy scale of the system ω_L. In fact, the thermopower appears to be much more sensitive to disorder variations than the resistivity. A comparison to experiments yields quantitative agreement.

The last chapter deals with the interplay of disorder and interactions, as in the previous chapter, but with a strong focus on the low temperature and low frequency features in single-particle quantities and response functions. The formalism remains the same as in the previous chapter, namely coherent potential approximation (CPA) and dynamical mean field theory. An exact low frequency analysis of the equations for CPA self-energy in the concentrated and dilute limits shows that the dynamical local potentials arising through disorder averaging generate a linear (in frequency) term in the scattering rate. Such non-Fermi liquid behaviour (nFL) is investigated in detail for Kondo hole substitution in heavy fermions within dynamical mean field theory. We find closed form expressions for the dependence of the static and linear terms in the scattering rate on substitutional disorder and

model parameters. We argue that the low temperature resistivity will acquire a linear in temperature term, and show that the Drude peak structure in the optical conductivity will disappear beyond a certain disorder x_c, that marks the crossover from lattice coherent to single-impurity behaviour. The analytical results thus obtained, we then carry out a full numerical solution of the DMFT equations. We found that the nFL term will show up significantly only in certain regimes, although it is present for any non-zero disorder concentration in principle. We highlight the dramatic changes that occur in the quasiparticle scattering rate in the proximity of x_c. Remarkably, we find that the nFL behaviour due to dynamical effects of impurity scattering has features that are distinct from those arising through Griffiths singularities or distribution of Kondo scales. Relevance of our findings to experiments on alloyed correlated systems is pointed out.

A good part of the work carried out in the thesis has been published in Refs. [44, 49, 50].

Chapter 2

From mixed valence to the Kondo lattice regime

2.1 Introduction

Rare earth lanthanides and actinides [1, 2] exhibit a wide range of behaviour such as heavy fermions (HFs), mixed valence (MV), proximity of superconductivity and magnetism, quantum critical points etc. Such behaviour arises through an interplay of a variety of factors such as hybridization between conduction bands and deep f- levels, orbital degeneracy, crystal field effects, long range spin interactions and most importantly local Coulomb repulsion [3, 9, 10, 13, 51].

In this chapter, we present a detailed and systematic theoretical investigation of a regime that borders on heavy fermions at one end and on the mixed valence regime at the other. Experimentally, such a crossover from HFs to MV or vice-versa has been observed to happen through pressure or doping [52–55]. The effects of such a crossover have been investigated for several materials [56–65]. For example, the first known heavy fermion superconductor $CeCu_2Si_2$ [53], when doped with Yttrium

(a non-magnetic homologue of Ce) shows increasing mixed valent character. The resistivity exhibits a two peak structure in the temperature range 2 K to 300 K. Varying doping concentration results in gradual coalescing of the two peak structure into a single broad peak. For the heavy fermion compound $YbCu_4Ag$ [54], the ambient pressure resistivity as a function of temperature shows a broad peak which is characteristic of mixed valent compounds. By applying pressure, the broad peak sharpens and the peak position also shifts to lower values of T, thus indicating a crossover to the Kondo lattice regime. The T^2 coefficient of the low temperature Fermi-liquid resistivity also increases sharply with pressure, implying a decrease in the coherence scale. $CeBe_{13}$ [55] also shows a pressure-induced crossover from Kondo lattice regime to mixed-valent regime, as seen in the changes in the coherence peak in the resistivity. The trend in this material is opposite to that seen in the previous example of $YbCu_4Ag$. [54]

Most previous theoretical attempts to describe the effects of pressure on heavy fermion materials have employed the single-impurity Anderson model [66–68]. An illustrative and important work in this context is that of Chandran *et al.* [66]. They use a phenomenological model comprising a competition between elastic energy cost and valence fluctuations induced magnetic energy gain. The magnetic energy for an Anderson lattice model was computed by using the free energy of an impurity Anderson model and ignoring lattice coherence effects. The free energy itself was arrived at through a slave-boson mean field approximation [69] which is a static approximation and is thus unable to treat dynamical effects of valence fluctuations. Phenomenological expressions were used to model volume dependence of the parameters, and the pressure was obtained by using $P(T,V) = -\partial F/\partial V$. The authors were able to describe continuous and discontinuous valence transitions in a single framework. However, since the impurity Anderson model was used, lattice

coherence effects were ignored. Transport quantities were not calculated. Recent years have seen the use of lattice models to describe the concentrated Kondo systems. The minimalist model that accounts for a large part of heavy fermion and mixed-valent behaviour is the periodic Anderson model (PAM).

The Kondo lattice regime within the PAM has been investigated heavily by [22, 34, 38, 40–42] within dynamical mean field theory (DMFT) and cluster extensions ignoring the d−f repulsion effects. Vidhyadhiraja *et al.* have used local moment approach(LMA) within the DMFT framework previously to understand the PAM in the Kondo lattice (KL)limit [40]. Although the mixed-valent regime was not the focus, their studies did indicate the absence of universality and scaling in the MV regime. The DC and optical transport properties were compared to several Kondo insulators and heavy fermion metals and excellent quantitative agreement was found [41, 70]. A few mixed-valent materials such as $YbAl_3$ and the skutterudite compound $CeOs_4Sb_{12}$ were also considered [71] and again good agreement between theory and experiment was found. In a recent work, valence transition in Ytterbium and Europium intermetallics was studied by Zlatic and Freericks [72] employing a multi-component Falicov-Kimball (FK) model within DMFT. The authors argue that a complete description would entail a solution of the periodic Anderson model combined with the FK model. However, since this is challenging, they chose to solve just the FK model, albeit a multi-component one. Transport quantities like DC and optical conductivity, thermopower and magnetoresistance etc were calculated and qualitatively compared to the experiment. Using an equation of motion decoupling approximation, Bennard and Coqblin [73] have investigated the PAM and explored the variation of the f- valence with various parameters of the model. They use the results of this study to understand pressure dependent valence changes. Miyake and co-workers [74] have used a variety

of methods including the slave-boson approximation, the density matrix renormalization group etc to investigate the one dimensional extended PAM (EPAM), which includes the $d-f$ repulsion effects represented by U_{cf}. The EPAM has been investigated within DMFT by Sugibayashi and Hirashima [75]using quantum Monte-Carlo methods. Their focus has been to understand the interplay between U_{cf}, valence fluctuations and superconductivity. In a recent work Ylvisaker [76] *et al.* combined local density approximation with DMFT to understand the valence fluctuation and the valence transition in the Yb metal. For the impurity solver, they have used Hirsh-Fye quantum Monte-Carlo and continuous time quantum Monte-Carlo. They reproduce the experimentally observed valence transition, and conclude that the Yb metal is a fluctuating valence material rather than an intermediate-valent one. As mentioned before and as illustrated through the above mentioned studies, there has been substantial work on the valence transition and its effect on the spectral quantities within the PAM, however the effects on transport quantities due to valence fluctuations and the crossover regime between the Kondo lattice and the mixed-valent regime have received scant attention.

In this chapter, we focus on such a KL-MV crossover using the LMA+DMFT approach to the PAM. We assume that effects of pressure/doping would be to change the model parameters, and hence a scan of the parameter space within the PAM framework should be able to provide insight into the crossover regime. We highlight the changes occurring in the dynamics and transport properties as a result of this crossover. We find several new results such as a two peak resistivity and anomalous absorption features in the optical conductivity in certain parameter regimes. We provide theoretical explanations for these anomalies, and show that such behaviour does indeed exist in real materials and may be explained quantitatively using the present approach. The paper is structured as follows: We present

the model and formalism in the next section. The results and discussions are in sections 2.3 and 2.5 respectively. A comprehensive range of experimental measurements is shown to be described by our theoretical results in section 2.6. We conclude in section 2.7.

2.2 Model and formalism

The periodic Anderson model is one of the simplest models representing a paradigm for understanding the physics of heavy-fermion compounds. In standard notation, the Hamiltonian for PAM is given by

$$\hat{H} = \epsilon_c \sum_{i\sigma} c^\dagger_{i\sigma} c_{i\sigma} - t \sum_{(i,j),\sigma} (c^\dagger_{i\sigma} c_{j\sigma} + \text{h.c.}) + V \sum_{i\sigma} (f^\dagger_{i\sigma} c_{i\sigma} + \text{h.c.}) + \sum_{i\sigma} \left(\epsilon_f + \frac{U}{2} f^\dagger_{i,-\sigma} f_{i,-\sigma} \right) f^\dagger_{i,\sigma} f_{i,\sigma} \,. \tag{2.1}$$

For a detailed description of the various terms in the PAM, we refer the reader to chapter 1.

In the non-interacting case, the two orbital energies ϵ_c and ϵ_f completely determine the nature of the ground state, i.e. whether the system would be gapped or gapless at the Fermi level. Equivalently, the occupation numbers $n_f = \sum_\sigma \langle f^\dagger_{i\sigma} f_{i\sigma} \rangle$ and $n_c = \sum_\sigma \langle c^\dagger_{i\sigma} c_{i\sigma} \rangle$ may also be used to characterize the ground state. It is straightforward to see that the system is a band insulator for $n_f + n_c = 2$, while it is metallic for $n_f + n_c \neq 2$ [9].

The f- and c- Green's functions within DMFT are given by

$$G^f(\omega) = \left[\omega^+ - \epsilon_f - \Sigma(\omega) - \frac{V^2}{\omega^+ - \epsilon_c - S(\omega)}\right]^{-1} \tag{2.2}$$

$$G^c(\omega) = \left[\omega^+ - \epsilon_c - S(\omega) - \frac{V^2}{\omega^+ - \epsilon_f - \Sigma(\omega)}\right]^{-1} \tag{2.3}$$

where $\Sigma(\omega)$ is the momentum-independent f- self-energy which represents interaction effects and $S(\omega)$ is the Feenberg self-energy [43], which represents the self-consistent hybridization. Within DMFT, vertex corrections are absent, hence the single-particle Green's functions are sufficient within Kubo formalism to obtain transport quantities such as DC resistivity and optical conductivity. The expressions have been derived previously [40], and we reproduce them here for completeness:

$$\sigma(\omega) = \frac{\sigma_0}{2\pi^2}\mathrm{Re}\int_{-\infty}^{\infty} d\omega' \frac{n_F(\omega') - n_F(\omega+\omega')}{\omega} \left[\frac{G^{c*}(\omega') - G^c(\omega+\omega')}{\gamma(\omega+\omega') - \gamma^*(\omega')} - \frac{G^c(\omega') - G^c(\omega+\omega')}{\gamma(\omega+\omega') - \gamma(\omega')}\right] \tag{2.4}$$

where $\sigma_0 = 4\pi e^2 t^2 a^2 n/\hbar$ for lattice constant a, electronic charge e, and electron density n and $\gamma(\omega) = \omega^+ - \epsilon_c - V^2[\omega^+ - \epsilon_f - \Sigma(\omega)]^{-1}$. The DC conductivity is obtained by considering the $\omega \to 0$ limit of the above equation as

$$\sigma_{DC} = \frac{\sigma_0}{2\pi^2}\mathrm{Re}\int_{-\infty}^{\infty} d\omega \left(-\frac{dn_F}{d\omega}\right)\left[\frac{\pi D^c(\omega)}{\mathrm{Im}\gamma(\omega)} + 2\left(1 - \gamma(\omega)G^c(\omega)\right)\right] \tag{2.5}$$

where $D^c(\omega) = -\mathrm{Im}G^c(\omega)/\pi$ is the spectral function of the retarded Green's function $G^c(\omega)$ and $n_F(\omega) = (e^{\beta\omega}+1)^{-1}$ is the Fermi function.

2.3 Results

In this section, we show results for spectral functions, i.e. the density of states (DOS), at both zero and finite temperature, optical conductivity again for $T \geq 0$, and DC resistivity. We work with a reasonably large interaction strength ($U \simeq 4.5t_*$) and a hybridization strength of $V^2 = 0.6t_*^2$. The crossover from Kondo lattice regime to the mixed-valent regime is investigated by varying ϵ_c and ϵ_f such that the total occupancy $n_{tot} = n_c + n_f$ is fixed, and n_f is decreased. This is done because pressure experiments would be expected to keep the total occupancy fixed. The practical details of implementation are given in references [38, 40]. We begin with the low energy scale and the spectra.

2.3.1 Coherence scale

The low energy coherence scale has been identified in previous studies to be $\omega_L = ZV^2/t_*$, where $Z = (1 - \partial\Sigma/\partial\omega|_{\omega=0})^{-1}$ is the quasiparticle weight (inverse effective mass). This scale is exponentially small in the strong coupling Kondo lattice regime ($n_f \to 1$). Spectral functions, optical conductivities and resistivity were shown to be universal functions of $(T/\omega_L, \omega/\omega_L)$ in our previous studies [38, 40, 70]. A crossover to the mixed-valence regime ($n_f \ll 1$) manifests in a rapid increase in ω_L as shown in figure 2.1, which shows the variation of the lattice coherence scale ω_L with the f- orbital occupancy n_f for a fixed $n_{tot} = 1.25$ (filled circles) and $n_{tot} = 1.1$ (squares). A lowering of the f- orbital occupation implies greater local charge fluctuations, implying an effective decrease of correlation effects. This in turn implies a decrease in effective mass or an increase in Z and hence an increase in ω_L with decreasing n_f.

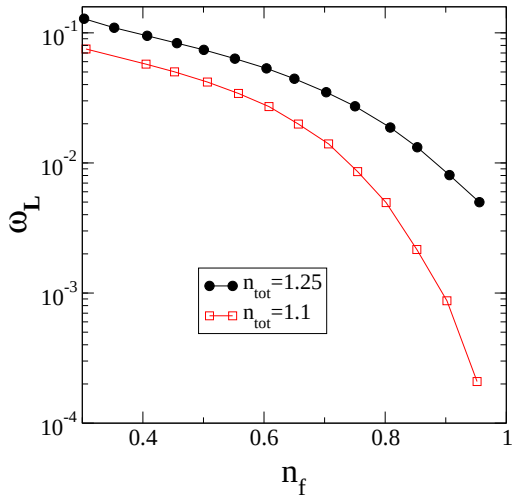

Fig. 2.1: A sharp decrease of the lattice coherence scale, ω_L is seen, with n_f increasing from the mixed-valence regime ($n_f \ll 1$) to the Kondo lattice regime ($n_f \to 1$).

2.3.2 Density of states: Zero temperature

The density of states or the spectral functions are considered next. The changes in the low frequency Kondo resonance and in the high frequency Hubbard bands are identified as the f- valence is varied.

We show the $T = 0$ f spectral function ($D^f(\omega; T = 0) = -\mathrm{Im}G^f(\omega, T = 0)/\pi$) in the left panel of figure 2.2. A usual three peak structure with high energy Hubbard bands and a narrow Kondo resonance at the Fermi level is seen for all n_f. The lower Hubbard band moves closer to the Fermi level, while the upper Hubbard band shifts to higher energies with decreasing n_f. The insets in figure 2.2 show the Kondo resonance in greater detail as a function of the scaled frequency ω/ω_L. In the Kondo lattice regime, a pseudogap is seen straddling the resonance, which gets progressively filled up and for the lower values of n_f, there is no trace of a pseudogap. Such a transfer of spectral weight is very non-trivial and is a very significant feature as it manifests clearly in a second peak in optical conductivity. The conduction band density of states, $D^c(\omega; T = 0)$, shown in the right panel

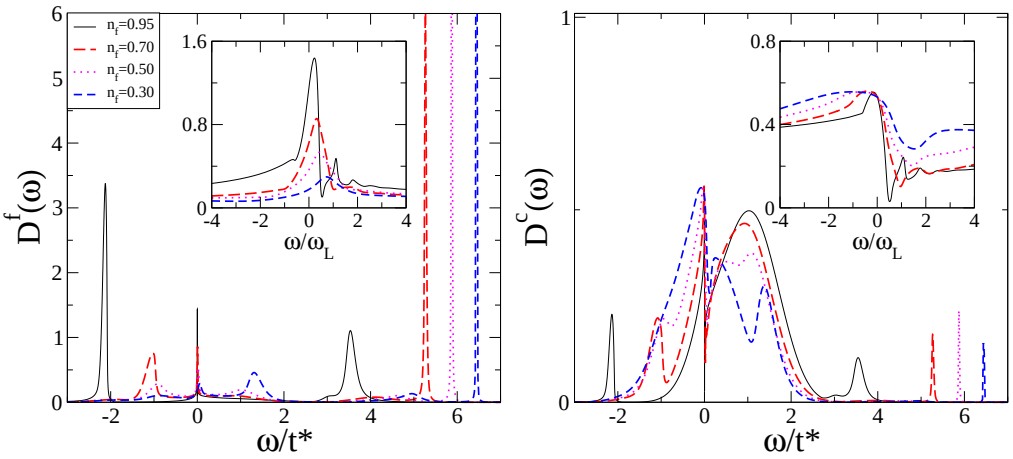

Fig. 2.2: The zero temperature spectral functions, $D^{\nu}(\omega; T = 0)$, $\nu = c, f$ are shown as a function of 'absolute' frequency ω/t_* for various f- occupancies (n_f) and a fixed $n_{tot} = 1.25$. The insets show the same spectra as the main panel, but as a function of the scaled frequency ω/ω_L highlighting the changes in the Kondo resonance and the pseudogap.

of figure 2.2, has an overall Gaussian envelope, with spectral weight carved out at the effective f- level, ϵ_f^* (see section 2.5 for further discussion) in the form of a pseudogap and small Hubbard bands flanking the envelope. In contrast to the f- DOS (left panel of figure 2.2), the Hubbard bands here possess a very small fraction of the total spectral weight. The lower Hubbard band is distinct from the envelope at higher $n_f(\gtrsim 0.75)$, and merges into the envelope at lower $n_f(\lesssim 0.6)$. The pseudogap fills up with decreasing n_f and for the lowest n_f values shown, there is indeed no trace of a pseudogap (see right panel)

2.3.3 Density of states: Temperature dependence

In figure 2.3, we show the evolution of the f- DOS as a function of temperature for $n_f = 0.8$ and $n_f = 0.3$ in the left and right panels respectively. The insets in the panels show the low frequency, low temperature ($(\omega/\omega_L, T/\omega_L) \sim \mathcal{O}(1)$) part more clearly. With increasing temperature, there is a spectral weight transfer on all

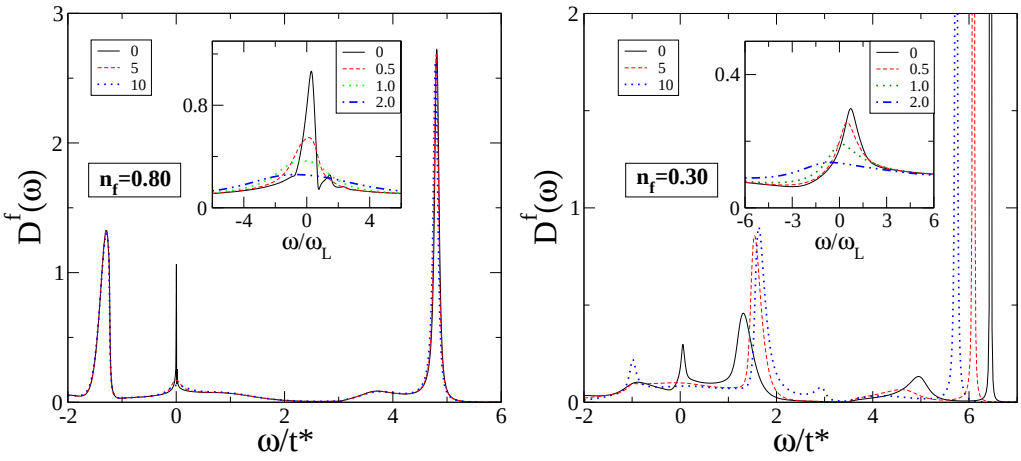

Fig. 2.3: The f- electron spectral function at temperatures $\tilde{T} = T/\omega_L = 0, 2, 5, 10, 20$ (indicated as legends) and for all scales in the main panel. The insets show the low frequency part as a function of scaled frequency for lower temperatures. The left panel is for $n_f = 0.75$ and the right panel is for $n_f = 0.40$.

scales. The pseudogap proximal to the Fermi level fills up, while a thermal broadening of the Kondo resonance is clearly visible in the f- DOS. The Hubbard bands are high energy ($\sim U/2$) features in the Kondo lattice regime, and hence don't get affected on temperature scales of the order of the exponentially small coherence scale ω_L. The physics in the mixed-valent regime is, naturally, different. The coherence scale is not exponentially small (see figure 2.1). At any given temperature T, it is expected that changes in the spectral function will occur upto $\omega \sim T$. And indeed, this is seen in the KL regime. However, in the MV regime, spectral weight transfer occurs in an energy interval that is far greater than the thermal energy scale. A new spectral feature, that appears to be a symmetric partner of the LHB, is seen to emerge in the MV regime. What is more suprising is that instead of experiencing thermal broadening, this feature actually gains spectral weight and grows with increasing T. Angle-resolved photoemission experiments should be able to easily identify such a feature. The conduction band density of states exhibits similar temperature dependence as the f- DOS and is hence not shown.

2.4 Transport properties

2.4.1 $T = 0$ optical conductivity

The zero temperature Green's functions are sufficient within DMFT to compute the $T = 0$ optical conductivity, $\sigma(\omega; T = 0)$ (Eq. (2.4)). In figure 2.4, we show $\sigma(\omega; T = 0)$ as a function of frequency (ω/t_*) for various values of n_f and a fixed $n_{tot} = 1.1$. For $n_f \to 1$, a familiar structure of a single mid-infrared peak (MIR) is obtained. As we decrease n_f, the MIR peak shifts to higher frequencies. The

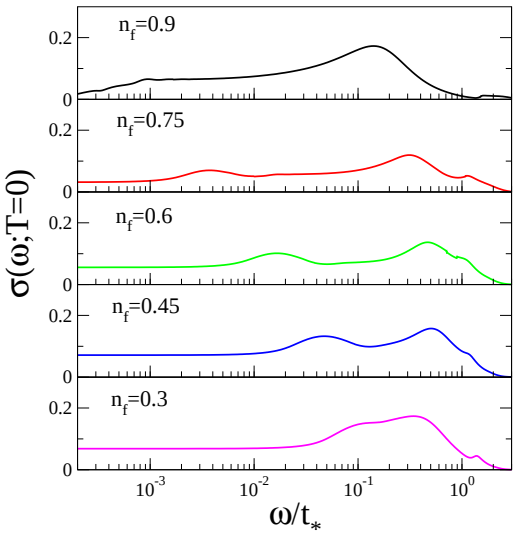

Fig. 2.4: The zero temperature optical conductivity $\sigma(\omega; T = 0)$ as a function of frequency (ω/t_*) for various n_f, and fixed $n_{tot} = 1.1$.

lower n_f values hold a surprise. A deep mid-infrared (DMIR) absorption feature or a shoulder emerges for lower n_f values. This is distinct from the above mentioned MIR peak. Such a two peak structure has been reported [56], but has not been understood quantitatively. Recently it has been pointed out through band structure studies that this feature could be due to transitions to the effective f- level [77]. Here we confirm (see the discussion section) that this feature is indeed absorption into the effective f- level at $\epsilon_f^* = Z(\epsilon_f + \Sigma(0))$. Here we must add that a clear

two-peak structure is not obtained for higher n_{tot}, such as that considered for the spectra ($n_{tot} = 1.25$) in figure 2.2 (also see [40] for optics in the KL regime).

2.4.2 DC Resistivity as a function of temperature

We now move on to finite temperature transport. In figure 2.5, we show the DC resistivity as a function of temperature T/t_*. The left panel shows the resistivity for $0.65 \leq n_f \leq 0.95$, while the right panel is for $0.30 \leq n_f \leq 0.60$. All of the theoretically computed $\rho(T)$ have zero residual values, but for visual clarity, they have been appropriately vertically offset. There is a clear shift of the coherence peak (low temperature peak) to higher temperatures since its position correlates with the low energy scale [40], and ω_L itself increases sharply with decreasing n_f. The right

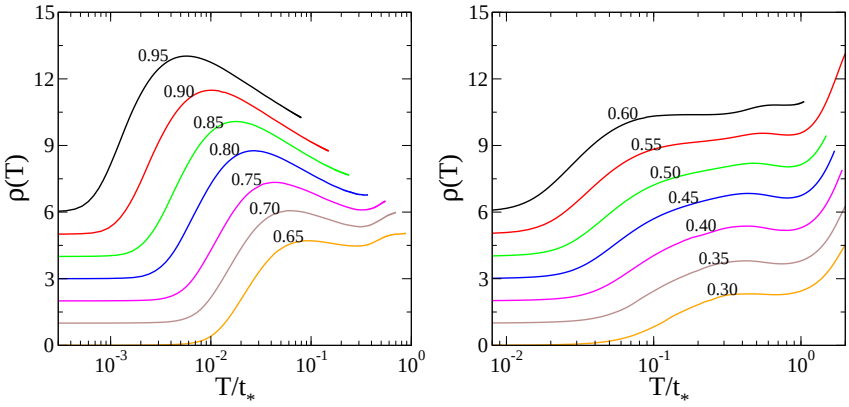

Fig. 2.5: DC resistivity for various n_f values (mentioned next to the curve) as a function of temperature T/t_* for a fixed $n_{tot} = 1.25$. All of the theoretically computed $\rho(T)$ have zero residual values, but for visual clarity, they have been appropriately vertically offset.

panel of figure 2.5 shows the DC resistivity for $0.30 \leq n_f \leq 0.60$. The functional form in this range of n_f is seen to be qualitatively different than the range shown in the left panel. The coherence peak is not a distinct feature anymore. For $n_f = 0.65$ and 0.60, a distinct two peak resistivity is seen. The two peaks coalesce and form a broad peak for lower n_f values. A broad resistivity peak is well known to be

a characteristic feature of mixed-valent systems. Here we show that the crossover from the Kondo lattice regime to the mixed- valent regime involves the coalescing of the coherence peak and a high temperature peak into a single broad peak. This high temperature peak is present but not visible in the KL regime. Pressure/doping-dependent resistivity measurements in $CeCu_2Si_2$ [52,53,64]show similar behaviour. For low pressure, a two peak resistivity is observed. As a function of increasing pressure, the two peaks merge and a single broad peak is obtained. We emphasise here that the model Hamiltonian we use has a single c- band and a single f- level, and hence neglects the crystal field effects completely, which are believed to be the reason for multiple peaks in various materials. Nevertheless a two-peak structure is seen in certain regimes here. We will discuss the origin of the second peak in section 2.5 and the relevance of our results to experiments in section 2.6.

2.4.3 $T > 0$ Optical transport

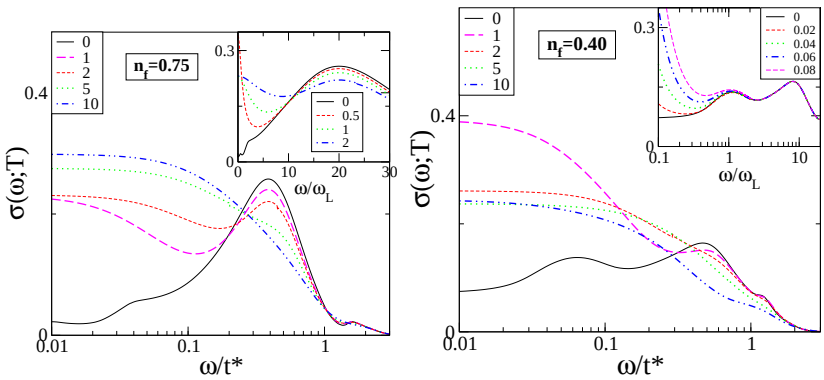

Fig. 2.6: Optical conductivity $\sigma(\omega;T)$ for $n_f = 0.75, n_c = 0.61$ and $n_f = 0.40, n_c = 0.71$ in the left and right panels respectively ($\epsilon_c = 0.5t_*$ and $U \sim 4.7t_*$) as a function of ω/t_* in the main panels and as a function of ω/ω_L in the insets respectively for various temperature values (given as multiples of ω_L in the legends). The insets show $\sigma(\omega;T)$ for low temperatures to show the transfer of spectral weight more clearly.

We now show the temperature dependence of the optical conductivity in figure 2.6 for two different f- occupancies, 0.75 and 0.4 (other parameters are men-

tioned in the figure caption) in the left and right panels respectively. The $\sigma(\omega;T)$ for the higher n_f case has a usual prominent mid-infrared (MIR) peak, with a slight shoulder at lower frequencies. The inset shows the low temperature evolution of $\sigma(\omega)$, while the main panel shows $T \leq 10\omega_L$. With increasing temperature, a transfer of spectral weight over all energy scales in seen. The lower $n_f(= 0.4)$ optical conductivity shown in the right panel of figure 2.6 is qualitatively different from that of the left panel. The shoulder like structure seen in the Kondo lattice regime (left panel) develops into a full peak in the mixed-valent regime, while the MIR peak diminishes in intensity and gets broader. The analysis at $T = 0$ shows (see section 2.5) that the lower frequency peak occurs at the effective f- level ϵ_f^*. The inset shows that the DMIR peak or the shoulder appears only below a temperature $T = 0.08\omega_L$ even though it is positioned at a frequency ω equal to the coherence scale ω_L (since here $\epsilon_f + \Sigma(0) \sim 1$). This precise behaviour is seen in recent optical conductivity measurements in $YbIr_2Si_2$ [78](see section 2.6).

2.5 Discussion

2.5.1 Spectral features: Kondo resonance and Hubbard bands

At high energies, the prominent spectral features are the Hubbard bands. In figure 2.2, it is seen that the Hubbard bands shift to the right with decreasing n_f. This is expected from the atomic limit, since the Hubbard bands occur at ϵ_f and $\epsilon_f + U$ in the atomic limit, and ϵ_f moves closer to the Fermi level when n_f decreases. However, we note that the Hubbard bands are not at the positions predicted by the atomic limit. This discrepancy is due to a combination of shifts in the levels

arising through hybridization and self-energy effects.

In the other extreme, i.e. close to the Fermi level, a low frequency form of the Green's functions using a Fermi liquid self-energy $\Sigma(\omega) = \Sigma(0) + \omega(\frac{1}{Z} - 1) + \mathcal{O}(\omega^2)$ may be derived that enables us to understand most of the features of the Kondo resonance. The resulting spectral functions in the neighbourhood of the Fermi level are given by

$$\begin{aligned} D^c(\omega) &\sim \rho_0 \left(\omega - \epsilon_c - \frac{ZV^2}{\omega - Z\bar{\epsilon}_f} \right) \\ V^2 D^f(\omega) &\sim \left(\frac{ZV^2}{\omega - Z\bar{\epsilon}_f} \right)^2 D^c(\omega) \end{aligned} \tag{2.6}$$

where $\epsilon_f^* = Z\bar{\epsilon}_f = Z(\epsilon_f + \Sigma(0))$ is the effective f- level. These equations show that the low energy ($\omega \lesssim \omega_L$) spectral features are precisely those of a non-interacting ($U = 0$) PAM with renormalized parameters ($V^2 \to ZV^2, \epsilon_f \to Z(\epsilon_f + \Sigma(0))$ and ($\epsilon_c \to \epsilon_c$) [38]. Thus, this is the renormalized non-interacting limit (RNIL). A scaling collapse of the numerically obtained spectra with the analytical expressions above would be a demonstration of adiabatic continuity of the interacting system to the non-interacting limit.

As $\omega \to \epsilon_f^*$ in Eq. (2.6), the spectral functions also vanish $D^\nu(\omega) \to 0$, thus the pseudogap seen in the spectra is positioned at the effective f- level, $\epsilon_f^* = Z\left(\epsilon_f + \Sigma(0)\right)$. Transfer of spectral weight into the pseudogap happens with decreasing n_f as seen in figure 2.2 which implies that the frequency interval in the neighbourhood of ϵ_f^* is gaining spectral weight. This spectral weight transfer is completely missed by theories that are equivalent to the renormalized non-interacting limit. This includes approaches such as slave-boson theories or two-band models of heavy fermion systems, which ignore the imaginary part of self-energy. The variation of ϵ_f^* with n_f may be easily predicted using the Luttinger's theorem which

states [38]

$$\frac{1}{2}(n_f + n_c) = \int_{-\infty}^{-\epsilon_c + V^2/\bar{\epsilon}_f} \rho_0(\epsilon)\, d\epsilon + \theta(-\bar{\epsilon}_f)\,. \tag{2.7}$$

For fixed $n_{tot} = n_f + n_c$, the upper limit of integration on the right side of Eq. (2.7) is also fixed. Crossing over from the KL to MV regime would require decreasing n_f and increasing n_c, which in turn would require decreasing ϵ_c. Thus to keep $-\epsilon_c + V^2/\bar{\epsilon}_f$ fixed, the $\bar{\epsilon}_f = \epsilon_f + \Sigma(0)$ must increase, and hence the effective f-level, $\epsilon_f^* = Z\bar{\epsilon}_f$, also increases as n_f decreases. This is indeed seen in the figure 2.2 because the position of the pseudogap does indeed shift to higher frequencies as n_f is decreased.

2.5.2 Inadequacy of the renormalized non-interacting limit

In [40], it was shown that the two band model or the RNIL predicts a square root singularity at the minimum direct gap ($\sim 2\sqrt{Z}V$), and hence the MIR peak is generally attributed to the direct gap. A simple Fermi-liquid analysis $\Sigma(\omega) \simeq \mathrm{Re}\Sigma(0) + \omega(1 - 1/Z)$ of the poles of the $\mathbf{k}-$ dependent conduction electron Green's function

$$G^c(\omega; \epsilon_{\mathbf{k}}) = \left[\omega^+ - \epsilon_c - \epsilon_{\mathbf{k}} - \frac{V^2}{\omega^+ - \epsilon_f - \Sigma(\omega)}\right]^{-1} \tag{2.8}$$

yields a two-band model

$$\omega_{\pm}(\epsilon_{\mathbf{k}}) = \frac{\left(\epsilon_c + \epsilon_{\mathbf{k}} - \epsilon_f^*\right) \pm \sqrt{\left(\epsilon_c + \epsilon_{\mathbf{k}} - \epsilon_f^*\right)^2 + 4ZV^2}}{2} \tag{2.9}$$

The minimum direct gap is given by $\min(\omega_+(\epsilon_{\mathbf{k}}) - \omega_-(\epsilon_{\mathbf{k}}))$. The square root singularity at the direct gap appears in the two band model because the imaginary part of the self-energy is neglected, and the resulting spectral functions are Dirac delta functions. Including incoherent effects due to electron-electron scattering results

in broadening of the MIR peak and cutting off the square root singularity. The strong coupling Kondo lattice regime has a large universal region on the frequency axis, however the mixed-valent regime shows clear deviations from universality, and consequently, the range of frequencies over which incoherent behaviour would manifest would be larger (universal region is smaller) than the Kondo lattice regime. This would result in a broader MIR peak in the mixed-valence regime (lower n_f, right panel, figure 2.4). At the lower n_f values, a clear two-peak structure is visible in the optical conductivity. The low frequency peak is in fact at the effective f- level, as argued below, while the high frequency peak is the usual MIR peak. Naively, finding an absorption peak at ϵ_f^* is counter-intuitive, because the renormalized non-interacting limit (Eq. (2.6)) shows that a pseudogap exists at ϵ_f^*, implying that there is no density of states at that energy. So how can absorption into a gap happen? The answer is of course that the RNIL, which is equivalent to a slave-boson mean-field theory, which in turn is equivalent to a two-band model, are not totally correct in their predictions. These approaches neglect the imaginary part of the self-energy (scattering rate). So even though the RNIL predicts a gap, there is in fact no gap at ϵ_f^* when self-energy effects are included. And in fact, it may be shown rigorously, without recourse to LMA that absorption to ϵ_f^* will happen provided the imaginary part of self-energy is non-zero at that energy. To see this, consider the roots of the real part of the denominator of the conduction electron Green function, $G^c(\omega, \epsilon_{\mathbf{k}})$ (Eq. (2.8)), given by

$$\begin{aligned} \mathrm{Re}\left[\omega - \epsilon_c - \epsilon_{\mathbf{k}} - V^2\left(\omega - \epsilon_f - \Sigma(\omega)\right)^{-1}\right] = \\ \omega - \epsilon_c - V^2 \frac{\omega - \epsilon_f - \mathrm{Re}\Sigma(\omega)}{\left(\omega - \epsilon_f - \mathrm{Re}\Sigma(\omega)\right)^2 + \left(\mathrm{Im}\Sigma(\omega)\right)^2} = \epsilon_{\mathbf{k}} \end{aligned} \tag{2.10}$$

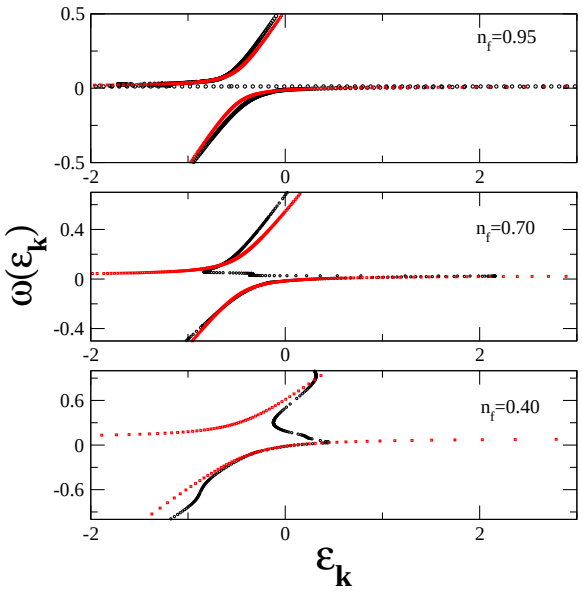

Fig. 2.7: The dispersion $\omega(\epsilon_{\mathbf{k}})$ computed from Eq. (2.10) (black) and from the RNIL, Eq. (2.9) (red) for $\epsilon_c = 0.5t_*, U \sim 4.7t_*$ and $n_f = 0.95, n_c = 0.58$ (top panel), $n_f = 0.70, n_c = 0.63$ (middle panel) and $n_f = 0.40, n_c = 0.71$ (bottom panel).

If the imaginary part of the self-energy is completely neglected and a first order Taylor expansion is carried out for the real part of the self-energy, we get back Eq. (2.9). However, retaining the imaginary part, however small it might be, results in an equation that is at least cubic in order. And for $\epsilon_{\mathbf{k}} = \epsilon_c - Z(\epsilon_f + \Sigma(0))$, one of the roots is just $\epsilon_f^* = Z(\epsilon_f + \Sigma(0))$.

We support the arguments above with LMA results below. The dispersion, $\omega(\epsilon_{\mathbf{k}})$ is computed for $n_f = 0.95(n_c = 0.58), 0.7(n_c = 0.63)$ and $n_f = 0.4(n_c = 0.71)$ with $\epsilon_c = 0.5, U \sim 4.7t_*$ through Eq. (2.10) and shown in the top, middle and bottom panels respectively in figure 2.7. The two-bands obtained at the renormalized non-interacting level (Eq. (2.9)) are also superimposed in red. It is clear from the figure that the agreement of the two-band model with the full dispersion gets progressively worse as n_f decreases. For $n_f = 0.4$, the middle band is clearly visible in the full dispersion, while being completely absent in the two-band picture. This third band, as argued above is centred at $\omega = \epsilon_f^*$. It is the excitations from

the 'band' below the Fermi level to ϵ_f^*, that appears as an additional 'anomalous' absorption peak in the deep mid-infrared region (as a shoulder). This anomalous peak is seen to become prominent in the mixed-valent regime and is very small or invisible in the Kondo lattice regime. As we will see later, such a two-peak optical conductivity has indeed been observed in recent experiments (section 2.6).

2.5.3 Origin of the two-peak resistivity

We have shown previously that the coherence peak (low temperature peak) in the resistivity, which would be a minimum in the conductivity [40], occurs at a temperature comparable to ω_L, the low temperature scale. The second peak (high temperature peak) has been attributed to crystal field split levels. However, we find a far simpler explanation even within the single band PAM. The second peak occurs at a temperature that is roughly half of the lower Hubbard band energy scale. It might at first seem surprising to note that the Hubbard band is contributing to transport. The Hubbard bands are usually at an energy scale of $U/2$ which being of the order of a few eV, remain untouched until room temperature. Nevertheless, for mixed-valent systems, even if the U is large, either the LHB or the UHB moves close enough to the Fermi level so as to be affected at room temperature scales. To show the contribution of the Hubbard band states to the conductivity, we consider expression, Eq. (2.5) again. On the right hand side, the integration is carried out over all frequencies. However, if we introduce a upper and a lower cutoff in the integration limits, we can isolate the contribution of individual spectral features within those limits. In figure 2.8, we show the calculated DC resistivity for $n_f = 0.6, n_c = 0.66$, with three different cutoffs: (i)the solid line being no cutoff (full resistivity), (ii) the dashed line having limits such that the lower Hubbard band is excluded but the symmetric partner of the LHB is included and (iii) the dotted

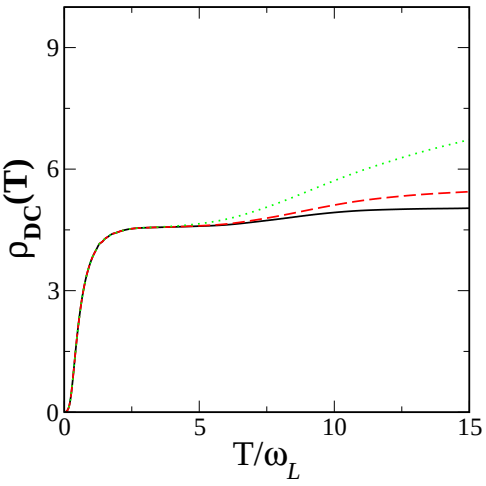

Fig. 2.8: Figure shows that the second peak in the DC resistivity seen most clearly in the right panel of figure 2.5 for $n_f = 0.6$ disappears progressively by excluding the lower Hubbard band and other spectral features. The solid line is for $n_f = 0.6, n_c = 0.66$ and is the full resistivity. The dashed and the dotted lines are obtained by excluding the lower Hubbard band below the Fermi level and with decreasing cutoff above the Fermi level (see text for discussion).

line having limits such that both the LHB and its symmetric partner are excluded. It is seen that excluding the spectral weight of the Hubbard bands enhances the resistivity systematically. This shows that the Hubbard band contribution to the DC conductivity is substantial in mixed-valent compounds. The two-peak behaviour of resistivity, however is specific to the parameter regime used in this manuscript ($U/V^2 \sim 8, n_{tot} = 1.25$). In other parameter regimes, such as U/V^2 much larger or much smaller than that considered here or $n_{tot} = 1.1$, our calculations demonstrate (not shown here) that the DC resistivity crosses over from a single sharp coherence peak to a broad peak lineshape with decreasing valence, without going via a two-peak structure. This would be relevant for understanding the effects of valence fluctuations in materials such as $YbCu_4Ag$ [54] and $CeBe_{13}$ [55].

2.6 Comparison to Experiments

2.6.1 DC resistivity: Ambient pressure

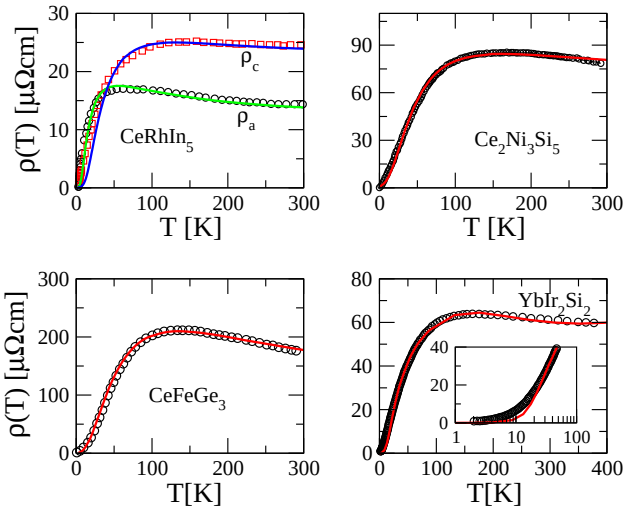

Fig. 2.9: Comparison of resistivity measurements for four different materials with theory. Please refer to text for discussion.

In figure 2.9, we have superposed theoretically computed DC resistivity (solid lines) with the experiments (circles) for $CeRhIn_5$ [79], $Ce_2Ni_3Si_5$ [80], $CeFeGe_3$ [81] and $YbIr_2Si_2$ [78]. To find the appropriate theoretical parameters for each material, we had to adopt a trial and error approach. However, a surprising similarity in the DC resistivity of $CeRhIn_5$ and $Ce_2Ni_3Si_5$ reduced our effort substantially. We found that we could take the experimentally measured DC resistivity for the two materials and scale them onto each other simply by rescaling the x and y axes. $CeRhIn_5$ has anisotropic resistivity, nevertheless the ρ_a and ρ_c may also be scaled onto each other, thus showing that qualitatively, they are also similar. We find that these two materials have an f- occupancy $n_f \sim 0.7$, with the rest of the parameters being $n_c \sim 0.55, U/V^2 \sim 8, \epsilon_c = 0.5t_*$. For $CeFeGe_3$, we found that the mixed-valence resistivities do not fit the data well. Rather, the best fit was found using parameters

($n_f \sim 1, n_c \sim 0.77, U/V^2 \sim 5, \epsilon_c = 0.3$) that signify an intermediate correlation with f- occupancy being nearly unity. The optical transport data for $YbIr_2Si_2$ (see below) shows a two-peak structure very similar to that seen in figure 2.4 for $n_f = 0.4$ and $n_{tot} = 1.1$. Thus we take the same resistivity and superimpose that onto the experimentally measured one, and we see very good agreement.

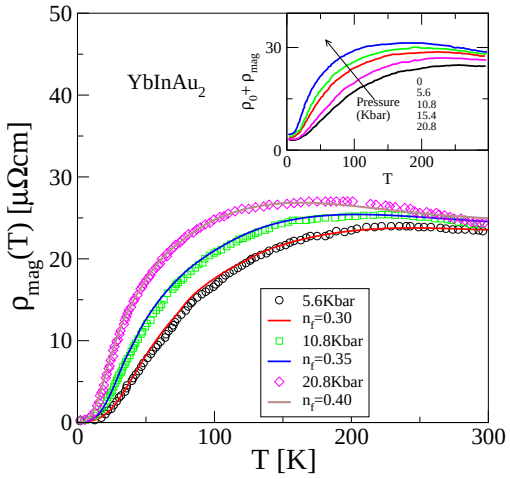

Fig. 2.10: Comparison of pressure dependent resistivity measurements (magnetic contribution only) for $YbInAu_2$ with theory. The inset shows the reported [82] experimental data.

2.6.2 DC resistivity: Pressure dependence

Hydrostatic pressure dependence measurements of the DC resistivity of $YbInAu_2$ and its non-magnetic homologue $LuInAu_2$ have been carried out by Fuse *et al.* [82]. The experimental magnetic resistivity along with the residual resistivity ($\rho_{mag} + \rho_0$) is shown in the inset of figure 2.10. The main panel shows a comparison of theory (solid lines, $n_{tot} = 1.1, U/V^2 \sim 8$) with experiment (symbols). The agreement is seen to be excellent. The T_{max} is seen to decrease with pressure, and the material appears to be progressing towards a Yb^{3+} state with increasing pressure, as conjectured in the experimental paper. Nevertheless, the valence remains in the

mixed-valent regime ($\lesssim 0.4$), even with pressures upto 20KBar.

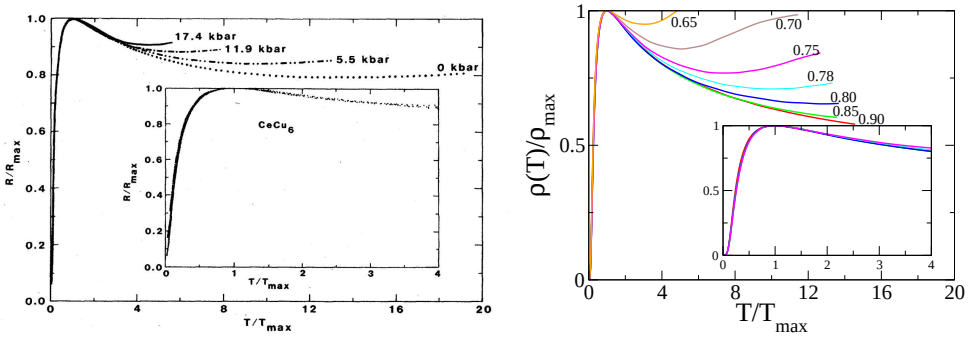

Fig. 2.11: Left panel: Experimentally measured pressure dependent resistivity measurements for $CeCu_6$ [83]. Right panel: Theoretically computed $\rho(T)$ (same data as left panel of figure 2.5) plotted as ρ/ρ_{max} *vs.* T/T_{max}. The respective valencies are mentioned next to the curves.

We now move on to $CeCu_6$, which has gathered a lot of attention in the past decade as a material that can be tuned to a quantum critical point with Au doping. Pressure dependent resistivity measurements on $CeCu_6$ were carried out in 1985 by Thomson and Fisk. They found that with increasing pressure, the material crosses over from Kondo lattice like to mixed-valence like regime. In the left panel of figure 2.11, we show the experimental graph, while in the right panel, the theory (same data as that for figure 2.5) is shown. The experiment shows that with increasing pressure, the temperature dependence follows the $P = 0$ curve to some temperature and then deviates. In the inset of the left panel, the experimental data for $0 \leq P \leq 17.4$ kbar is shown to collapse when plotted as R/R_{max} *vs.* T/T_{max} for $T \leq 4T_{max}$. The theoretical curves in the right panel correspond very closely to those seen in the experiment. The agreement between theory and experiment shows that indeed with increasing pressure, the occupancy does change from $n_f \to 1$ to $n_f \sim 0.75$, thus implying that the valence of Ce changes from $\sim 3+$ to $\sim 2.75+$. The theory curves decrease more rapidly (than experiment) with increasing temperature beyond the coherence peak, and the reason for this

is that the phonon contribution is not subtracted in the experiment. The inset in the theory panel has five different valencies plotted together, namely, $n_f = 0.90, 0.85, 0.80, 0.78$ and 0.75. Except for $n_f = 0.75$, the rest of the data is seen to collapse onto a single curve, as seen in the experiment. The $n_f = 0.75$ curve does collapse upto a certain temperature and then deviates from the universal curve.

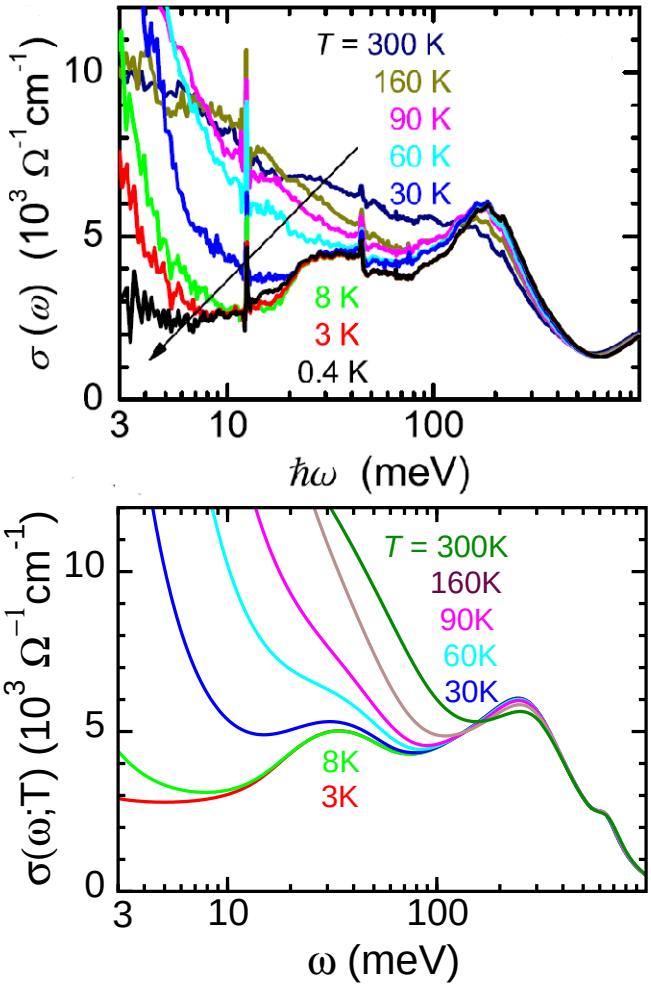

Fig. 2.12: Top panel: Experimentally measured optical conductivity for $YbIr_2Si_2$ [78]. Bottom panel: Theoretically computed $\sigma(\omega; T)$ for $U/t_* \sim 5, V^2 \sim 0.6t_*^2$ and $\epsilon_c = 0.5t_*$, which yields $n_f = 0.4$ and $n_c = 0.7$. Excellent quantitative agreement is observed between theory and experiment for the line shape and the temperature dependence.

2.6.3 Optical transport: $YbIr_2Si_2$

The recently discovered heavy fermion system $YbIr_2Si_2$ [84] has a crystal structure similar to the well studied $YbRh_2Si_2$. The latter exhibits a field-tuned quantum critical point (QCP), while the former has a pressure-tuned first order phase transition to a ferromagnetic phase. The experimentally measured optical conductivity [78] is shown in the top panel of figure 2.12. A clear two peak structure is evident, and a large scale spectral weight transfer occurs as temperature is increased from 0.4 K to 300 K. An important characteristic of the temperature dependence of $\sigma(\omega; T)$ is that, as temperature is increased, the lower frequency peak (shoulder) merges into the continuum at $T \sim 60$ K, at which temperature the higher frequency peak remains untouched.

In the experiment, the shoulder peak appears only for $T \lesssim 30$ K, which, according to theory, should be roughly 0.08 times the peak frequency (see the discussion for figure 2.6). Thus, theoretically, we can predict that the shoulder should appear at $\sim 30.0/0.08$ K $\simeq 32$ meV. The shoulder peak position as predicted by theory indeed agrees very well with the experimentally observed shoulder position (~ 30 meV). The bottom panel of the same figure shows the optical conductivity computed for $U/t_* \sim 5, V^2 \sim 0.6t_*^2$ and $\epsilon_{=}0.5t_*$, which yields $n_f = 0.4$ and $n_c = 0.7$, thus classifying $YbIr_2Si_2$ as a mixed-valent material. These parameters were chosen using the results shown in figure 2.4, and for consistency, we note that the DC resistivity in the experiment has a broad and shallow peak (see figure 2.9) which indicates that $YbIr_2Si_2$ belongs to the mixed-valent regime. The DC conductivity obtained through a low frequency limit in the theory is higher than the corresponding experimental values. This is natural, since the theory neglects electron-phonon scattering, which if included would reduce the theoretical conductivities. Apart

from this disagreement, an excellent agreement between theory and experiment is seen in quantitative terms for both the lineshape and the temperature dependence. A phenomenological analysis [78] of the experimental optical conductivity using Drude and extended Drude formalism has been used to infer non-Fermi liquid nature of the quasiparticles in this material. However, if the quantitative agreement between theory and experiment is any indication, this material is a perfect Fermi liquid. The self-energy has the correct Fermi liquid form for the parameters used to compute the optical conductivity in the bottom panel of figure 2.12. In our approach, the Luttinger's theorem is used as a constraint, which also supports the inference of Fermi liquid behaviour. The low temperature resistivity also exhibits a clean T^2 behaviour, which again supports a Fermi liquid ground state. Additionally, we conclude that this material is in the mixed-valent regime with an effective f- occupancy of $n_f = 0.4$, which would correspond to an effective valence $Yb^{2.4+}$. (Naturally, the n_f given here must be interpreted as hole occupancy for Yb compounds.) This effective valence predicted by our theory disagrees with the inference from susceptibility measurements, which yields a Yb valence close to 3+. Further theoretical and experimental investigations are needed to resolve this. We can also infer that the effective f- level given by $\epsilon_f^* = Z(\epsilon_f + \Sigma(0))$ in $YbIr_2Si_2$ is located at roughly 25-30 meV. The DC resistivity calculated from theory for the parameters mentioned in the figure 2.12 does agree qualitatively with experiment in terms of a broad peak and the lineshape(see figure 2.9), however, the scale inferred from fitting to the experimental data does not agree with that obtained from optical conductivity.

2.7 Conclusions

We have carried out an extensive study of the changes in spectral and transport properties of the periodic Anderson model as the f- occupation number is varied from unity to nearly zero. The local moment approach within dynamical mean field theory has been employed for this study. We have used the results of our study to understand the crossover from mixed-valent regime to the Kondo lattice regime (or vice-versa) observed to occur in many rare earth intermetallics. We find several unusual features such as a two peak resistivity, anomalous absorption feature in optical conductivity etc in the crossover regime. We show that the proximity of the Hubbard band to the Fermi level is responsible for the former while the latter happens due to optical transitions into the effective f- level. The two-band (hybridization gap) model generally applied to understand the physics of these materials is shown to be inadequate in this regime. Qualitative agreement with pressure-dependent DC resistivity measurements in $CeCu_2Si_2$ is found while quantitative agreement with DC transport measurements in $CeRhIn_5$, $Ce_2Ni_3Si_5$, $CeFeGe_3$ and $YbIr_2Si_2$ is obtained. We also obtain excellent agreement with pressure dependent resistivity measurements in $YbInAu_2$ and the prototypical quantum critical system $CeCu_6$. In agreement with previous observations, we find that increasing pressure pushes Cerium materials to mixed-valence while the Yb materials cross over to the Kondo lattice regime. Further, a remarkable agreement with optical conductivity experiments in $YbIr_2Si_2$ is obtained. We also infer from the agreement that $YbIr_2Si_2$ belongs to the mixed-valent regime. Investigations including $d-f$ correlations in the periodic Anderson model to understand valence transitions are discussed in the next chapter.

Chapter 3

Inter-orbital correlations and valence fluctuations

3.1 Introduction

In recent years, quantum critical phenomena have been one of the focal points for the condensed matter community. Many rare earth inter-metallic compounds, which are also heavy fermions can be tuned easily to a quantum critical point by application of external perturbations like magnetic field and pressure [5]. $YbRh_2Si_2$ [85] and $CeCu_2Si_2$ [86] are a few examples. The periodic Anderson model (PAM) is the paradigm for studying these kind of systems. There are two possible theoretical scenarios for achieving quantum phase transitions in heavy fermion alloys [87], namely (a) competition between Kondo interaction (which is local in nature) and the non-local RKKY interactions and (b) Kondo destruction (KD) leading to sharp valence transition and consequently a quantum phase transition. However, it has been shown in previous chapter 2 that within the PAM, while a smooth valence crossover is possible, there is no possibility of a valence transition for a smooth

change in model parameters.

The extended periodic Anderson model (EPAM) [88], which includes a Coulomb repulsion (U_{fc}) between conduction (c) and localised electrons (f) naturally captures the second scenario and has been studied using mean field theory for spin independent EPAM [89], slave-boson (SB) mean-field theory [88] and dynamical mean-field theory (DMFT) using exact diagonalization (ED) [90] as the impurity solver. Nevertheless, the model parameters reported for the occurrence of the transition are physically inaccessible. Recently, a continuous time quantum Monte-Carlo within DMFT [91] study of the broken symmetry phases in the particle-hole symmetric EPAM was also carried out, but the valence transition was not studied.

We have employed a static mean-field Hartree-Fock (HF) approach as well as a dynamical local moment approach (LMA) [21] within DMFT [16, 30] to explore valence transitions within the framework of an EPAM. Within the HF approximation, we find a first order transition in average occupancy of f- electrons by tuning f- orbital energy at a critical inter orbital Coulomb interaction U_{fc}. With LMA, we find that in specific parameter regimes of the EPAM, a quantum critical point (QCP) governed by valence fluctuations exists. Additionally, this parameter regime in which we get the signature of transition is physically accessible unlike HF theory. We have reported the behaviour of low energy scale and density of states across the valence transition. The large spectral weight transfers found in dynamical quantities should be observable in photoemission experiments.

3.2 Model and formalism

The EPAM extends the usual PAM by considering an additional Coulomb interaction between localised electrons and conduction electrons. In the standard second

quantised notation, the model may be represented by the following Hamiltonian:

$$\begin{aligned}\hat{H} =&\epsilon_c \sum_{i\sigma} c^\dagger_{i\sigma} c_{i\sigma} - t \sum_{(ij),\sigma} c^\dagger_{i\sigma} c_{j\sigma} + V \sum_{i\sigma} (f^\dagger_{i\sigma} c_{i\sigma} + \text{h.c.}) \\ &+ \sum_{i\sigma} (\epsilon_f + \frac{U_f}{2} f^\dagger_{i\bar{\sigma}} f_{i\bar{\sigma}}) f^\dagger_{i\sigma} f_{i\sigma} + U_{fc} \sum_{i\,\sigma\sigma'} n^c_{i\sigma} n^f_{i\sigma'} \end{aligned} \tag{3.1}$$

The first two terms correspond to the site and kinetic energy of the conduction electrons. The third term hybridises the local (f) and itinerant (c) electrons. The fourth term represents f- orbital energy and Coulomb repulsion cost of double occupancy. The last term represents Coulomb repulsion between c- and f- electrons. Within DMFT [16, 30], which is exact in the limit of infinite dimensions D, the hopping t_{ij} must be rescaled as $t_{ij} \propto t_*/\sqrt{D}$. Next, we present Hartree-Fock (HF) mean field theory for EPAM.

3.2.1 Static mean field approach

As mentioned in the previous chapters, the starting point of LMA is an unrestricted Hartree Fock mean field theory in the paramagnetic regime. This is equivalent to an alloy-analogy approach or the Hubbard-III approximation. The mean-field PAM can then be exactly solved. For the EPAM, we have employed the Hartree approximation to decouple the additional U_{fc} term. The local f- and c- Green's functions within this approach are given by

$$G^f_\sigma(\omega) = \left[\omega^+ - \tilde{\epsilon_f} - \frac{U_f n_f}{2} + \frac{U_f \sigma |\mu|}{2} - \frac{V^2}{\omega^+ - \tilde{\epsilon_c} - S(\omega)}\right]^{-1} \tag{3.2}$$

$$G^c_\sigma(\omega) = \left[\omega^+ - \tilde{\epsilon_c} - \frac{V^2}{\omega^+ - \tilde{\epsilon_f} - \frac{U_f n_f}{2} + \frac{\sigma U_f |\mu|}{2}} - S(\omega)\right]^{-1}, \tag{3.3}$$

where $\tilde{\epsilon_f} = \epsilon_f + Un_c$, $\tilde{\epsilon_c} = \epsilon_f + Un_f$; $S(\omega)$ is the Feenberg self-energy, calculated self-consistently with Eqs. (3.4) and (3.3) (see below). The average occupancies of the f- and c- electrons, denotes as n_f and n_c, are derived self-consistently using the spectral functions, $D_\sigma^{f/c}(\omega) = -\frac{1}{\pi}\mathrm{Im}G_\sigma^{f/c}(\omega)$. The magnetic moment of f-electrons, $\left(|\mu| = \int_{-\infty}^{0} d\omega \left[D_\uparrow^f(\omega) - D_\downarrow^f(\omega)\right]\right)$ is also computed self-consistently. As for the PAM in the previous chapter, the local c- Green's function can be written in terms of Hilbert transform as

$$G^c(\gamma) = \int_{-\infty}^{\infty} d\epsilon \frac{\rho_0(\epsilon)}{\gamma - \epsilon} = H\left[\gamma\right] = \frac{1}{\gamma - S(\omega)} \tag{3.4}$$

where $H[\gamma]$ denotes the Hilbert transform of γ with respect to the non-interacting density of states $\rho_0(\epsilon)$. While $\gamma = \omega^+$ in the $V = 0$ limit, for a finite V as in present case, it is given by

$$\gamma_\sigma = \omega^+ - \tilde{\epsilon_c} - \frac{V^2}{\omega^+ - \tilde{\epsilon_f} - \frac{U_f n_f}{2} + \frac{\sigma U_f |\mu|}{2}} \,.$$

The non-interacting density of states has been chosen to be $\rho_0(\epsilon) = \theta(t_* - |\epsilon|)\sqrt{1 - \epsilon^2/t_*^2}/(2\pi t_*)$. The full c- Green's function can also be written as

$$G^c(\omega) = \frac{1}{2}\left[\frac{1}{\gamma_\uparrow - S(\omega)} + \frac{1}{\gamma_\downarrow - S(\omega)}\right] \tag{3.5}$$

With Eqs. (3.4), (3.5) and (3.3), we may compute $G^c(\omega)$ and $S(\omega)$ self-consistently.

In the next subsection, we will describe the LMA formulation, that attempts to incorporate dynamical corrections beyond the static MF approach described here.

3.2.2 Dynamical corrections: Local moment approach

In the previous subsection, we decoupled the inter-orbital interaction term within Hartree approximation. This resulted in a renormalization of the conduction and localised electron site energies as $\tilde{\epsilon_c} = \epsilon_c + U_{fc} n_f$ and $\tilde{\epsilon_f} = \epsilon_f + U_{fc} n_c$, where n_c and n_f are average occupancies for conduction and localised orbitals respectively. In going beyond the static approach, we will build the dynamical self-energies via the local moment approach, which incorporates transverse spin fluctuations to all orders. A point to note is that the occupancies, n_c and n_f are derived from the full interacting Green's function, and hence must be obtained self-consistently. In this sense, the present approach is equivalent to carrying out a skeleton expansion of the U_{fc} term about the PAM upto the first order. With the renormalized self-energies, the retarded Green's functions within DMFT for the localised and conduction electrons are given respectively by (2)

$$G^f(\omega) = \left[\omega^+ - \tilde{\epsilon_f} - \Sigma(\omega) - \frac{V^2}{\omega^+ - \tilde{\epsilon_c} - S(\omega)}\right]^{-1} \tag{3.6}$$

$$G^c(\omega) = \left[\omega^+ - \tilde{\epsilon_c} - S(\omega) - \frac{V^2}{\omega^+ - \tilde{\epsilon_f} - \Sigma(\omega)}\right]^{-1} \tag{3.7}$$

where $\Sigma(\omega)$ is the momentum independent f- self-energy. The spectral functions are given by $D^\alpha(\omega) = -\mathrm{Im}G^\alpha(\omega)/\pi$ and the occupancies are given by $n_\alpha = 2\int_{-\infty}^{0} d\omega\, D^\alpha(\omega)$. $S(\omega)$ is the Feenberg self-energy, that may be calculated self-consistently through Eq. (3.4) where $\gamma(\omega) = \omega^+ - \tilde{\epsilon}_c - V^2[\omega^+ - \tilde{\epsilon}_f - \Sigma(\omega)]^{-1}$.

As mentioned above, the local f- self-energy is calculated using LMA. The method of calculation is exactly the same as described in the previous chapters. In this work, we have investigated valence transitions in the EPAM using the static and dynamic approaches described above. The only difference with our previous

works, in terms of implementation, is that we have maintained a constant n_{tot} as the f- level is varied.

3.3 Results and discussion

3.3.1 Static approach

In this section, we present results of EPAM obtained using the static approach described in section 3.2.1. In figure 3.1, we show the average f- occupancy $n_f = \sum_\sigma \langle f^\dagger_{i\sigma} f_{i\sigma} \rangle$ as a function of the bare f- orbital energy, ϵ_f. In the absence of Coulomb repulsion between the f- and c- electrons, i.e. $U_{fc} = 0$, there is a smooth crossover from KL ($n_f \sim 1$) to an empty orbital regime ($n_f \sim 0$). With an increase in U_{fc}, the crossover becomes sharp and for a critical value of $U_{fc} = U^C_{fc}$, a first order transition is seen. The precise value of the critical U_{fc} depends on the values of U and V. Thus, the static mean field approach yields a line (surface) of quantum critical points in the $U - U_{fc}$ plane ($U - V - U_{fc}$ volume). Further, we present the behaviour of f- spectral function for the crossover and the transition regime. In left panel of figure 3.2, f- spectral functions have been shown for zero local Coulomb repulsion between f- and c- electrons. Spectral weight transfer to the right of Fermi-level takes place smoothly with increasing f- orbital energy . In the right panel of figure 3.2, we show f- spectral functions for various f- orbital energies and a U_{fc} value close to the transition (shown in figure 3.1). For a small change in f- orbital energy, there is a large transfer of spectral weight to the right of Fermi level which is evidently due to the first order transition of the average impurity occupancy.

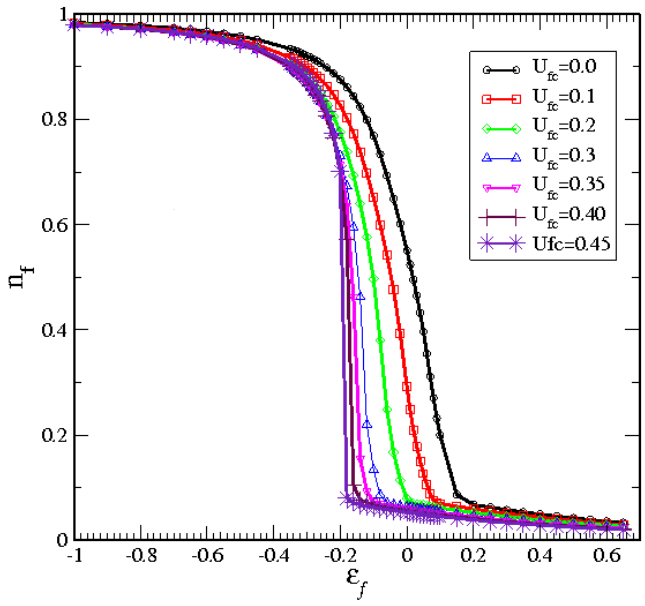

Fig. 3.1: Variation of f- orbital occupancy with f- orbital energy for different U_{fc} values. The model parameters are $U = 9.0, V^2 = 0.05$.

3.3.2 LMA results

In figure 3.3, we show the variation of f- occupancy (n_f) with the f- level (ϵ_f) energy for various values of U_{fc}. The total filling is fixed at $n_{tot} \sim 1.5$. It is seen that n_f decreases with increasing ϵ_f for all U_{fc}. However, with increasing U_{fc}, the decrease becomes steeper. This is reflected in the valence susceptibility, shown in the inset of figure 3.3, which is approaching a divergent form with increasing U_{fc}. The model parameters (in units of $t_* = 1$) are $U = 5.3$, $\epsilon_c = 0.5$ and $V^2 = 0.6$. These numbers for the parameters are motivated by our earlier works on the PAM [41], wherein we have successfully compared theory with experiments. Thus, the model parameters have modest values and are physically accessible.

The inverse of the maximum susceptibility as a function of U_{fc}, shown (as filled

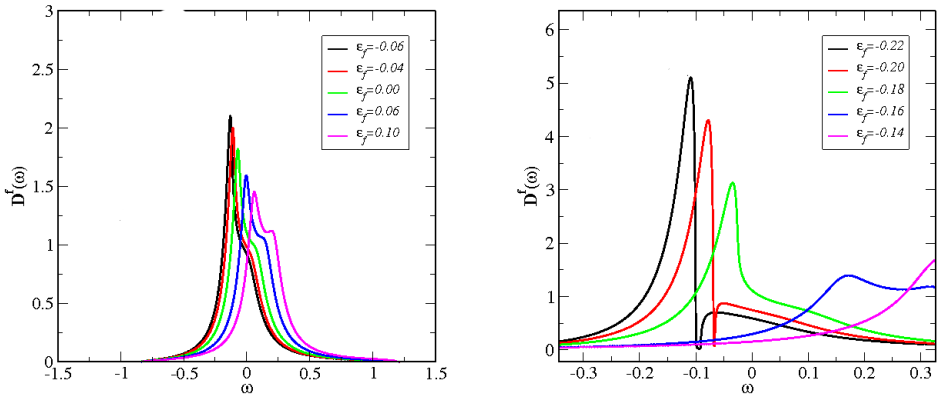

Fig. 3.2: The f- spectral function for various f- orbital energies. $U_{fc} = 0$ in the left panel, while $U_{fc} = 0.4$ in the right panel. The other model parameters are the same as in figure 3.1.

squares) in figure 3.4, decreases linearly and, if extrapolated (dashed line), vanishes at a critical $U_{fc}^C \sim 1$. This is a signature of a valence fluctuations driven quantum critical point. Although the same scenario is obtained at static mean field level, as seen in our results above and also obtained in previous works [88], the critical range of parameters is so extreme (for $U_{fc}^C \sim 1$), that hardly any experimental systems would correspond to them. Even in the ED calculations [75], the parameter regime explored was such that the $U/V^2 \sim 500$, because at lower values, the Kondo lattice regime was found to be unstable. As seen above, we start from very realistic values of U, V and ϵ_c, and the U_{fc}^C obtained is also a small fraction of the U scale, and is of the order of the bandwidth (t_*), in agreement with previous theoretical works. Since the critical valence fluctuations (CVF) model predicts the transition to occur in unreasonably large parameter values, the authors of a recent experimental study on $CeCu_2Si_2$ [92] propose that the discrepancy between the experimental findings and the predictions of CVF model could be due to the absence of certain non-local

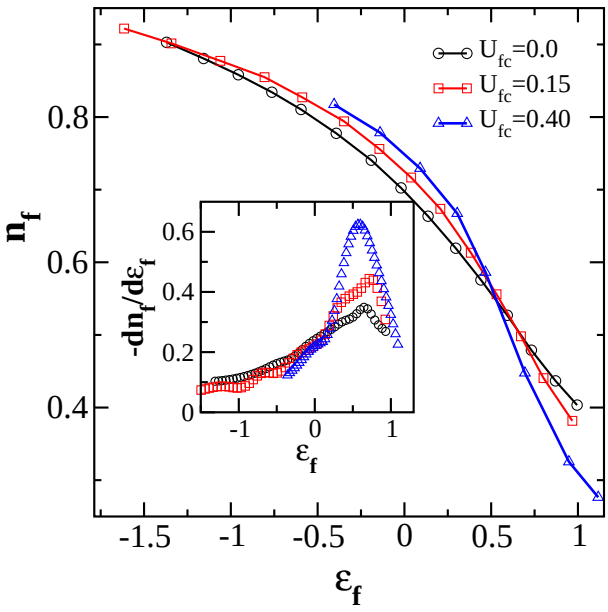

Fig. 3.3: Variation of f- orbital occupancy (main panel) and valence susceptibility (inset) with f- level, ϵ_f, for various values of U_{fc}. The other model parameters are $U \sim 5.3$, $\epsilon_c = 0.5$ and $V^2 = 0.6$.

terms in the model. Here, we show that without the need to include such terms, it is sufficient to include dynamical fluctuations beyond static mean-field for a realistic and experimentally relevant description of the pressure-induced valence changes. It is important to understand the variation of the low energy coherence scale across this crossover. As is well-known, the coherence scale is given by $\omega_L = ZV^2/t_*$, where $Z = (1 - \partial\Sigma/\partial\omega)|^{-1}_{\omega=0}$ is the quasiparticle weight. In figure 3.5 we have shown the variation of quasiparticle weight with varying ϵ_f for various values of the inter orbital Coulomb interaction, U_{fc}. The Z increases sharply as the f- level moves up in energy. We observe another trend for the change in Z. For any fixed ϵ_f below the critical point, the Z increases with increasing U_{fc}, while above the critical point, the low energy scale and U_{fc} are anti-correlated. Thus very close to the transition point, the quasiparticle weight is almost independent of changes in U_{fc}. It would be interesting to see such an 'isosbestic point' in experiments. Since

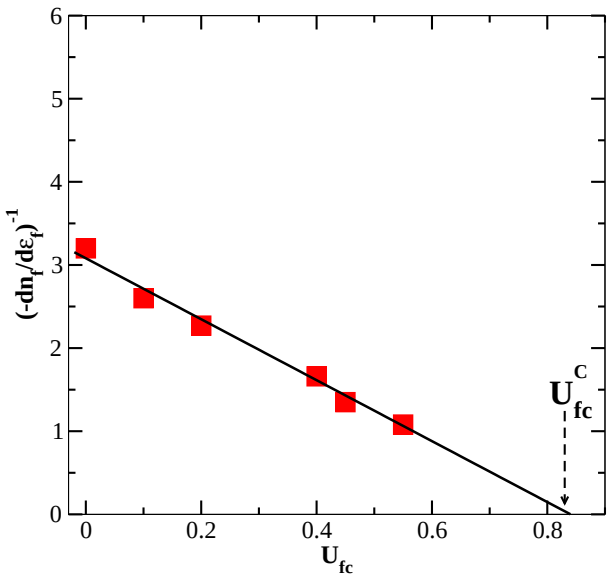

Fig. 3.4: The black squares are inverse of maximum valence susceptibility (obtained from figure 3.3) as a function of U_{fc}. The dashed line is a linear fit extrapolated to the critical value at which the susceptibility would diverge. The model parameters are same as figure 3.3.

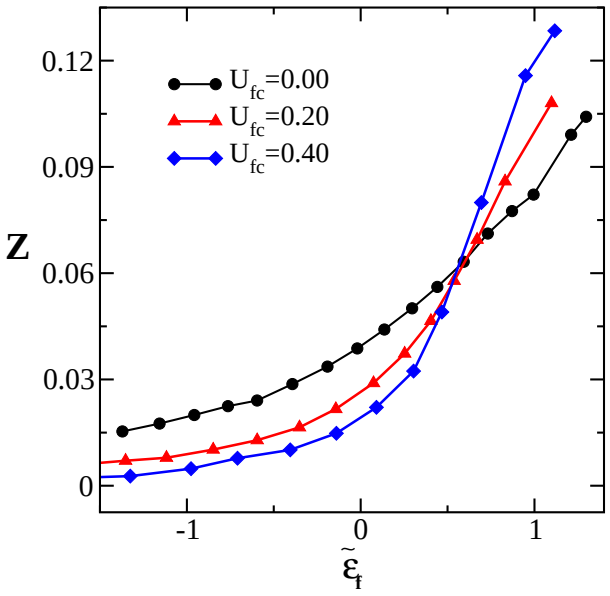

Fig. 3.5: The quasiparticle weight as a function of the effective f- level, $\tilde{\epsilon}_f$ for various U_{fc}. The model parameters are same as figure 3.3.

the scale and the valence change significantly across the crossover, we must expect that the density of states (DOS) might exhibit large scale spectral weight transfers. Indeed, as shown in the main panel of figure 3.6, the DOS changes significantly across the crossover. With decreasing n_f, the lower Hubbard band moves towards the Fermi level and gets broader, while the upper Hubbard band moves away and gets sharper. As seen from the inset, where an expanded view of the low frequency region is shown, the Kondo resonance at the Fermi level broadens significantly. This is as expected from figure 3.5 where the Z increases with decreasing n_f, and the width of the resonance is proportional to Z.

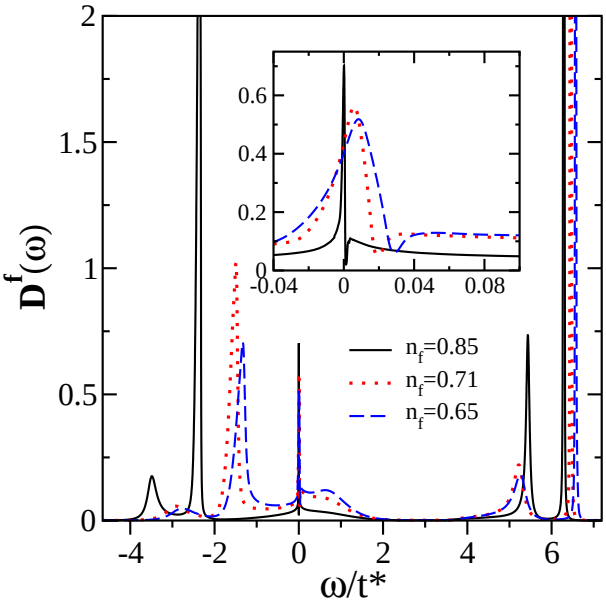

Fig. 3.6: Main panel: The f- density of states as a function of the frequency for different f- level, ϵ_f positions, corresponding to different n_f values, as mentioned in the legends. The U_{fc} value is fixed at 0.5 and the rest of the model parameters are same as figure 3.3. Inset: An expanded view of the spectra in the main panel at low frequencies.

3.4 Conclusions

The extended periodic Anderson model has been proposed as one of the prime candidate Hamiltonians for describing valence transitions and a new form of quantum criticality in heavy fermion and mixed-valent systems. However, the critical point found in previous theoretical investigations lies in model parameter regimes that would not be physically realizable. We present investigations of the EPAM within DMFT using a highly accurate local moment approach as the impurity solver. Our results clearly suggest that the inclusion of dynamical fluctuations beyond static mean field theories are crucial to making the critical point physically accessible. The low energy Kondo scale changes significantly across the valence crossover, and the single-particle spectra also show concomitant large scale weight transfers. These changes must be easily observable in angle resolved photoemission spectroscopy experiments. Finite temperature investigations are of future consideration and will be important to resolve issues such as the temperature dependence of the valence changes across the quantum critical point under the second superconducting dome in $CeCu_2Si_2$.

Chapter 4

A local moment approach for the degenerate multi-orbital periodic Anderson model

4.1 Introduction

The single-band, single-orbital periodic Anderson model (SB-SO-PAM) is a minimalistic model that is commonly employed to understand various physical properties of heavy fermion compounds. Although it has been used successfully to explain optical and thermodynamic properties of some heavy fermion alloys [40, 41, 93], a majority of HFs do not lie within the purview of this simple model. The localized f- orbital responsible for the anomalous properties of the HF materials is, in reality, highly degenerate. Although crystal fields reduce it, degeneracy nevertheless remains, and must be taken into account as an important consideration. In real materials, the number of bands crossing the Fermi level is also more than one, and thus the model appropriate for a large class of HFs would be the multi-band,

multi-orbital periodic Anderson model (MB-MO-PAM).

Unlike the multiorbital Hubbard model, theoretical work on the MO-PAM is scant. A generalization of the usual PAM, where the conduction orbital is also considered correlated, has been investigated using multi-orbital methods using various groups. Recently, Sato *et al.* [94] have studied the degenerate MO-PAM using the linearised version of DMFT. The authors have calculated the renormalization factor, spectral functions, spectral gap and local correlation functions for various sets of parameters. They have explored the continuous change from Kondo insulator to Mott insulator with increasing correlation strength of conduction electrons for a particular set of model parameters. In an other important work on multiorbital PAM by Koga *et al.* [95], NRG within DMFT has been employed to explore quantum phase transitions in a two orbital periodic Anderson model. The authors find a first order transition from Kondo insulator to Mott insulator by tuning Hund's coupling between the orbitals.

The local moment approach (LMA) outlined in the introduction and employed in the previous as well as the subsequent chapters of this thesis is specifically aimed at solving the single-band single-orbital impurity Anderson model. When combined with dynamical mean field theory (DMFT) [16], we get a non-perturbative handle on the SB-SO-PAM. But, as explained above, the plain LMA is inadequate for investigating multi-orbital systems. In this chapter, we take the first step towards realistic modeling of HFs by employing a modified LMA, that is a generalization of the single-orbital LMA, and is aimed at solving the degenerate multi-orbital single-impurity Anderson model. Such a modified LMA was formulated by Logan and co-workers [96]. The orbital energies and the on-site intra-orbital Coloumb repulsion (U) were considered to be same for all the degenerate orbitals. Although the approach allows the inter-orbital Coulomb repulsion (U') to be different than

U, Hund's coupling is ignored in the existing formulation. The approach was used to solve the multi-orbital Anderson impurity model, and the results were benchmarked against numerical renormalization group results. Excellent agreement was obtained, thus extending the reliability of the physically transparent, and easily implementable LMA to the case of multi-orbitals, albeit degenerate. We carry this forward in the present chapter and combine the multiorbital LMA (MO-LMA) with DMFT, thus achieving a powerful method to solve the very difficult problem presented by the MO-PAM.

The chapter is structured as follows: we present the model and formalism in the next section. The results obtained from the application of MO-LMA to the degenerate, multi-orbital single impurity Anderson model are briefly reviewed and benchmarked against earlier results in section 4.3.1. Subsequently, we present the spectra and transport of the multi-orbital periodic Anderson model in section 4.4, as obtained through MO-LMA+DMFT. Finally, we conclude in section 4.5.

4.2 Model and formalism

The degenerate multi-orbital periodic Anderson model (MO-PAM) in standard second quantized notation can be expressed as

$$\begin{aligned}\hat{H} = &\sum_{\mathbf{k}m\sigma}(\epsilon_{\mathbf{k}}+\epsilon_c)c^{\dagger}_{\mathbf{k}m\sigma}c_{\mathbf{k}m\sigma} + V\sum_{im\sigma}(f^{\dagger}_{im\sigma}c_{im\sigma}+\text{h.c}) \\ &+\epsilon_f\sum_{im\sigma}n^f_{im\sigma} + U\sum_{im}n^f_{im\uparrow}n^f_{im\downarrow} + \frac{U'}{2}\sum_{im\neq m';\sigma\sigma'}n^f_{im\sigma}n^f_{im'\sigma'}\ , \end{aligned} \tag{4.1}$$

where $\mathbf{k}$ is the momentum index; i is the site-index, m is the orbital and σ is the spin-index. The maximum value of m can be N which is the number of degenerate orbitals. Inclusion of spin degeneracy makes the Hamiltonian invariant under

SU(2N) symmetry, if $U = U'$. The first term represents the N-band metallic host with dispersion $\epsilon_{\mathbf{k}}$ and orbital energy ϵ_c; with the values of $\epsilon_{\mathbf{k}}$ and ϵ_c taken to be the same for all conduction bands. Note that m has been used as a conduction band index as well. The second term is the local hybridization between the metallic host and the corresponding impurity orbital. The third term is the orbital energy for f- electrons. The last two terms represent local intra- and inter-orbital Coulomb repulsion respectively. Since the U' does not depend on the electron spins, $\sigma.\sigma'$, it is implicit that Hund's coupling has been ignored. The main reason for choosing such a specific representation of MO-PAM is that the MO-LMA formulation is specifically designed for the single-impurity version of the above mentioned lattice Hamiltonian. Thus, our objective of combining DMFT and MO-LMA can be realised in a straightforward way for the MO-PAM expressed by Eq. (4.1).

Next, we will briefly discuss the local moment approach for multi-orbital SIAM as described in detail in previous works [96].

4.2.1 Local moment approach for multiorbital SIAM

Within DMFT, the MO-PAM of Eq. (4.1) can be mapped to the degenerate, multi-orbital single-impurity Anderson model (MO-SIAM) which may be represented as

$$\begin{aligned}\hat{H} =& \sum_{\mathbf{k}m\sigma}(\epsilon_{\mathbf{k}}+\epsilon_c)c^{\dagger}_{\mathbf{k}m\sigma}c_{\mathbf{k}m\sigma} + \sum_{\mathbf{k}m\sigma} V_{\mathbf{k}}(f^{\dagger}_{m\sigma}c_{\mathbf{k}m\sigma} + \text{h.c}) \\ &+ \epsilon_f \sum_{m\sigma} n^f_{m\sigma} + U\sum_m n^f_{m\uparrow}n^f_{m\downarrow} + \frac{U'}{2}\sum_{m\neq m';\sigma\sigma'} n^f_{m\sigma}n^f_{m'\sigma'}\,. \end{aligned} \tag{4.2}$$

It is easy to see that the MO-SIAM is very similar to the MO-PAM (Eq. 4.1). The only difference is in the site-index for f- electrons, which is absent in the former, but present in the latter. The terms have the same physical interpretation

as the MO-PAM. The model has particle-hole symmetry when $\epsilon_f = -U/2 - (N-1)U'$ (derived in appendix B), where N is total number of the orbitals. Thus an asymmetry parameter can be defined (for $U = U'$) as $\eta = 1 + 2\epsilon_f/((2N-1)U)$. As detailed in Ref. [96], the local f- (impurity) Green's function in the paramagnetic case for orbital m can be written as

$$G^f_m = \frac{1}{2}\left[G^f_{m\uparrow} + G^f_{m\downarrow}\right]. \tag{4.3}$$

where the spin-dependent local f- Green's function is given by

$$G^f_{m\sigma} = \left[\omega^+ - \epsilon_f - \tilde{\Sigma}_\sigma(\omega) - \Delta(\omega)\right]^{-1} \tag{4.4}$$

and $\Delta(\omega) = \sum_{\mathbf{k}} V^2_{\mathbf{k}}/(\omega^+ - \epsilon_{\mathbf{k}})$ is the hybridization function. The self-energy is given by the sum of the static and dynamical parts as

$$\tilde{\Sigma}_{m\sigma}(\omega) = +\frac{Un}{2} + (N-1)U'n - \frac{1}{2}\sigma U|\bar{\mu}| + \Sigma_{m\sigma}(\omega)\,. \tag{4.5}$$

For the symmetric case (p-h condition), the retarded quantities obey the symmetries: $\tilde{\Sigma}_{m\sigma}(\omega) = -\tilde{\Sigma}^*_{m\bar{\sigma}}(-\omega)$ and thus, $G^f_{m\sigma}(\omega) = -G^{f*}_{m\bar{\sigma}}(-\omega)$. The structure of the dynamical self-energy for the N orbital single impurity Anderson model within MO-LMA (detailed in Ref. [96]) is given as

$$\Sigma_{m\sigma} = \Sigma^{\sigma\bar{\sigma}}_{m\sigma}(\omega; U) + (N-1)\left[\Sigma^{\sigma\bar{\sigma}}_{m\sigma}(\omega; U') + \Sigma^{\sigma\sigma}_{m\sigma}(\omega; U')\right]. \tag{4.6}$$

where, at zero temperature, the time-ordered self-energy is given by

$$\Sigma^{\sigma\sigma'}_{m\sigma} = \frac{U^2}{2\pi i}\int_{-\infty}^{\infty} d\omega_1 \Pi^{\sigma\sigma'}(\omega_1)\mathcal{G}_{m\sigma'}(\omega + \omega_1) \tag{4.7}$$

Note that the subscript index m is really not relevant for the present case under consideration, which is of *degenerate* orbitals. The full time-ordered polarisation propagator $\Pi^{\sigma\sigma'}$ of Eq. (4.7) can be written in closed form using a random phase approximation as

$$\Pi^{\sigma\sigma'}(\omega) = \frac{{}^0\Pi^{\sigma\sigma'}}{1 - U\,{}^0\Pi^{\sigma\sigma'}} \tag{4.8}$$

with

$${}^0\Pi^{\sigma\sigma'} = -\frac{1}{2\pi i}\int_{-\infty}^{\infty} d\omega_1 \mathcal{G}^T_{\sigma}(\omega_1)\,\mathcal{G}^T_{\sigma'}(\omega_1 - \omega). \tag{4.9}$$

where $\mathcal{G}^T(\omega)$ is the time-ordered counterpart of $\mathcal{G}(\omega) = (\omega^+ - \epsilon - \sigma x - \Delta(\omega))^{-1}$. Here, $\epsilon_f = \epsilon - U/2 - (N-1)U'$ is the effective f- orbital energy and $x = U|\mu|/2$. Since we have considered retarded quantities throughout, we use the following procedure to evaluate the polarization propagator and the self-energy. The imaginary part of ${}^0\Pi^{\sigma\sigma'}$ in Eq. (4.9) can be written as

$$\frac{1}{\pi}\mathrm{Im}{}^0\Pi^{\sigma\sigma'}(\omega^+) = \int_{-\infty}^{\infty} d\omega_1 \mathcal{D}_{\sigma}(\omega_1)\mathcal{D}_{\sigma'}(\omega_1 - \omega)\left[\theta(\omega_1 - \omega) - \theta(-\omega_1)\right], \tag{4.10}$$

where $D_\sigma(\omega) = -1/\pi \mathrm{Im}\mathcal{G}_\sigma(\omega)$ and the real part can be calculated through Kramers-Kronig transformation

$$\mathrm{Re}{}^0\Pi^{\sigma\sigma'}(\omega) = -\mathcal{P}\int_{-\infty}^{\infty} \frac{d\omega_1}{\pi}\frac{\mathrm{Im}{}^0\Pi^{\sigma\sigma'}(\omega_1)}{\omega - \omega_1}\,. \tag{4.11}$$

This is converted to a time-ordered form simply by multiplying the imaginary part by $\mathrm{sgn}(\omega)$, and then used in Eq. (4.8) to get the RPA sum. The resulting $\Pi^{\sigma\sigma'}$ is time-ordered, and thus, its imaginary part is positive-definite. This is then used in

finding the imaginary part of the retarded part of the self-energy (Eq. (4.7)) by

$$\frac{1}{\pi}\Sigma_{\sigma}^{\sigma\sigma'}(\omega^{+}) = -U^{2}\int_{-\infty}^{\infty} d\omega_{1}\ [\theta(-\omega_{1})\theta(\omega+\omega_{1}) + \theta(\omega_{1})\theta(-\omega-\omega_{1})] \\ \mathcal{D}_{\sigma'}(\omega+\omega_{1})\mathrm{Im}\Pi^{\sigma\sigma'}(\omega_{1}). \tag{4.12}$$

The real part of the retarded self-energy is calculated using Kramers-Kronig transformation, thus the full self-energy is given by $\Sigma_{\sigma}^{\sigma\sigma'} = \mathrm{Re}\Sigma_{\sigma}^{\sigma\sigma'}(\omega) - i\mathrm{Im}\Sigma_{\sigma}^{\sigma\sigma'}(\omega)$. To ensure Fermi-liquid behaviour at low energy, symmetry restoration must be carried out, which is equivalent to enforcing adiabatic continuity to the non-interacting limit. The approach is similar to the corresponding one for the single orbital SIAM [21, 22]. We will briefly discuss symmetry restoration condition here.

4.2.2 Symmetry restoration

In parallel to the local moment approach for single orbital SIAM, the symmetry restoration condition for multiorbital SIAM is

$$\tilde{\Sigma}_{m\uparrow}(\omega=0) = \tilde{\Sigma}_{m\downarrow}(\omega=0). \tag{4.13}$$

In addition, to ensure the analyticity of RPA transverse spin polarization propagator, the following condition must be satisfied.

$$|\mu_{0}| \leq |\mu| = \frac{2x}{U} \leq 1 \tag{4.14}$$

We solve Eqs. (4.13) and (4.14) numerically for various set of model parameters keeping $U'/U \leq 1$.

4.3 Results for the single impurity Anderson model

The multiorbital SIAM has been considered in detail previously [96], but just to recapitulate and benchmark, we display our results for the MO-SIAM in section 4.3.1 below. The one difference in terms of models between our work and the previous work by Logan and co-workers [96] is that we have considered either a Gaussian or semi-elliptic density of states, while the previous work used a flat band.

4.3.1 $SU(2N)$ symmetry: $U = U'$

In this section, we present our results for the single impurity Anderson model with degenerate multiorbitals and $U = U'$. We will benchmark our numerical implementation with earlier work [96], which itself has been extensively benchmarked with numerical renormalization group (NRG) approach with excellent agreement. The specific choice for the number of orbitals will be 2 with $U = U'$, hence we will present results for the $SU(4)$ Anderson model. As mentioned before, our choice of conduction band density of states for calculating the hybridization $\Delta(\omega)$, is a Gaussian ($\rho_0(\epsilon) = \frac{1}{\sqrt{\pi}\,t*} \exp([-\epsilon/t*]^2)$) which is appropriate for a hypercubic lattice in infinite dimensions. First, we present the $f-$ spectral functions and discuss their features in different frequency regimes.

In figure 4.1, the spectral function for $SU(4)$ single impurity Anderson model has been shown for different Coulomb repulsions, i.e. $U = 6.0, 7.0$ and 8.0. The spectral functions have been plotted versus the absolute frequency $(\omega/t*)$. Pinning of the spectral function at $\omega = 0$ ensures the Friedel sum rule for $SU(4)$ SIAM at half-filling. For comparison, we have shown the spectral function for $SU(2)$ SIAM with solid line. We first analyse the high frequency behaviour (in the left panel of figure 4.1). The Hubbard bands for $SU(4)$ SIAM are much broader compared

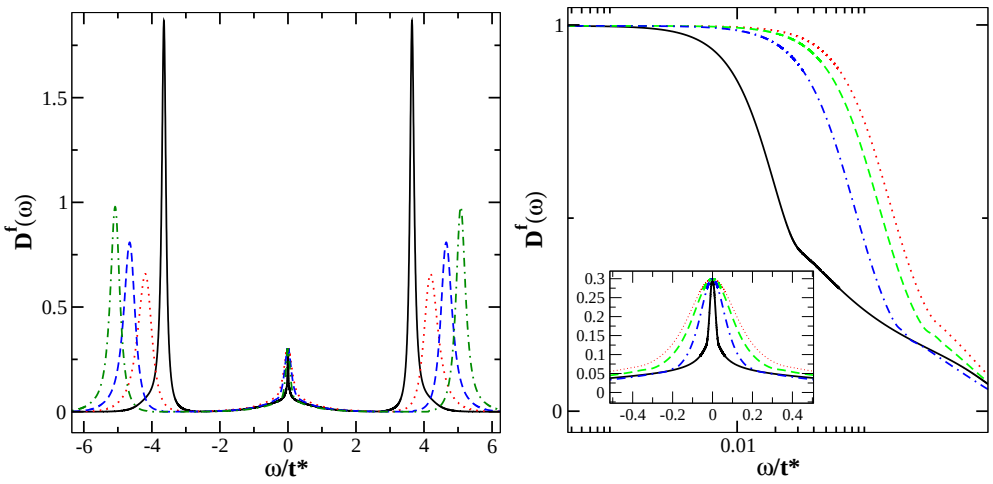

Fig. 4.1: The f- spectral functions for a two orbital $SU(4)$ Anderson model for $U = 6.0, 7.0$ and 8.0 (dotted, dashed and dotted dashed lines respectively). The $SU(2)$ Anderson model spectral function has also been shown for $U = 5.4$ with solid line. $V^2 = 0.6$ has been chosen for all the U values. Left panel: All scales showing a three peak structure. Right panel: Expanded view of the spectra in the left panel near $\omega = 0$. The inset shows the narrowing of the Kondo resonance with increasing U.

to the $SU(2)$ SIAM. As mentioned in detail in Ref. [96], the number of relaxation channels contributing to the lifetime broadening of the Hubbard bands increase with the number of orbitals, i.e. N and the width of a Hubbard band is proportional to $(N+1)\Delta_0$ ($\Delta_0 = \mathrm{Im}\Delta(\omega = 0)$). In the right panel of figure 4.1, the low frequency structure of the spectral function for $SU(4)$ single impurity Anderson model has been shown for various Coulomb repulsion values. The main panel depicts the positive part of the Kondo resonance peak on a logarithmic scale (for the sake of clarity). In the inset of the right panel, the full resonance peak has been shown, which has pinning at $\omega = 0$ confirming the satisfaction of the Friedel sum rule. Next, we will discuss the variation of low energy scale for $SU(2)$ and $SU(4)$ SIAM with Coulomb repulsion U in the strong coupling regime ($\eta \sim 0; U/\Delta_0 >> 1$).

The low energy scale, i.e. $\omega_L = ZV^2$ ($Z = (1 - \frac{\partial \Sigma_m}{\partial \omega})$) is proportional to the full width at half maximum of the central resonance peak. The ω_L scale for the

$SU(2N)$ SIAM in strong coupling limit is known to be exponentially dependent on $-U/\Delta_0$, the precise expression for which has been derived in Ref. [96] and is reproduced below:

$$\omega_L \overset{U/\Delta_0 \to \infty}{\sim} c(N) U \exp(-\frac{\pi U}{8N\Delta_0}) \ , \tag{4.15}$$

where $c(N)$ is a constant prefactor for given N. The low energy scale is seen to be strongly dependent on the number of orbitals. The above result agrees with slave-rotor mean-field theory, where in a $1/N$ dependence of the argument of the exponential is known from analytical results of $SU(2N)$ model in strong coupling [96]. We have carried out MO-LMA calculations, and we would like to benchmark our implementation against the above result. Thus, to validate our numerical finding against Eq. (4.15), we show $\log(\omega_L/U)$ versus U/Δ_0 for $SU(2)$(squares) and $SU(4)$(diamond) models for large U/Δ_0 in figure 4.3. The solid lines are the prediction of Eq. (4.15) with constant $c(N)$ (obtained through fitting) for different N. The numerical results are seen to be in excellent agreement with the predictions of Eq. (4.15).

In strong coupling, the spectral functions are expected to exhibit a scaling collapse onto a universal form when plotted in terms of scaled frequency (ω/ω_L). In figure 4.2, we show the same spectra as in the figure 4.1, but as a function of the scaled frequency, ω/ω_L. The spectra for the $SU(4)$ model do seem to collapse on a single universal form. Also shown as a solid line is the scaling spectrum for the $SU(2)$ Anderson impurity model, which is seen to be quite different from that of the $SU(4)$ model. In practice, the spectrum for the SU(2) model was computed with $U = 5.4$ and $V^2 = 0.6$.

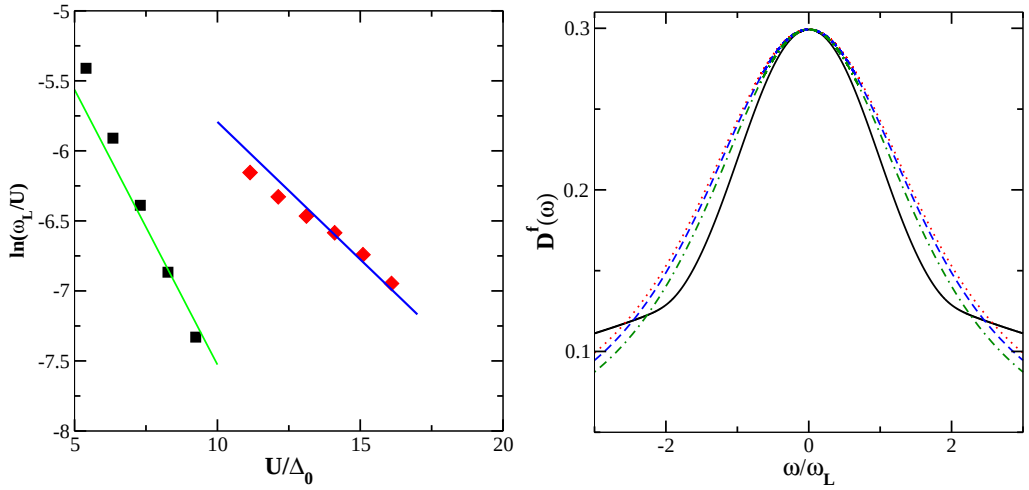

Fig. 4.2: Left panel: Validating the numerical implementation; Comparison of our numerical result (squares and diamonds for the $SU(2)$ and $SU(4)$ models respectively) with the prediction of Eq. (4.15) (solid lines). Right panel: The same spectra as in figure 4.1 versus scaled frequency ω/ω_L appear to collapse onto a single universal function with increasing U. Spectral function for $SU(2)$ Anderson model (solid line) has a scaling form that is very different than that of the $SU(4)$ model.

4.3.2 $(SU(2))^N$ symmetry: $U \neq U'$

In the previous section, we explored the multiorbital Anderson impurity model with same inter and intra-orbital Coulomb repulsion. In this section, we have considered intra-orbital repulsion to be different from inter-orbital repulsion ($U \neq U'$). In this case, the multiorbital SIAM does not have $SU(2N)$ symmetry, but has $(SU(2))^N$ symmetry. In practice, we choose $U' = \alpha U$, where $\alpha < 1$. The complete structure of the self-energy is given by Eq. (4.6). However, in the strong coupling limit $U/\Delta_0 >> 1$, the last term in Eq. (4.6) can be neglected (as shown in Ref. [96]). The two remaining terms involve a polarisation propagator, namely $\Pi^{\sigma\bar{\sigma}}(\omega; U)$ and $\Pi^{\sigma\bar{\sigma}}(\omega; U')$. Each of these two propagators generate a distinct scale when $U \neq U'$. Thus, a two-scale picture emerges for a multi-orbital Anderson impurity model when the intra-and inter-orbital Coulomb repulsion energies are different ($\alpha < 1$). These two scales manifest in the spectral function as kinks, which are shown in

figure 4.3, where only the $\omega > 0$ part of the spectral function has been shown, and the two scales are marked. For the specific parameters considered in the figure, namely $\alpha = 0.95, V^2 = 0.4$ and $U = 5.35$, the two scales are separated by one order of magnitude.

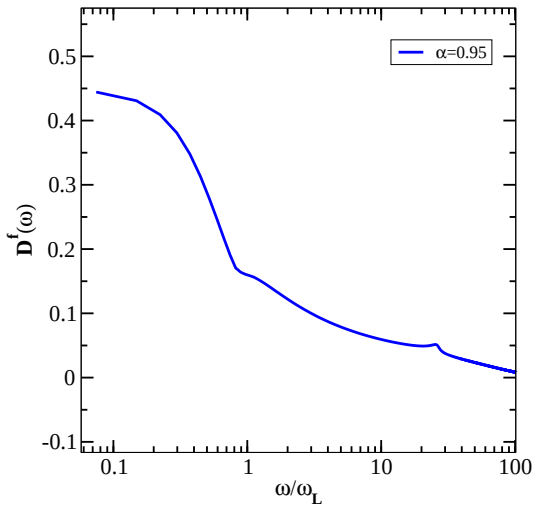

Fig. 4.3: Positive part of f– spectral function with different inter-orbital and intra-orbital Coulomb repulsion, i.e. $SU(2)^2$ SIAM with $U' = 0.95U$. $U = 5.35$ and $V^2 = 0.4$.

Given that our implementation reproduces the previously known results, we now move on to the multiorbital PAM by combining dynamical mean field theory (DMFT) with MO-LMA.

4.4 Multiorbital periodic Anderson model

Like the single orbital periodic Anderson model, the multiorbital PAM (Eq. (4.1)) can be mapped on to a multiorbital SIAM (Eq. (4.2)) using dynamical mean field theory (DMFT). The local Green's functions for c- and f- electrons are given by

$$G^f(\omega) = \left[\omega^+ - \epsilon_f - \Sigma(\omega) - \frac{V^2}{\omega^+ - \epsilon_c - S(\omega)}\right]^{-1} \tag{4.16}$$

$$G^c(\omega) = \left[\omega^+ - \epsilon_c - S(\omega) - \frac{V^2}{\omega^+ - \epsilon_f - \Sigma(\omega)}\right]^{-1} \tag{4.17}$$

The local Green's functions are calculated in the same way as described in chapter 1. The momentum independent self-energy $\Sigma(\omega)$ has been calculated using the local moment approach for multiorbital SIAM as discussed in previous sections, with the difference that the propagators that are used to build the self-energy are the host Green's functions found through the Dyson's equation in each DMFT iteration. Thus, the Feenberg self-energy, $S(\omega)$, which is self-consistently determined, is used to construct the hybridization function, $\Delta(\omega) = V^2/(\omega^+ - \epsilon_c - S(\omega))$. Until now, we have considered the symmetric SIAM, for which the conduction band is symmetrically placed about the chemical potential, and $\eta = 0$. In the following however, we will consider the $p-h$ asymmetric case, implying that $\epsilon_c \neq 0$ and/or $\eta \neq 0$. Thus, the c- and f- occupancies would be, in general, non-integral. We will present the results separately for $U = U'$ and $U \neq U'$ cases in the following two subsections.

4.4.1 $SU(2N)$ symmetry: $U = U'$

In this section, we have focused on the f- spectral function of the $SU(4)$ PAM. In the left panel of figure 4.4, the f- spectra have been shown for $U \sim 6.20$, $U \sim 7.20$ and $U \sim 8.20$ as functions of absolute frequency $\omega/t*$. For comparison, the f- spectral function of $SU(2)$ PAM has also been shown for $U \sim 5.2$ (solid line). The spectra for the $SU(4)$ case are qualitatively very similar to the $SU(2)$ PAM. A three peak structure is seen; with two Hubbard bands at $\omega \sim \epsilon_f \sim -U/2$ and $\omega \sim \epsilon_f + U/2$. The only remarkable difference between the two cases is visible in the inset of figure 4.4. The width of the Kondo resonance for the $SU(4)$ PAM is much larger than that of the $SU(2)$ PAM even though the U values chosen are much

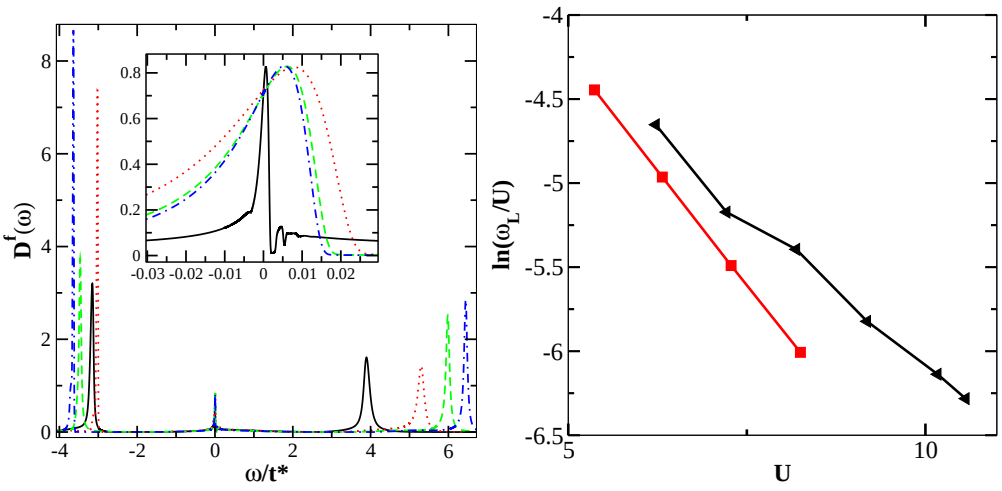

Fig. 4.4: Left panel: The f- electrons spectra versus absolute frequency ($\omega/t*$) for $SU(4)$ PAM with $U \sim 6.20$ (dotted), $U \sim 7.20$ (dashed) and $U \sim 8.20$ (dotted dashed). For comparison, the f- spectral function of the $SU(2)$ PAM has been shown with solid line. Inset: Same spectra as the main panel have been shown, but with an expanded view of the low frequency region, to show the Kondo resonance clearly. The model parameters are $V^2 = 0.6, \epsilon_c = 0.5$ for which $n_c \sim 0.5$ and $n_f \sim 1$. Right panel: Low energy scales for the $SU(2)$ and $SU(4)$ asymmetric periodic Anderson model with square and diamond symbols respectively.

larger for the former than the latter. This is reflected in the low energy scales for the two cases. The fact that the $SU(4)$ case has much larger scales than the $SU(2)$ case for the same U value can be understood by the $1/N$ factor in the low energy scale expression, Eq. (4.15). We show the ω_L scales in the right panel of figure 4.4. The scales for the PAM are also seen to decrease exponentially with increasing U. Further, we show the f- spectral function with scaled frequency ω/ω_L in figure 4.5 for $SU(2)$ and $SU(4)$ PAM. The scaling forms for the f- spectral functions of $SU(2)$ and $SU(4)$ cases are quite distinct, as also was found for the impurity Anderson models.

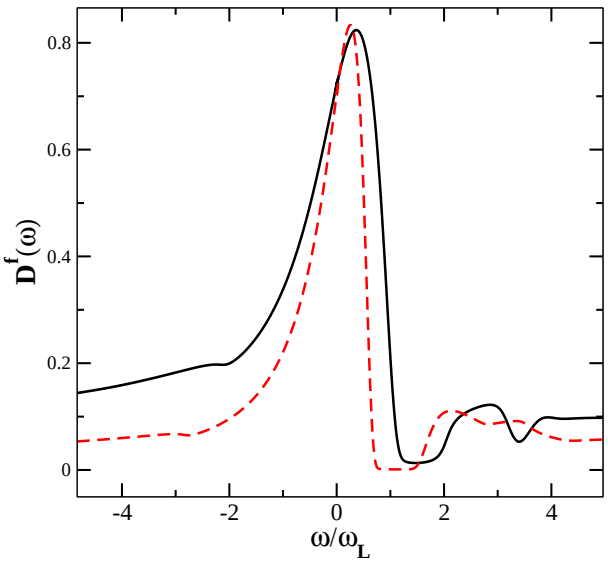

Fig. 4.5: Kondo resonance peak (low energy feature) versus scaled frequency ω/ω_L for $SU(2)$ (solid line) ($U \sim 7.20$) and $SU(4)$ (U$\sim$ 10.0) (dashed line).

4.4.2 $(SU(2))^N$ symmetry: $U \neq U'$

In figure 4.6, the $\omega > 0$ part of the f- spectral functions for $SU(4)$ ($U = 5.23$) and $(SU(2))^2$ ($U' = 4.70$) have been shown with solid and dotted lines respectively. Like the $(SU(2))^2$ SIAM, we observe a kink in spectral function at $\omega 1 \sim 11\omega_L$ for $(SU(2))^2$ PAM. Thus we conclude that there are two energy scales in $SU(2)^N$ PAM too.

4.5 Conclusions

In this chapter, we have combined the well benchmarked local moment approach for multiorbital SIAM with the dynamical mean field theory to explore the degenerate multiorbital periodic Anderson model. We reproduce the previous results of local moment approach for SIAM, which itself has been benchmarked with numerical renormalization approach. We have explored the $SU(4)$ PAM for different values

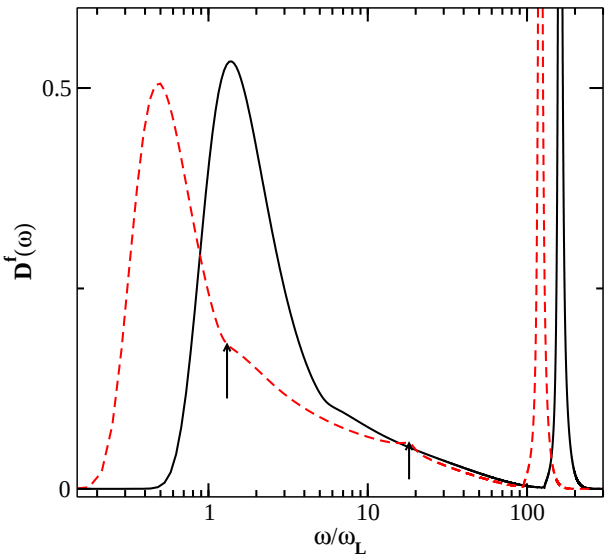

Fig. 4.6: Positive part of f- spectral function versus scaled frequency ω/ω_L on logarithmic scale for $SU(2)$ (solid line)and $SU(2)^2$ (dashed line) ($U \sim 5.20$ and $U' \sim 4.70$). Model parameter $\epsilon_c = 0$ and $V^2 = 0.4, n_c \sim 1$ and $n_f \sim 1$.

of Coulomb repulsion and compared it with $SU(2)$ PAM. The universal scaling form of PAM spectra tail depends strongly on the number of orbitals. In the present approach, we have not accounted for the Hund's coupling between the orbitals. The extension of multiorbital LMA with inclusion of Hund's coupling and crystal field effects remains an aspect of future consideration.

Chapter 5

Kondo hole route to incoherence in heavy fermions

5.1 Introduction

The concentration of f- electrons in heavy fermion alloys can be tuned by substituting non magnetic homologues. For example, Lanthanum can be substituted for Cerium. Various examples of such alloys are $Ce_{1-x}La_xCu_6$ [97], $Ce_{1-x}La_xB_6$ [98], $Ce_{1-x}La_xCu_2Si_2$ [53], and $Yb_{1-x}Lu_xRh_2Si_2$ [99] etc. Doping with non-magnetic homologue, defined as Kondo-hole (KH) type substitution, leads to a crossover from coherent lattice to incoherent single impurity behaviour. Such a crossover is reflected in dynamics and transport properties.

The other kind of doping in heavy fermions is ligand field substitution, as in $CeCu_{6-x}Au_x$ [100] and $UCu_{5-x}Pd_x$ [101]. This kind of doping in the former leads to a quantum critical point, that in turn manifests in a wide parameter space at finite temperatures and leads to anomalous properties.

The coherent potential approximation (CPA) is an extensively used approxi-

mation for theoretical investigations of substitutional doping and the consequent disorder [102–104]. By embedding the CPA within the dynamical mean field theory (DMFT) framework, a dynamical CPA (dCPA) may be formulated [105, 106]. The disordered PAM has been studied using various impurity solvers such as slave boson (SB) theory [8], numerical renormalization group (NRG) [105] and iterative perturbation theory (IPT) [106]; with most studies focusing on KH type disorder. Miranda and Dobrosavljevic [8] have proposed that disorder induces a distribution of the Kondo scales and have employed SB theory to explain linear resistivity behaviour occurring in a few uranium based heavy fermion alloys. Within the dCPA framework, Grenzebach *et al.* [105] have used NRG, while T. Mutao [106] has used IPT to study the resistivity and thermopower behaviour for Kondo hole and ligand field type disorder over the entire range of $x \in [0, 1]$. The aforementioned crossover from coherent to incoherent behaviour was also thoroughly investigated [105,107,108]. It has been found theoretically that for the KH-type doping, the crossover occurs at an x value that is roughly the same as the conduction electron filling $(1 - n_c)$ [107, 108]. Slave-boson mean-field theory has been employed to study KH-type disorder and numerical simulations of mean field equations have been carried out on a square lattice up to 20×20 sites for different n_c and n_f. The disadvantage with CPA is that inter-site coherence and coherent back scattering effects are ignored and hence Anderson localization cannot be incorporated. Statistical DMFT and typical medium theory are the extensions beyond CPA that can take into account these effects.

In the present chapter, we have studied the periodic Anderson model (PAM) within dCPA using local moment approach (LMA) [21] as an impurity solver. The dCPA is implemented through the Feenberg renormalized perturbation series (FRPS). The Kondo hole sites are considered non interacting, while those with $f-$

orbitals are treated with LMA. While we find agreement with previous theoretical studies using similar methods, we conclude that quantitative agreement with experimental results necessitates the introduction of *doping dependence* into the model parameters. Experimentally measured residual resistivity per unit concentration of magnetic impurities increases with increasing disorder [97,98]. However, in all previously reported theoretical work [105,106,109,110] the residual resistivity peaks at a certain doping value, and is not monotonic. We have found that including doping dependence into the conduction orbital energy correctly reproduces the known experimental trend in residual resistivity.

The chapter is structured as follows; we first discuss the standard model for heavy fermions, i.e. periodic Anderson model, followed by the formalism of CPA+DMFT which is needed to incorporate Kondo hole disorder. In section 5.3.1, we present results discussing spectral functions, low energy scale and hybridization with various disorder values. In section 5.3.2, we discuss the behaviour of optical conductivity with disorder. In sections 5.3.3 and 5.3.4, we show resistivity and thermoelectric behaviour for different disorder values in the $n_f \sim 1$ regime. In final section 5.4, we have done a detailed comparison of theoretical result with the experimental data for resistivity and thermopower in $Ce_{1-x}La_xB_6$.

5.2 Model and formalism

5.2.1 Periodic Anderson model

The periodic Anderson model has been discussed earlier in the chapters 3 and 4. It is the simplest theoretical model to understand the physics of heavy fermions in various regimes. In second quantized notation, the PAM is expressed as

$$H_{PAM} = -\sum_{\langle ij\rangle\sigma} t_{ij}\left(c^{\dagger}_{i\sigma}c_{j\sigma} + \text{h.c}\right) + \sum_{i} H_{ii} \tag{5.1}$$

where $H_{ii} = \epsilon_c \sum_\sigma c^{\dagger}_{i\sigma}c_{i\sigma} + \epsilon_f \sum_\sigma f^{\dagger}_{i\sigma}f_{i\sigma} + V(\sum_\sigma f^{\dagger}_{i\sigma}c_{i\sigma} + \text{h.c}) + Un_{fi\uparrow}n_{fi\downarrow}$. For a detailed description of various terms in the PAM, we refer the reader to chapter 1.

In order to handle disorder within DMFT, we use the coherent potential approximation (CPA) which becomes exact in the limit of infinite dimensions [102]. We outline our method for incorporating disorder below.

5.2.2 Coherent potential approximation and dynamical mean field theory

We have employed Feenberg renormalized perturbation series (FRPS) [43] for binary distribution of disorder, i.e. $P(\epsilon_i) = (1-x)\delta(\epsilon_i - \epsilon_A) + x\delta(\epsilon_i - \epsilon_B)$ (where ϵ_i can be any model parameter) and derived averaged local conduction and impurity Green's function for PAM. The tight binding Hamiltonian which is expressed in second quantized notation as

$$\hat{H} = -\sum_{ij\sigma} t_{ij}c_{i\sigma}c_{j\sigma} + \sum_{i\sigma}\epsilon_c c_{i\sigma}c_{i\sigma} \tag{5.2}$$

represents kinetic energy and orbital energy. Green's function in matrix representation is given by the following equation,

$$\mathbf{g} = [\mathbf{z}+\mathbf{t}]^{-1} \tag{5.3}$$

where $z_{ij} = \delta_{ij}(\omega - \epsilon_c)$. The local Green's function for the Hamiltonian using FRPS can be written as

$$g_{ii} = \frac{1}{\omega - \epsilon_c - S_i[g_{jj}(\omega)]} \tag{5.4}$$

where S_i is a Feenberg self-energy given by the sum of all self-avoiding paths on the lattice, where the vertices are the local (site-excluded) Green's functions, while the lines are the hopping amplitudes connecting neighbouring sites. In the limit of infinite-dimensions, the restriction of site-exclusion may be relaxed. Thus, for example, for the Bethe lattice, where the only self-avoiding closed paths would be a single-hop to a nearest neighbour, the $S(\omega)$ would be a functional only of the nearest neighbour local (diagonal) Green's functions. The Dyson's equation for an interacting system is given as

$$G_{ii;\sigma} = g_{ii}(\omega) + \sum_{jk} g_{ij}\Sigma_{jk;\sigma}(\omega)G_{ki;\sigma}(\omega) \tag{5.5}$$

Within DMFT [16], the self-energy is momentum-independent and spatially local i.e. $\Sigma_{ij;\sigma}(\omega) = \delta_{ij}\Sigma_{ii;\sigma}(\omega)$ and thus the local Green's function may be written as

$$G_{ii;\sigma} = g_{ii}(\omega) + \sum_{jj} g_{ij}\Sigma_{jj;\sigma}(\omega)G_{ji;\sigma}(\omega) \tag{5.6}$$

Matrix representation for above Green's function can be written as

$$\mathbf{G}_\sigma(\omega) = \mathbf{g}(\omega) + \mathbf{g}(\omega)\mathbf{\Sigma}_\sigma(\omega)\mathbf{G}_\sigma(\omega) \tag{5.7}$$

or as

$$\mathbf{G}_\sigma(\omega)) = [\mathbf{g}(\omega)^{-\mathbf{1}} - \mathbf{\Sigma}_\sigma(\omega)]^{-\mathbf{1}} \tag{5.8}$$

Combination of Eqs. (5.3) and (5.8) gives

$$\mathbf{G}_\sigma(\omega)) = [\mathbf{z} - \mathbf{\Sigma}_\sigma(\omega) + \mathbf{t}]^{-\mathbf{1}} \tag{5.9}$$

Since $\Sigma_\sigma(\omega)$ is diagonal, Green's function in matrix representation is given as

$$\mathbf{G}_\sigma(\omega)) = [\tilde{\mathbf{Z}} + \mathbf{t}]^{-\mathbf{1}} \tag{5.10}$$

with $\tilde{\mathbf{Z}} = \mathbf{z} - \mathbf{\Sigma}_\sigma$. The structure of Eqs. (5.3) and (5.10) is identical and thus the Green's function with diagonal self-energy in d= ∞ limit can be written as

$$G_{ii;\sigma}(\omega) = \frac{1}{\omega - \epsilon_c - \Sigma_{i;\sigma}(\omega) + S_i[G_{jj;\sigma}(\omega)]} \tag{5.11}$$

where S_i is exactly the same functional of local interacting Green's functions as in the non-interacting case. So far, we have not invoked any disorder. For a binary alloy, $P(\epsilon_i) = (1-x)\delta(\epsilon_i - \epsilon_1) + x\delta(\epsilon_i - \epsilon_0)$, where every site "i" is surrounded by a fraction x of '1' type sites and $1-x$ of '0' type. Thus in the Feenberg self-energy, since each vertex has a sum over the sites, the argument of the functional becomes a self-averaged quantity:

$$S_i = S\left[G^{CPA}_{jj:\sigma}\right] \tag{5.12}$$

and $G^{CPA}_{ii;\sigma}$ is the disordered averaged CPA Green's function and given as

$$G^{CPA}_{jj;\sigma}(\omega) = (1-x)G^1_{jj;\sigma}(\omega) + xG^0_{jj;\sigma}(\omega) \tag{5.13}$$

As discussed in the introduction(5.1), our focus is on substitutional disorder in $f-$ sites, and hence we choose $\epsilon_1 = \epsilon_{f;1}$ and $\epsilon_0 = \epsilon_{f;0}$. The local conduction electron

(c) Green's functions for 1 and 0 type are given by

$$G^{1}_{ii;\sigma}(\omega) = \frac{1}{\omega - \epsilon_c - \Sigma^{1}_{i;\sigma}(\omega) + S_i[G^{CPA}_{jj;\sigma}(\omega)]} \tag{5.14}$$

and likewise for '0' type. Here the $\Sigma^{1/0}_{i;\sigma} = \frac{V^2}{\omega^{+} - \epsilon_f^{1/0} - \Sigma^{f;1/0}(\omega)}$. Using Eq. (5.14) in Eq. (5.13) gives the CPA averaged Green's function

$$\begin{aligned} G^{CPA}_{ii;\sigma} = & \frac{1-x}{\omega - \epsilon_c - S_i[G^{CPA}_{ii;\sigma}] - \Sigma^{1}_{i;\sigma}(\omega)} \\ & + \frac{x}{\omega - \epsilon_c - S_i[G^{CPA}_{ii;\sigma}] - \Sigma^{0}_{i;\sigma}(\omega)} \end{aligned} \tag{5.15}$$

Within the LMA [40,44], we have a two self-energy description corresponding to the two degenerate mean-field broken symmetry solutions with self-energy Σ^{A} and Σ^{B} and hence the corresponding Green's functions will be $G^{CPA;A}_{i;\sigma}(\omega)$ and $G^{CPA;B}_{i;\sigma}(\omega)$. In the paramagnetic regime every site is surrounded by an equal number of 'A' and 'B' type Green's functions. Thus we can use the same arguments for the Feenberg self-energy, and we can write

$$G^{CPA}(\omega) = \frac{1}{2}[G^{CPA;A}_{ii;\sigma}(\omega) + G^{CPA;B}_{ii;\sigma}(\omega)] \tag{5.16}$$

With the symmetries of the Green's function the above equation can be written as

$$G^{CPA}_{ii}(\omega) = \frac{1}{2}[G^{CPA}_{ii;\sigma}(\omega) + G^{CPA}_{ii;-\sigma}(\omega)] \tag{5.17}$$

Combining Eqs. (5.15) and (5.17) and the condition of Kondo hole type of disorder, i.e. $\Sigma_{\sigma}(\omega)^{0} = \Sigma_{-\sigma}(\omega)^{0} = 0$ (since $\epsilon_{f;0} \to \infty$ for Kondo holes), the averaged local c-

CPA Green's function can be written as

$$G_c^{CPA}(\omega) = \frac{(1-x)}{2}\left[\frac{1}{\omega-\epsilon_c-S(\omega)-\Sigma_\sigma(\omega)}+\frac{1}{\omega-\epsilon_c-S(\omega)-\Sigma_{-\sigma}(\omega)}\right] + \left[\frac{x}{\omega-\epsilon_c-S(\omega)}\right]. \tag{5.18}$$

The above equation is similar to CPA+DMFT equation derived previously [105, 106]. Since the CPA Green's function corresponds to that of a translationally invariant system, the local c− CPA Green's functions can also be calculated with the following Hilbert transform

$$G_c^{CPA}(\omega) = H[\gamma] = \int_{-\infty}^{\infty}\frac{\rho_0(\epsilon)}{\gamma(\omega)-\epsilon} = \frac{1}{\gamma(\omega)-S(\omega)} \tag{5.19}$$

where $\gamma(\omega) = \omega^+ - \epsilon_c - \Sigma_c^{CPA}$. Eqs. (5.18) and (5.19) give a self-consistent equation for $S(\omega)$. The CPA Green's function for f- electrons is given by

$$G_f^{CPA}(\omega) = \frac{\Sigma_c^{CPA}(\omega)}{V^2}\left[1+\Sigma_c^{CPA}(\omega)G_c^{CPA}(\omega)\right] \tag{5.20}$$

The local Green's functions for interacting f- and c- electrons are given as

$$G_\sigma^f(\omega) = \left[\omega^+ - \epsilon_f - \Sigma_\sigma^f(\omega) - \frac{V^2}{\omega^+-\epsilon_c-S(\omega)}\right]^{-1} \tag{5.21}$$

$$G_\sigma^c(\omega) = \left[\omega^+ - \epsilon_c - S(\omega) - \frac{V^2}{\omega^+-\epsilon_f-\Sigma_\sigma^f(\omega)}\right]^{-1} \tag{5.22}$$

Evaluation of local self-energy $\Sigma^f_{\uparrow/\downarrow}$ and inclusion of DMFT is carried out in the manner discussed in detail in previous works [40, 44] and in chapters 0-3 for the clean case. For disordered systems, the CPA Green's functions are used to evaluate transport properties which have been discussed in the next section.

5.2.3 Transport formalism

Electrical ($\mathcal{J}$) and thermal ($\mathcal{J}^q$) current density can be given as [111]

$$\mathcal{J} = L^{11}\mathcal{E} + L^{12}(-\Delta T)$$

$$\mathcal{J}^q = L^{21}\mathcal{E} + L^{22}(-\Delta T)$$

where $\mathcal{E} = E + \frac{1}{e}\Delta\mu$ and ΔT are applied effective electric field and temperature gradient respectively. L^{ij} are called Lorenz numbers and are given as

$$L^{11} = \mathcal{L}^{(0)}; L^{21} = TL^{12} = -\frac{1}{e}\mathcal{L}^1; L^{22} = \frac{1}{e^2T}\mathcal{L}^2$$

The expression for $\mathcal{L}$ is

$$\mathcal{L}^\alpha = \int d\omega\, \omega^\alpha \left(-\frac{dn_F}{d\omega}\right) \tau(\omega) \tag{5.23}$$

where n_F and $\tau(\omega)$ are Fermi-function and inverse scattering rate respectively. The DC conductivity and thermopower can be expressed in terms of Lorenz numbers as

$$\sigma_{DC} = L^{11} = \mathcal{L}^0; Q = -\frac{1}{eT}\frac{L^{12}}{L^{11}} = -\frac{1}{eT}\frac{\mathcal{L}^1}{\mathcal{L}^0}$$

Since within DMFT, vertex corrections are absent [16], the single-particle Green's functions are sufficient within the Kubo formalism to obtain transport quantities such as DC resistivity and optical conductivity. The expressions have been derived previously [40] for non-disordered case. With the inclusion of disorder at CPA level, the expressions retain the same form, while the c- Green's function in the expression are replaced by the CPA Green's function. Thus the expression for the

real part of optical conductivity is given by

$$\sigma(\omega;T) = \frac{\sigma_0}{2\pi^2}\int_{-\infty}^{\infty} d\omega' \, \frac{n_F(\omega) - n_F(\omega+\omega')}{\omega} \\ \mathrm{Re}\left[\frac{G_c^{CPA*}(\omega) - G_c^{CPA}(\omega+\omega')}{\gamma(\omega+\omega') - \gamma^*(\omega)} - \frac{G_c^{CPA}(\omega) - G_c^{CPA}(\omega+\omega')}{\gamma(\omega+\omega') - \gamma(\omega)}\right] \tag{5.24}$$

where $\sigma_0 = 4\pi e^2 t^2 a^2 n/\hbar$ for lattice constant a, electronic charge e, and electron density n and $\gamma(\omega) = S(\omega) - \frac{1}{G_c^{CPA}(\omega)}$.

By carrying out a Kramers-Kronig transform of the $\sigma(\omega;T)$ we can get $\sigma'(\omega;T)$, and then the complex optical conductivity, $\bar{\sigma}(\omega;T)$, can be obtained as $\sigma(\omega;T) + i\sigma'(\omega;T)$. The optical scattering rate [48] is defined as $M^{-1}(\omega;T) = \mathrm{Re}(1/\bar{\sigma}(\omega;T))$. The explicit expression for DC conductivity(Eq. (5.25)) and thermopower coefficient Eq. (5.26) are obtained by considering the $\omega \to 0$ limit of the above equation and can be written as

$$\sigma_{DC} = \int_{-\infty}^{\infty} d\omega \, \left(-\frac{dn_F}{d\omega}\right)\tau(\omega) \tag{5.25}$$

$$Q_{DC} = \frac{Q_0}{T\sigma_{DC}}\int_{-\infty}^{\infty} d\omega \, \omega \left(-\frac{dn_F}{d\omega}\right)\tau(\omega) \tag{5.26}$$

where $n_F(\omega) = (e^{\beta\omega}+1)^{-1}$ is the Fermi function, $Q_0 = -\frac{1}{e}$; $\tau(\omega) = \frac{\sigma_0}{2\pi^2}\mathrm{Re}[\frac{\pi D_c^{CPA}(\omega)}{\mathrm{Im}\gamma(\omega)} + 2(1-\gamma(\omega)G_c^{CPA}(\omega)]$ and $D_c^{CPA}(\omega) = -\mathrm{Im}G_c^{CPA}(\omega)/\pi$ is the spectral function of the retarded CPA c- Green's function $G_c^{CPA}(\omega)$.

5.3 Results

As mentioned in the introduction, our main objective in this chapter is to elucidate the emergence of incoherence in heavy fermions through the introduction of Kondo holes. The focal theme throughout this section will be the crossover from

coherent lattice behaviour to incoherent single-impurity behaviour as a function of doping concentration. The manifestation of this crossover will be examined in single-particle quantities such as spectral functions, and two-particle quantities such as DC and optical conductivity and thermopower. It is well known that heavy fermions systems display such a crossover even in the clean limit with an increase in temperature from T=0 to beyond the lattice coherence temperature. We will examine the interplay of disorder and temperature in inducing the incoherence. We will restrict ourselves to the strong coupling Kondo lattice regime where $Ut_*/V^2 \gg 1$ and $\eta = 1 - \frac{2|\epsilon_f|}{U} \sim 0$. The conduction band centre is fixed at $\epsilon_c = 0.5$. We begin with density of states and low energy scale.

5.3.1 Density of states and low energy scale

The clean limit of the PAM has been studied extensively. It has been found that the spectral functions, optical conductivity and resistivity in strong coupling regime are universal functions of $(T/\omega_L, \omega/\omega_L)$ [38, 40, 70]. The low energy scale, which is given by $\omega_L \simeq ZV^2/t_*$ where $Z = (1-\partial\Sigma/\partial\omega|_{\omega=0})^{-1}$ is an exponentially decreasing function [21, 38] of $\frac{U}{V^2}$ (for $\eta = 1 + \frac{2\epsilon_f}{U} = 0; \frac{U}{V^2} >> 1$). In the upper panel of figure 5.1, we show the f- dos as a function of 'bare' frequency, ω/t_* for various values of the doping, x. The three peak structure of two Hubbard bands and the central Kondo resonance persists for all x. The central sharp peak is seen to diminish visibly upon increasing x, while the Hubbard bands remain almost unaffected. This may be seen more clearly in the lower panel wherein the low frequency region is shown. It is easy to see that a local redistribution of spectral weight has occurred with the increase in x, and the hybridization gap flanking the Kondo resonance fills up giving rise to a broad featureless resonance in the single-impurity limit. The full-width at half-maximum of the resonance is proportional to

the low energy scale. And given the broadening of the resonance, we must expect that the ω_L should increase with increasing x. Indeed, as the inset shows the ω_L rises almost linearly, and saturates in the single-impurity limit.

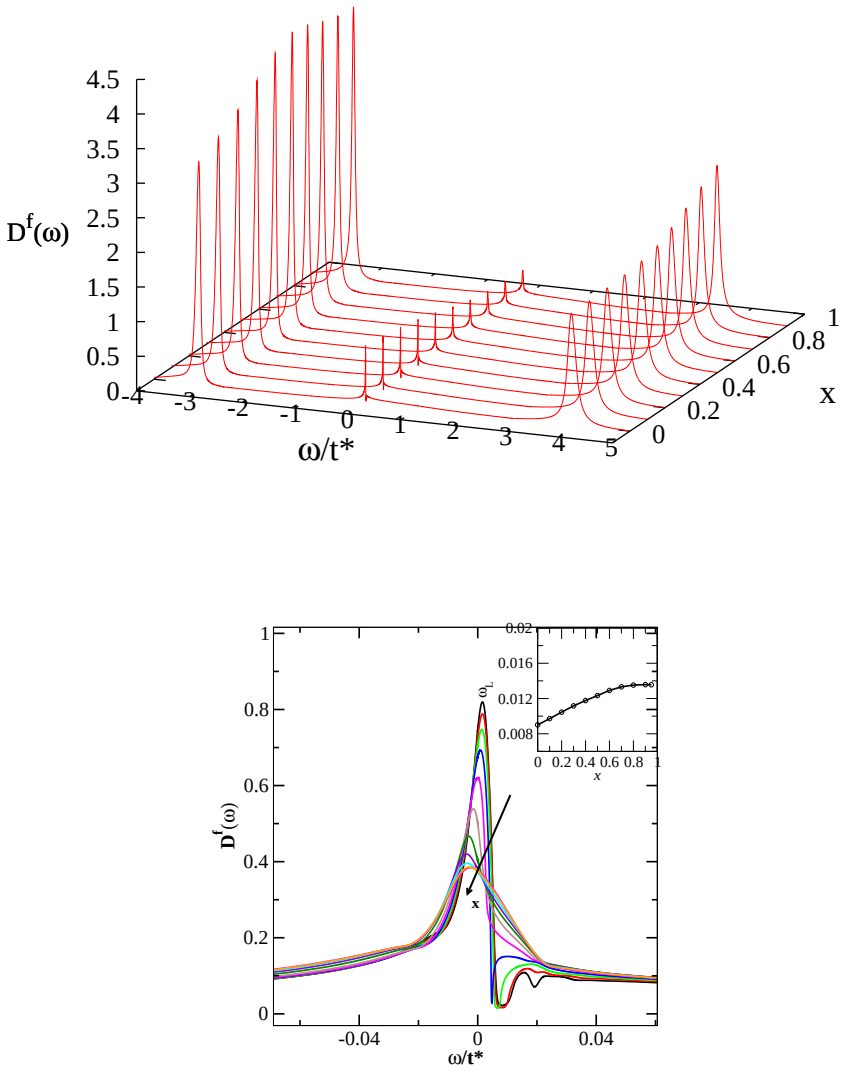

Fig. 5.1: Upper figure: f- DOS ($D^f(\omega)$) are shown as function of absolute frequency $\frac{\omega}{t*}$ with varying disorder in third axis ($U = 5.11; V^2 = 0.6, n_f \simeq 0.98, n_c = 0.59$). Lower figure: Expanded view of the central peak in the upper panel. Inset in lower figure: variation of low energy scale with disorder.

Next we discuss the dependence of hybridization function, $\Delta(\omega) = -\mathrm{Im}\,[S(\omega)]$, (where the $S(\omega)$ is the Feenberg self-energy) on dopant concentration. The $\Delta(\omega)$ may be found through the imaginary part of the inverse of the host Green's function, which is determined self-consistently within DMFT. We show the $\Delta(\omega)$ in figure 5.2. It is seen that for small values of disorder, the hybridization function has a Gaussian envelope with spectral weight carved around $\epsilon^{f*} = Z(\epsilon^f + \Sigma(0))$. With increasing disorder, the hybridization gap fills up and for large values of disorder, ($x \simeq 1$) we see a featureless Gaussian. This is natural because in the dilute limit, the impurities should have a negligible effect on the host, hence the hybridization assumes a simple form that is proportional to the non-interacting density of states, $\rho_0(\epsilon)$, which has been chosen to be a Gaussian in our work. In the next subsection, we discuss the

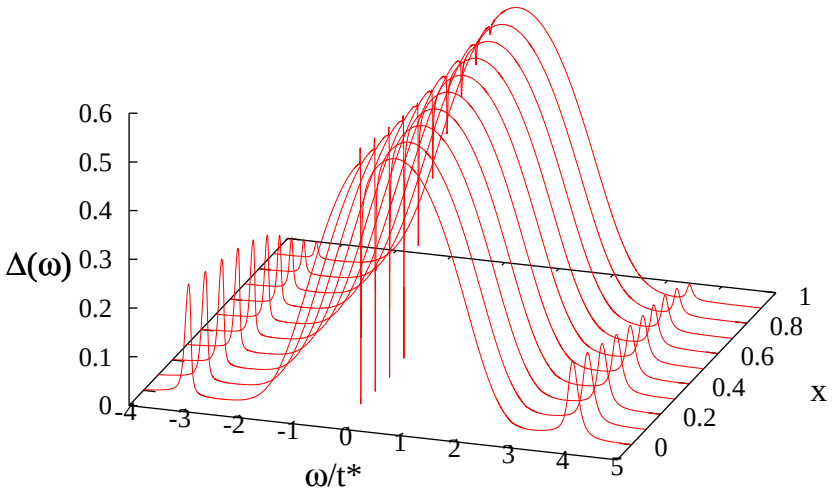

Fig. 5.2: Hybridization as a function of absolute frequency ω/t_* for different disorder values. The parameters are $U = 5.23; V^2 = 0.4; n_f = 0.98; n_c = 0.53$.

effects of disorder on response functions. We consider optics first.

5.3.2 Optical conductivity and optical scattering rate

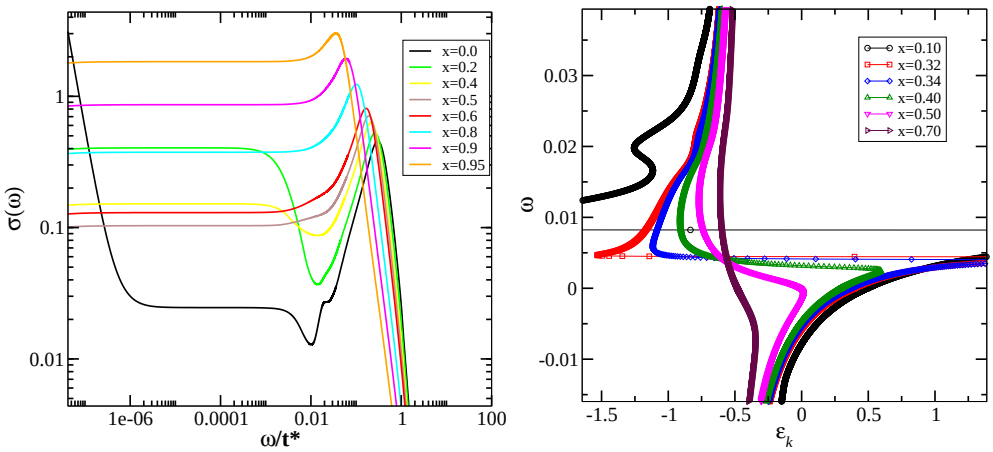

Fig. 5.3: Left panel: Zero temperature optical conductivity as a function of $\frac{\omega}{t*}$ for different disorder strength. Right panel: Dispersion curve for various disorder strengths. The model parameters are $U = 5.11; V^2 = 0.6; n_f \simeq 0.98$ and $n_c \simeq 0.59$.

In the left panel of figure 5.3, we show $T = 0$ optical conductivity computed using Eq. (5.24) for different values of x. With increasing x, the Drude peak at $\omega = 0$ melts rapidly and the the low frequency region appears flat and featureless. The DC value of the optical conductivity represents static effects of impurity scattering. The mid-infrared peak moves to lower frequencies with increase in disorder value. This is counterintuitive if we invoke the renormalized non-interacting picture, which says that the MIR peak is positioned at $\sim \sqrt{ZV^2}$. The scale increases with x, so if the MIR were to be proportional to $\sqrt{\omega_L}$, then the MIR would experience a blue shift. So how does one explain the red shift? The answer is provided by the dispersion, $\omega(\epsilon_{\mathbf{k}})$ found by plotting the position at which the $\mathbf{k}$-dependent spectrum, $A^{CPA}(\mathbf{k},\omega) = -\mathrm{Im}G_c^{CPA}(\mathbf{k},\omega)/\pi$ peaks for a fixed $\epsilon_{\mathbf{k}}$. This is shown in the right panel of figure 5.3. It is seen that for low disorder, there is a clean minimum direct gap, that is indeed proportional to $\sqrt{\omega_L}$. With increasing disorder, the direct gap fills up with mid-gap states, which causes the gap to direct excitation to decrease.

Eventually, for $x \gtrsim 0.7$, there is almost no gap. Thus, the theory predicts that with increasing substitutional disorder, the MIR absorption peak should experience a strong red shift.

In figure 5.4, we show the variation of residual resistivity, i.e. $\frac{1}{\sigma(\omega=0;T=0)}$ for a given set of model parameters(mentioned in figure caption). In the clean case ($x = 0$), the residual resistivity is zero and increases to a maximum for a disorder value of $x = 0.4$. It decreases further with increasing disorder and goes back to zero for $x \simeq 1$. We have compared our result with Nordheim's rule, according to which DC resistivity of a binary alloy is proportional to $x(1-x)$, where x is disorder strength. This behaviour is not obeyed by disordered heavy fermion alloys as evident in our comparison (and also from experiments).

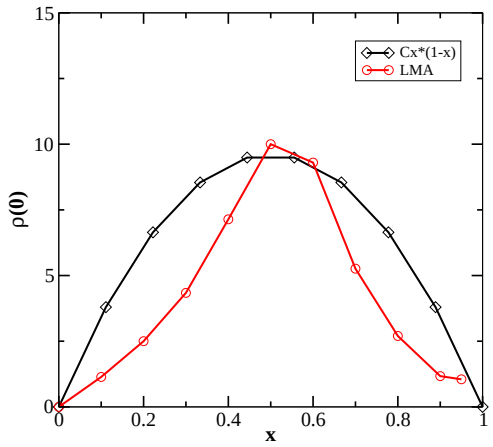

Fig. 5.4: Inverse of optical conductivity at zero temperature and zero frequency i.e. $\frac{1}{\sigma(\omega=0;T=0)}$ as function of doping. The model parameters are the same as figure 5.3.

The optical scattering rate, $M^{-1}(\omega)$, defined in section 5.2 as $M^{-1} = \mathrm{Re}(\frac{1}{\sigma(\omega)})$, is shown in figure 5.5. In the concentrated regime ($x \to 0$), a characteristic peak is visible in optical scattering rate at low frequencies. This is also observed in experiments [112–114] on heavy fermion systems. This peak is narrow and centred at ω_L for small x. As x increases, the peak broadens, experiences a red shift, and

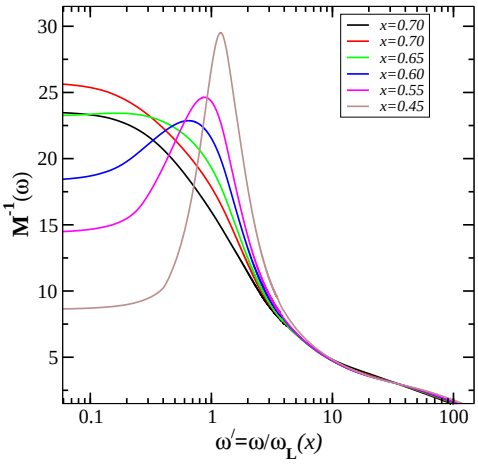

Fig. 5.5: Zero temperature optical scattering rate as a function of $\frac{\omega}{\omega_L(x)}$ for various disorder strengths. The model parameters are $U = 5.11; V^2 = 0.6; n_f \simeq 0.98$ and $n_c \simeq 0.59$.

ultimately vanishes in the dilute limit. It is precisely around a disorder value of $x \sim 0.6$, that this peak structure vanishes, which is attributed to crossover from heavy fermion to single impurity regime. The high frequency tail is seen to be universal for all x. We further investigate the effect of temperature on the optical scattering rate for finite value of disorder. In the main panel of figure 5.6, the optical scattering rate has been shown for $x = 0.45$ versus scaled frequency ω/ω_L. The peak in optical scattering rate corrodes slowly with increasing temperature, and finally vanishes for $T \gtrsim 0.5\omega_L$ for the parameters mentioned in figure 5.6. In the inset of figure 5.6, the DC resistivity *vs.* temperature has been shown for the same parameter regime. It is seen that the coherence peak appears at the same value of temperature i.e. $T \sim 0.5\omega_L$, where peak in scattering rate vanishes (main panel) and for all higher temperatures, the resistivity follows single impurity behaviour. Thus, the behaviour of optical scattering rate is consistent with resistivity in terms of predicting the crossover from Kondo lattice (KL) to single impurity. Next, we will discuss the effect of disorder on the finite temperature response functions.

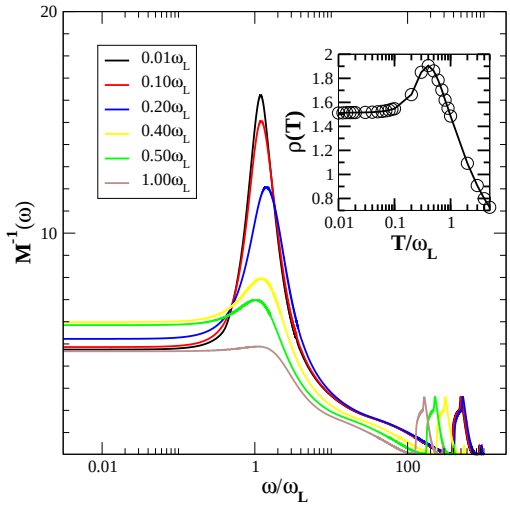

Fig. 5.6: In main panel: optical scattering rate for $x = 0.45$ and various temperatures, shown as fractions of the low energy scale. In the inset, the resistivity *vs.* scaled temperature is shown, also for $x = 0.45$. The other model parameters are $V^2 = 0.6; \epsilon_c = 0.7; \eta \simeq 0$ and $U \simeq 5.32$, $n_f = 0.98$ and $n_c = 0.59$.

5.3.3 DC Resistivity

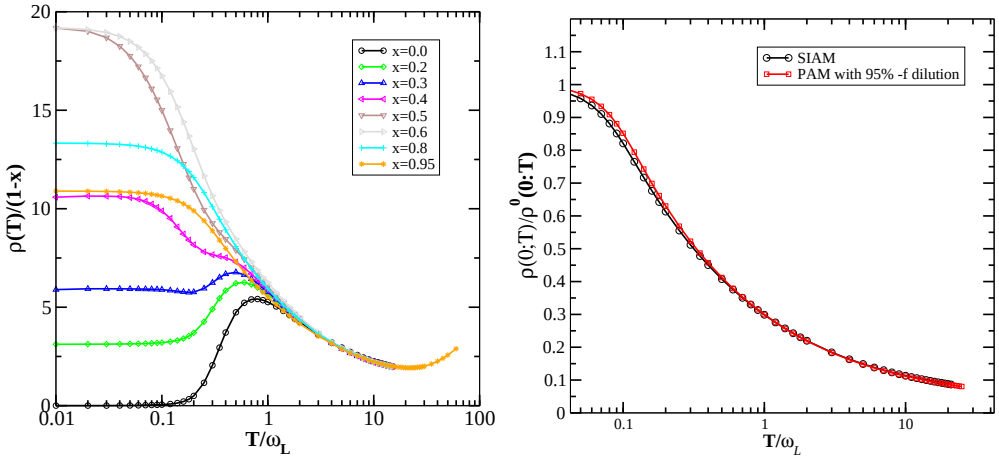

Fig. 5.7: Left panel: Resistivity per $f-$ site as a function of scaled temperature, $\frac{T}{\omega_L(x)}$. Right panel: The strong coupling single impurity Anderson model (SIAM) resistivity compared with $x = 0.95$ disordered Periodic Anderson Model (PAM) for $U = 5.11; V^2 = 0.2; \epsilon_c = 0.5$.

In the left panel of figure 5.7, the effects of disorder on DC resistivity $\rho(T)$ have been shown. For zero disorder, resistivity is zero at $T = 0$ and follows T^2 behavior

(Fermi-liquid) at low temperatures. As temperature is increased, a crossover from coherent to incoherent behavior in resistivity takes place. At large temperatures resistivity shows single impurity behaviour ($\rho(T) = \frac{3\pi^2}{16\ln^2 T/\omega_L}$) as discussed in detail in previous work [40]. For doping value of $x = 0.1, 0.2, 0.3, 0.4$, the normalised resistivity $\frac{\rho(T)}{(1-x)}$ has finite residual value at $T = 0$. It is constant for small temperatures and further crossover from coherent to incoherent behaviour takes place at higher T. For disorder strength $x > 0.4$, with decrease in temperature resistivity increases monotonically and saturates to a finite residual value. Thus, the lattice coherent behaviour never sets in for these specific parameters of PAM for $x > 0.4$. At $\frac{T}{\omega_L} >> 1$, the resistivity for all doping collapses onto a single universal form. Continuing with finite temperature response, we explore the behaviour of thermopower with disorder.

5.3.4 Thermopower

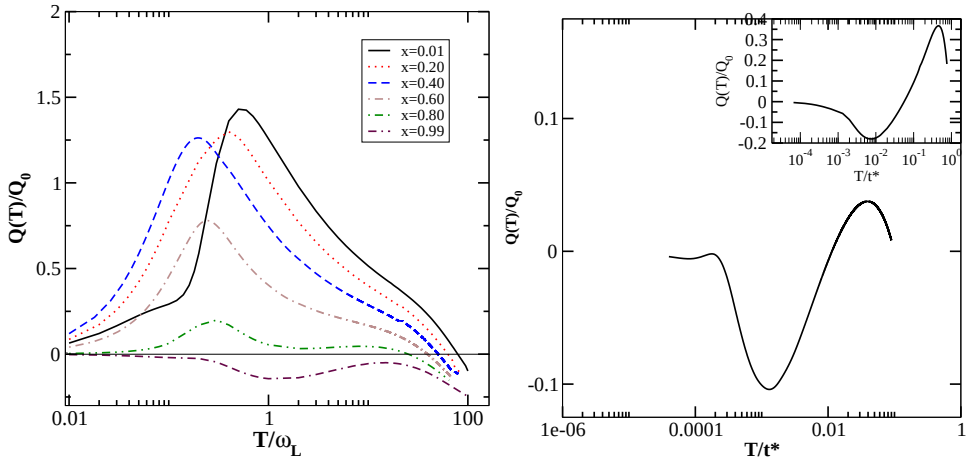

Fig. 5.8: Left panel: Thermopower *vs.* T scaled by low energy scales $\omega_L(x)$ for various x mentioned in the legend box (model parameters are $U \sim 5.23; V^2 = 0.4$). Right panel: thermopower variation with temperature scaled with $t*$ in extreme dilution i.e $x = 0.99$ with $U \sim 7.17; V^2 = 0.4$. Inset of left panel is thermopower of SIAM for $U \sim 5.80; V^2 = 0.4$.

In left panel of figure 5.8, the effect of disorder on thermopower for different temperatures has been shown. For zero disorder, the thermopower coefficient is zero for $T = 0$. With increase in temperature, it goes through a maximum value at a characteristic temperature and for higher temperature values, a change of sign occurs. As disorder increases, the position of the maximum in thermopower red shifts monotonically upto $x = 0.4$ for a given set of parameters. For the disorder strength $x > 0.4$, the peak in thermopower starts shifting towards larger temperature value, though the shift is very small. The magnitude of the peak decreases with increase in disorder and changes sign in large disorder limit. In extreme dilution limit shown in the right panel of figure 5.8, the thermopower looks qualitatively similar to that of SIAM as shown in inset of right panel, i.e. one peak at low temperature and the other peak with opposite sign at large temperature. Thermopower calculation for SIAM has been done using LMA and bench marked with NRG calculations [115].

5.4 Comparison to experiment

5.4.1 Resistivity

In previous work [41], DMFT+LMA has been employed to compare theory with experiments for a few heavy fermion metals in the clean case. Theoretical comparisons with experiment for disordered case has several complications. Introduction of disorder may change lattice parameters which effectively can change the hopping parameters, site energies and hybridization amplitudes. The precise estimation of model parameters for different disorder strengths is next to impossible and thus only qualitative comparison is possible. In figure 5.9, we have compared disorder

dependent resistivity of $Ce_xLa_{1-x}B_6$ by N. Sato *et al.* [98] with our theory. In left

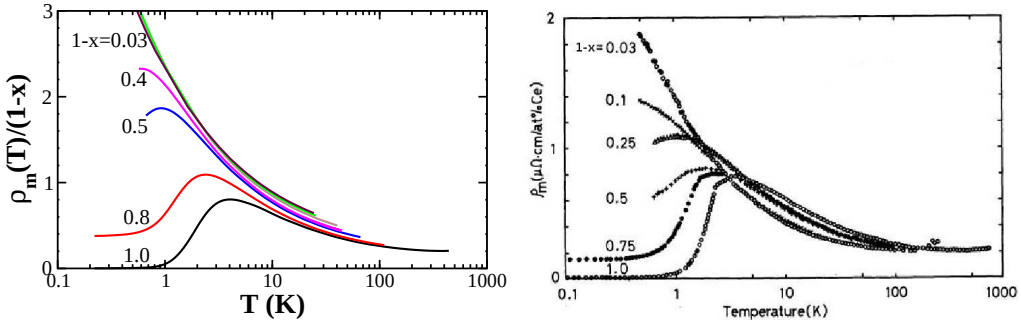

Fig. 5.9: Comparison of theory with experiment for Ce_xLa_{1-x} – Left panel: theoretically computed resistivity versus T for various x. Right panel: experimental data for $Ce_xLa_{1-x}B_6$ by Sato *et al.* [98].

panel, we present theoretical data where $n_f = 0.98$, $n_c = 0.53$ and $\frac{U}{V^2} \sim 6.0$. With the above choice of parameters and appropriate scaling (mentioned in previous work [41]), the theoretical data superimposes with experimental data (right panel of figure 5.9) for clean case. If we compute resistivities for finite x without changing the model parameters, we find that the residual resistivity peaks at a finite x; but experimentally, it is observed that the residual resistivity increases monotonically with increasing x and saturates in the dilute limit. Hence, in order to get correct trend in residual resistivity with increasing disorder, we introduce a minimal dependence of model parameter with x. Our choice is the linear dependence of x for conduction electron site energy ($\epsilon_c(x) = \epsilon_c(0) + \alpha x$, with $\alpha = 0.5$). The argument behind such a choice is that the larger atomic size of the doped lanthanum atom changes effective conduction electron site energy and hybridization. Further, the $x-$ axis is scaled by ratio of coherence peak position in theory to the experiment for zero disorder. The agreement between theory and experiment is qualitatively good.

5.4.2 Thermopower

In the upper panel of figure 5.10,a thermopower measurement by Kim *et al.* [116] of $Ce_xLa_{1-x}B_6$ for varying concentrations of Cerium is shown. The experimentally measured thermopower includes electronic (f) and lattice contributions. It is important to extract the electronic contribution in thermopower coefficient, since calculation does not include phonons. For the case of DC resistivity, the Mattheissen's rule was employed to extract the electronic contribution. For thermopower, the Nordheim-Gorter rule $S \cdot \rho = S_{La} \cdot \rho_{La} + S_{Ce} \cdot \rho_{Ce}$ is commonly employed.

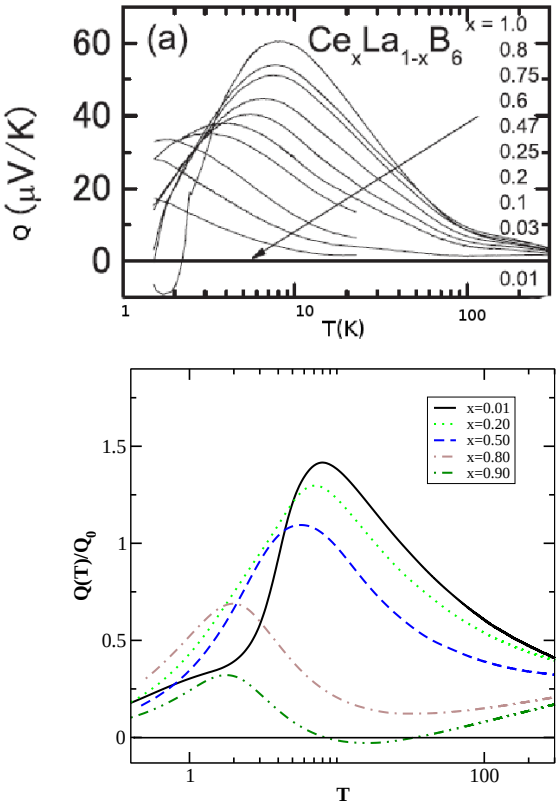

Fig. 5.10: Comparison of experiment with theory – Top panel: Experimental data for $Ce_xLa_{1-x}B_6$ by Kim *et al.* Lower panel: Theoretically computed thermopower for various x.

The contribution from the first term is small and can be neglected (as argued

in experimental work [116]). It is observed that the peak position in thermopower shifts to lower temperatures with increasing x. In the lower panel of figure 5.10, the theoretically computed thermopower is shown for the same parameter values as in figure 5.9. The x-axis of theoretical data has been scaled. Theoretical data for different disorder strengths have been scaled by ratio of the peak position in thermopower in theory to experiment for respective disorder strengths. The theory does agree with experiments. Indeed it is gratifying to note that the theoretically computed DC resistivity and thermopower agree with experiments for the same set of parameters.

5.5 Conclusions

In this chapter, we have investigated Kondo hole type of substitution in heavy fermions using CPA+DMFT+LMA. The physics issue in focus is the crossover from heavy fermions to single impurity behaviour in physical properties like resistivity and thermopower. We have used the Feenberg renormalisation perturbation series (FRPS) to derive the CPA equations. The LMA+CPA+DMFT does capture the crossover from Kondo lattice (KL) to single impurity (SI) behaviour as reflected in spectral functions, optics, resistivity, thermopower and optical scattering rate. Comparison of our theoretical results with experimental data for resistivity and thermopower yields qualitatively good agreement. A disorder dependent conduction orbital energy correctly captures the experimental trend in resistivity and thermopower. CPA does not capture inter site coherence and and coherent back scattering effects. Using approaches that go beyond the CPA, like typical medium dynamical cluster approximation, the above effects can be taken into account [117].

Chapter 6

Non-Fermi-liquid behavior in disordered, correlated Fermi liquids

6.1 Introduction

There exist a number of metallic doped systems for which the Fermi liquid (FL) theory is clearly violated in transport and thermodynamic properties [7,118]. Most theoretical scenarios for non-Fermi liquid (nFL) behaviour require the proximity of some kind of singularity in the phase diagram, such as a quantum critical point (QCP) [4, 37, 119], Griffiths singularities (GS) close to magnetic instabilities [120] or van Hove singularities [121]. Other proposals for nFL include distribution of Kondo scales [8] and multichannel Kondo effect [122]. The nFL behaviour in a wide range of materials has been explained through these proposals.

Nevertheless, there is an expanding set of correlated systems for which the nFL behaviour does not fit the existing scenarios [7, 118, 123, 124]. For example, in

a recent study of the heavy fermion material $Ce_{1-x}La_xB_6$ [125], a resistivity of the form $\rho(T) = \rho_0 + AT^\alpha$ was found for $x \gtrsim 0.4$, where the non-universal and fractional exponent α, was found to be x-dependent. In the FL regime ($x \lesssim 0.4$), the coefficient of the quadratic term of the resistivity apparently diverges at the crossover from FL to nFL regime. The optical scattering rate of several U-based materials has been found to have a linear-in-frequency term [126]. A consistent theoretical explanation for such unusual nFL behaviour has not yet been found.

The $T = 0$ scattering rate in clean Fermi liquids has the form $\Gamma_{sc}(\omega) \stackrel{\omega\to 0}{\longrightarrow} a_2\omega^2$, The static effects of scattering by quenched substitutional disorder in Fermi-liquids contribute a constant term a_0 to $\Gamma_{sc}(\omega)$ [105, 106]. In this chapter, we show that dynamical effects of impurity scattering can give rise to the type of aforementioned unusual nFL behaviour. The $\Gamma_{sc}(\omega)$ is shown to acquire an additional linear in frequency term, $a_1\omega$. We also demonstrate that an excellent power-law description of $\Gamma_{sc}(\omega)$ is possible over two decades in ω, that yields a doping dependent exponent.

In heavy fermion systems such as $CeCu_6$, the substitution of Ce by La is of the Kondo hole (KH) type while that of Cu with Au is referred to as ligand-field type [105]. In present chapter, we will explicitly consider the KH type of substitution where the orbital energy of the f- level of the substituted non-magnetic atom is high enough that it decouples from the conduction band. Any type of random substitution breaks translational invariance, and leads to site and bond disorder. Random chemical substitution of the type $A_{1-x}B_x$ is usually incorporated through a probability distribution of the parameters in the Hamiltonian.

6.2 Model and formalism

The Hamiltonian for the periodic Anderson model (PAM), which is appropriate for heavy fermion systems, may be expressed in standard second-quantized notation as

$$H_{PAM} = -\sum_{\langle ij\rangle\sigma} t_{ij}\left(c^{\dagger}_{i\sigma}c_{j\sigma} + \text{h.c}\right) + \sum_{i} H_{ii} \tag{6.1}$$

where t_{ij} represents nearest neighbour hopping and $c_{i\sigma}$ is the conduction (c)-electron annihilation operator for site i and spin σ. Within dynamical mean field theory (DMFT) [16, 30], which is exact in the limit of infinite dimensions D, the hopping t_{ij} must be rescaled as $t_{ij} \propto t_*/\sqrt{D}$. The site-diagonal part, given by $H_{ii} = \epsilon_c \sum_\sigma c^{\dagger}_{i\sigma}c_{i\sigma} + \epsilon_f \sum_\sigma f^{\dagger}_{i\sigma}f_{i\sigma} + V(\sum_\sigma f^{\dagger}_{i\sigma}c_{i\sigma} + \text{h.c}) + Un_{fi\uparrow}n_{fi\downarrow}$ represents the orbital energies, hybridization between c- and f- electrons and the cost of double occupancy of the f- orbital respectively.

The coherent potential approximation (CPA) is the best single-site approach to study the interplay of disorder with interactions in strongly correlated systems [105, 127]. Even though the CPA ignores inter-site coherence and coherent back scattering effects (and hence Anderson localization), the effects of configurational averaging are well accounted. A dynamical CPA within DMFT has been formulated in section 5.2 of previous chapter 5 that takes into account the dynamical effects of impurity scattering. In this approach, the arithmetically averaged local c-electron Green's function called G_c^{CPA} is given by

$$G_c^{CPA}(\omega) = \frac{1-x}{\omega^+ - \epsilon_c - \Sigma_c - S(\omega)} + \frac{x}{\omega^+ - \epsilon_c - S(\omega)} \tag{6.2}$$

where the c- self-energy is $\Sigma_c(\omega) = V^2(\omega^+ - \epsilon_f - \Sigma_f(\omega))^{-1}$ and $\Sigma_f(\omega)$ is the f-self-energy. The dopant concentration is denoted by x, and $S(\omega)$ is Feenberg self-

energy [43] that represents the hybridization with the host. In the clean case ($x = 0$), the $S(\omega)$ is a functional of the local c- Green's function [44]. In the disordered case ($x \in (0, 1]$), the sum over all neighbouring sites in the Feenberg renormalized perturbation series [43] can be reduced, within DMFT, to a probabilistic averaging of the magnetic and Kondo hole Green's functions. Thus $S(\omega)$ becomes a functional of the averaged (CPA) Green's function, $S(\omega) = S[G_c^{CPA}]$. It is given by the condition that the CPA restores translational invariance, hence G_c^{CPA} is given by

$$\begin{aligned} G_c^{CPA}(\omega) &= \frac{1}{N}\sum_{\mathbf{k}} \frac{1}{\omega^+ - \epsilon_c - \epsilon_{\mathbf{k}} - \Sigma_c^{CPA}} \\ &= \mathcal{H}\left[\gamma(\omega)\right] = \frac{1}{\gamma(\omega) - S(\omega)} \end{aligned} \tag{6.3}$$

where $\gamma = \omega^+ - \epsilon_c - \Sigma_c^{CPA}$ and $\mathcal{H}[z] = \int_{-\infty}^{\infty} d\epsilon\, \rho_0(\epsilon)\,(z-\epsilon)^{-1}$ is the Hilbert transform of z with respect to the non-interacting density of states, $\rho_0(\epsilon)$. For the semi-elliptical density of states, $\rho_0(\epsilon) = \sqrt{1 - \epsilon^2/t_*^2}/(2\pi t_*)$, corresponding to the Bethe lattice, the Feenberg self-energy is simply given by $S(\omega) = t_*^2 G_c^{CPA}(\omega)/4$. This allows us to relate the CPA self-energy directly to the Σ_f as shown below.

As expressed by Eq. (6.2), the CPA Green's Function is given by

$$G_c^{CPA}(\omega) = \frac{1}{\Gamma - \Sigma_c^{CPA}} = \frac{1-x}{\Gamma - \Sigma_c} + \frac{x}{\Gamma}\,, \tag{6.4}$$

where $\Gamma = \omega^+ - \epsilon_c - S(\omega)$. From Eq. (6.4), the CPA self-energy can be extracted as

$$\Sigma_c^{CPA} = \frac{\Gamma\Sigma_c(1-x)}{\Gamma - x\Sigma_c}\,. \tag{6.5}$$

The above can be inverted to get Γ in terms of x, Σ_c and Σ_c^{CPA} as

$$\Gamma = \frac{x\Sigma_c\Sigma_c^{CPA}}{\Sigma_c^{CPA} - \Sigma_c(1-x)} \tag{6.6}$$

For a Bethe lattice,

$$S(\omega) = \frac{t_*^2}{4}G^{CPA}(\omega) = \frac{t_*^2}{4}\frac{1}{\Gamma - \Sigma_c^{CPA}}\,,$$

and for $t_* = 2$

$$S(\omega) = \frac{1}{\Gamma - \Sigma_c^{CPA}}\,. \tag{6.7}$$

Substituting $S(\omega) = \omega^+ - \epsilon_c - \Gamma$ in Eq. (6.7), we get

$$\omega^+ - \epsilon_c - \Gamma = \frac{1}{\Gamma - \Sigma_c^{CPA}}\,. \tag{6.8}$$

In Eq. (6.8), if we substitute for Γ, using Eq. (6.6), we will get an equation relating Σ_c^{CPA} to Σ_c. Alternatively if we substitute for Σ_c^{CPA}, using Eq. (6.5), we will get an equation for Γ in terms of Σ_c. In Eq. (6.8), substituting Γ using Eq. (6.6), we get

$$\begin{aligned}\Sigma_c^{CPA}\big(\Sigma_c - \Sigma_c^{CPA}\big)\Big[(\omega^+ - \epsilon_c)(\Sigma_c^{CPA} - \Sigma_c(1-x)) \\ -x\Sigma_c\Sigma_c^{CPA}\Big] - \big(\Sigma_c^{CPA} - \Sigma_c(1-x)\big)^2 = 0\end{aligned} \tag{6.9}$$

This is a cubic equation for Σ_c^{CPA}. Given the local self-energy $\Sigma_c(\omega)$, this equation may be used to obtain the CPA self-energy for any x. This equation is studied in detail in the next section.

6.3 Low frequency analysis

We have carried out a low frequency analysis of Eq. (6.9) in the concentrated ($x \to 0$) and dilute limits ($x \to 1$). Our basic premise is that the f- moments are completely screened, and hence have a local FL form of the self-energy, $\Sigma_f(\omega) \stackrel{\omega\to 0}{\longrightarrow} \Sigma_f(0) + \omega(1 - 1/Z) - iA'\omega^2$. Using this, the c- self-energy $\Sigma_c(\omega) = V^2[\omega^+ - \epsilon_f - \Sigma_f(\omega)]^{-1}$ can be Taylor expanded as

$$\Sigma_c(\omega) = \frac{V^2}{\omega - \epsilon_f - \Sigma_f(\omega)} \stackrel{\omega\to 0}{\longrightarrow} -\frac{V^2}{\epsilon_f^*}\left(1 + \frac{\omega}{Z\epsilon_f^*} + i\frac{A'}{\epsilon_f^*}\omega^2\right) \tag{6.10}$$

where the renormalized f- level, $\epsilon_f^* = \epsilon_f + \Sigma_f(0) \in \mathcal{R}\ \forall x$. The above may be used in Eq. (6.9) to find the low frequency form for $\Sigma_c^{CPA}(\omega)$.

Before delving into the details of the calculations, we summarize our main result. We find that

$$\Sigma_c^{CPA}(\omega) \stackrel{\omega\to 0}{\longrightarrow} S_0 + S_1\omega + S_2\omega^2 \tag{6.11}$$

where $\{S_i\}$ have finite imaginary parts that depend on x. The above expression, which shows that the CPA self-energy has a distinctly nFL form, embodied in the linear in ω term in the imaginary part, is the central result of our work. A finite linear term in the $\mathrm{Im}\Sigma_c^{CPA}$ in addition to the well-known residual ($\omega = 0$) and quadratic terms has broad consequences. First, since $\Sigma_c^{CPA} = V^2[\omega^+ - \epsilon_f - \Sigma_f^{CPA}]^{-1}$, the CPA self-energy of the f- electrons will also have an nFL form, even though the local self-energy has a standard FL form. It is easy to show using Eq. (6.2) that [105]

$$\mathrm{Im}\Sigma_f^{CPA}(\omega) = \frac{1}{1-x}\mathrm{Im}\Sigma_f(\omega) + \frac{x}{1-x}\mathrm{Im}\frac{V^2}{\omega^+ - \epsilon_c - S(\omega)}\,. \tag{6.12}$$

The above relation implies that the nFL part in the CPA self-energy arises through the contribution from the imaginary part of the self-consistently determined dynamical hybridization or the local potential. Second, the scattering rate, $\Gamma_{sc}(\omega) \propto -\mathrm{Im}\Sigma_c^{CPA}$ will also have a linear non-Fermi liquid type term in addition to the static potential scattering and the quadratic electron-electron scattering terms. As an inevitable consequence, transport quantities would display an nFL form. For example, the resistivity would have the low temperature form $\rho(T) = \rho(0) + A_R T + B_R T^2$, for a general particle-hole asymmetric case, as shown later (section 6.4). Thermodynamic quantities like the specific heat (C) will also be affected. A linear term in the imaginary part of the self-energy naturally leads to a $\omega \ln \omega$ term in the real part. From the expression of specific heat [71], it is easy to see that a $\ln T$ contribution would arise in C/T.

A straightforward generalization of Eq. (6.2) to the case of ligand-field substitution may be carried out [105]. A low frequency analysis similar to the one done above for KH disorder shows that the linear term would arise even for this case. Similarly, substitutional disorder in the Hubbard model [128] will also yield similar results, since the dynamical CPA equations for the local Green's function are exactly the same as Eqs. (6.2) and (6.3) with the Σ_c being replaced by the local self-energy of the interacting electrons. The CPA self-energy will thus have contributions from the FL self-energy and the dynamical local potentials which will again lead to a linear (in frequency) term in the scattering rate. Thus our findings have implication for transition metal oxides and other systems for which the Hubbard model is appropriate. Here, we have considered a binary distribution of site energies. A generalization to other discrete or continuous distributions can be made simply by generalizing Eq. (6.2) to a general distribution, $\mathcal{P}(\epsilon_{ci})$, in the

following way:

$$G_c^{CPA}(\omega) = \int_{-\infty}^{\infty} d\epsilon_{ci}\, \mathcal{P}(\epsilon_{ci}) \frac{1}{\omega^+ - \epsilon_{ci} - \Sigma_c - S(\omega)}\,. \tag{6.13}$$

The rest of the analysis proceeds in exactly the same way as for the binary distribution, and hence this will also yield similar nFL behaviour. Next, we find closed-form approximate expressions for the coefficients of the scattering rate (Eq. (6.11)) in the dilute and concentrated limits.

6.3.1 Analytical expressions for static and linear terms in scattering rate

We expect to find analytic solutions for the CPA self-energy, hence expanding $\Sigma_c^{CPA}(\omega) = S_0 + S_1\omega$, and using Eq. (6.10) in Eq. (6.9) with $(\omega^+ - \epsilon_c \to -\epsilon_c)$ for $\omega \to 0$, we get

$$\begin{aligned}
&(S_0 + S_1\omega)\left(\Sigma_{c0}(1 + A\omega) - S_0 - S_1\omega\right)\Big[(-\epsilon_c) \\
&(S_0 + S_1\omega - \Sigma_{c0}(1 + A\omega)(1 - x)) - x\Sigma_{c0}\,(1 + A\omega) \\
&(S_0 + S_1\omega)\Big] - \Big[S_0 + S_1\omega - \Sigma_{c0}(1 + A\omega)(1 - x)\Big]^2 = 0\,.
\end{aligned} \tag{6.14}$$

where $A = 1/(Z\epsilon_f^*)$. Substituting $\omega = 0$ in the above will yield an equation for the static contribution, namely $\Sigma_c^{CPA}(0)$. The coefficient of the linear in ω term may be found by collecting the linear terms. This will be done in the following subsections in the concentrated ($x \to 0$) and dilute ($x \to 1$) limits.

Concentrated limit $x \to 0$

After a lengthy and tedious, but straightforward calculation, we find the explicit dependence of $\{S_i\}$ (Eq. (6.11)) on x for a symmetric conduction band ($\epsilon_c = 0$). In the concentrated limit, $x \to 0$, the static part of Σ_c^{CPA} is given by (detail derivation in appendix C)

$$\begin{aligned} \mathrm{Re}(S_0) =& (1-x)\Sigma_{c0} + \frac{x(1-x)^2}{2}\Sigma_{c0}^3 \\ \mathrm{Im}(S_0) =& -x(1-x)\Sigma_{c0}^2 \times \left[1 - \frac{(1-x)^2}{4}\Sigma_{c0}^2\right]^{1/2}, \end{aligned} \tag{6.15}$$

where $\Sigma_{c0} = -V^2/\epsilon_f^*$. The $\mathrm{Im}(S_0)$ leads to a finite $T = 0$ residual resistivity. The coefficient of the linear term, $\mathrm{Im}(S_1)$ is given by

$$\mathrm{Im}(S_1) = \frac{x}{Z\epsilon_f^*}\mathrm{Im}\left[\frac{(\delta\Sigma_{c0})^2(\Sigma_{c0} - \delta\Sigma_{c0})}{(\delta\Sigma_{c0})^2 - 2(\delta\Sigma_{c0} - \Sigma_{c0})^2}\right]. \tag{6.16}$$

where $\delta\Sigma_{c0} = -\frac{(1-x)\Sigma_{c0}^2}{2}\left[(1-x)\Sigma_{c0} + 2i\right]$ is an $\mathcal{O}(1)$ number in the limit $x \to 0$. Thus, the nFL contribution is seen to be proportional to x at low dopant concentrations. It is also important to note that the quasiparticle weight (QpW) Z does not appear in the static part (Eq. (6.15)), but does appear in the dynamics, and arises purely because of the linear term in the FL form of the local self-energy, $\Sigma_f(\omega)$. Hence, the dynamical effects of potential scattering are responsible for nFL behaviour due to substitutional doping.

Dilute limit: $x \to 1$

In the dilute limit ($x \to 1$), the hybridization is determined through the non-interacting density of states, $\rho_0(\epsilon)$(detail derivation in appendix C). Hence we get

$$\Sigma_c^{CPA}(\omega) = \frac{V^2(1-x)}{\omega^+ - \epsilon_f - \Sigma_f(\omega) - x\Delta_0(\omega)}\,. \tag{6.17}$$

where $\mathrm{Im}\Delta_0(\omega) = -\pi V^2 \rho_0(\omega - \epsilon_c)$. In the strong coupling limit, and for low frequencies $\omega \lesssim \omega_L = ZV^2/t_*$, the $\rho_0(\omega)$ may be taken to be a constant, yielding the low frequency form of the CPA self-energy as:

$$\Sigma_c^{CPA} \xrightarrow{\omega \to 0} \frac{V^2(1-x)}{\frac{\omega}{Z} - \tilde{\epsilon}_f^* + ix\bar{\Delta}_0 + iA'\omega^2}\,. \tag{6.18}$$

where $\tilde{\epsilon}_f^* = \epsilon_f + \Sigma_f(0) + x\mathrm{Re}\Delta(0)$, and $\bar{\Delta}_0 = \pi V^2 \rho_0(-\epsilon_c)$. From the above expression, it is easy to see that in the dilute limit, all the three coefficients of Eq. (6.11) (divided by the number of magnetic atoms $(1-x)$) obtained through a Taylor expansion of Eq. (6.18) around $\omega = 0$ will remain non-zero. Thus for $x \to 1$, if either the effective f- level or the conduction band centre (ϵ_c) are non-zero, a linear term can be obtained in the temperature dependence of the resistivity, as discussed later in section 6.5.

6.3.2 General considerations for the quasiparticle weight

Before we discuss transport, we will briefly consider the behaviour of the QpWs as derived through the CPA quantities. This is important, because much of the low frequency and low temperature physics in clean systems can be gleaned through the renormalized non-interacting limit, where in the bare parameters such as the hybridization, V^2 or the bandwidth, t_* are renormalized by the QpW. As an ex-

ample of the consequence of such renormalization, the integrated spectral weight contained in the Drude peak of the optical conductivity is proportional to Z [40] in the clean system. In the disordered case, since the response functions are determined by the CPA self-energies, $\Sigma^{CPA}_{c/f}$, rather than the local self-energies, a clear picture must be obtained of the $Z^{CPA}_{c/f}$ defined as

$$\begin{aligned} \frac{1}{Z^{CPA}_{c/f}} &= \left(1 - \frac{\partial \Sigma^{CPA}_{c/f}(\omega)}{\partial \omega}|_{\omega\to 0}\right) \quad \text{and} \\ \frac{1}{Z^{CPA}_{c/f\,R}} &= \text{Re}\left(\frac{1}{Z^{CPA}_{c/f}}\right) \end{aligned} \tag{6.19}$$

From Eq. (6.11) and Eq. (6.16) above, it is clear that the QpWs defined above through the CPA self-energy would in general be complex. Furthermore, unlike the clean case, where the QpW for the c-electrons is proportional to that of the f-electrons, the Z^{CPA}_c and Z^{CPA}_f may behave entirely differently, because of the finite imaginary parts of either of these. This may be seen as follows. The CPA self-energy of the c- electrons is related to that of the f- electrons through

$$\Sigma^{CPA}_c = \frac{V^2}{\omega^+ - \epsilon_f - \Sigma^{CPA}_f} \overset{\omega\to 0}{\longrightarrow} \frac{V^2}{\omega/Z^{CPA}_f - \epsilon^*_f}\,, \tag{6.20}$$

where ϵ^*_f is a complex number. This implies the following for the corresponding QpWs:

$$\frac{1}{Z^{CPA}_c} = 1 + \frac{V^2}{(\epsilon^*_f)^2}\frac{1}{Z^{CPA}_f}\,. \tag{6.21}$$

which implies that the real part of the CPA c- electron QpW is dependent on both, the real and imaginary, parts of the Z^{CPA}_f.

6.4 Transport: Analytical considerations

In this section, we will discuss the consequences of an anomalous CPA self-energy (6.11) on transport quantities, namely resistivity and optical conductivity.

6.4.1 Resistivity

For the disordered PAM on a hypercubic lattice, the DC conductivity (within CPA) is given by Eq. (5.25)

$$\sigma_{DC}(T) = \sigma_0 \int_{-\infty}^{\infty} d\omega \left(-\frac{\partial n_F(\omega)}{\partial \omega}\right) \tau_{DC}(\omega) \tag{6.22}$$

$$\text{where} \quad \tau_{DC}(\omega) = \frac{\pi D_c^{CPA}(\omega)}{\gamma_I(\omega)} + 2\left(1-\gamma(\omega)\right) G_c^{CPA}(\omega)\,, \tag{6.23}$$

and $\gamma(\omega)$ is defined below Eq. (6.2), $\gamma_I = \mathrm{Im}\gamma = -\mathrm{Im}\Sigma_c^{CPA}$ and $n_F(\omega) = (\exp(-\omega/T)+1)^{-1}$ is the Fermi-Dirac distribution function (with T being the temperature). The local self-energy maintains a FL form in ω *and* T for all x, so even though the ω dependence of $\Sigma_{c/f}^{CPA}$ is anomalous, the explicit T dependence of $\Sigma_{c/f}^{CPA}$ will remain FL-like for all x. As an important consequence, since the $\tau_{DC}(\omega;T)$ depends on $\mathrm{Im}\Sigma_{c/f}^{CPA}$ (Eq. (6.23)), the frequency dependence of the scattering rate will be anomalous, but the temperature dependence will remain FL-like ($\sim T^2$). Such a $\tau_{DC}(\omega;T)$ when substituted in Eq. (6.22) will nevertheless yield a linear in temperature term in the DC conductivity as shown below.

We will revisit the clean case first, and then consider the disordered case. For $x = 0$, the $\tau_{DC}(\omega)$ of a clean FL may be approximated at the lowest (ω, T) by using the FL expansion of the local self-energy as

$$\tau_{DC}^{FL} \simeq \pi \frac{\pi D_c(0)}{a\omega^2 + bT^2}\,. \tag{6.24}$$

which is just a symmetric Lorentzian centred at $\omega = 0$, and a width$\sim T$. For an *even function* $\tau_{DC}(\omega)$, the integral in Eq. (6.22) will yield a conductivity that is an *even* function of temperature, because the derivative of the Fermi function is an even function of ω/T. Thus the resistivity will have the form $\rho_{DC}(T) = AT^2$.

In the presence of disorder, if only the static contribution to Σ_c^{CPA} is included, then the $\tau_{DC}(\omega)$ remains a symmetric Lorentzian, hence the conductivity will again be an even function of T, thus the resistivity will acquire the form $\rho_{DC}(T) = \rho_0 + AT^2$.

The nFL contribution embodied in the linear in T term arises from the dynamical, linear in ω contribution to the imaginary part of the CPA self-energy, as argued below. We have shown that the Σ_c^{CPA} acquires an nFL form for $x \neq 0$, where due to dynamical effects of impurity scattering, a linear in ω term arises (Eq. (6.11)). Since $\gamma_I = \mathrm{Im}(\omega^+ - \epsilon_c - \Sigma_c^{CPA}(\omega))$, the $\tau_{DC}(\omega)$ (Eq. (6.22)) is no longer an even function; in fact, it becomes a shifted Lorentzian of the form

$$\tau_{DC}^{nFL} \simeq \pi \frac{\pi D_c^{CPA}(0)}{a_0 + a_1\omega + a_2\omega^2 + bT^2}\,. \tag{6.25}$$

Now, for a strongly asymmetric $\tau_{DC}(\omega)$ (about $\omega = 0$), the conductivity will pick up linear in T terms. As a simple illustration, a square pulse form of $\tau_{DC}(\omega) = \theta(-\omega)\theta(\omega + |a|)$ yields $\sigma(T) = \sigma_0(1/2 + T/|a|)$, which is clearly a non-Fermi liquid form. Thus, we have argued that an nFL frequency dependence of the CPA self-energy will yield a nFL temperature dependence of DC conductivity.

6.4.2 Optical conductivity

In this section, we will explore the consequences of Kondo hole substitution on the low frequency features of the optical conductivity. The optical conductivity at zero

temperature within DMFT is given by [44]

$$\sigma(\omega) = \frac{\sigma_0}{\omega} \int_{-\infty}^{0} d\omega' \int_{-\infty}^{\infty} d\epsilon \rho_0(\epsilon) D(\omega', \epsilon) D(\omega + \omega', \epsilon) \tag{6.26}$$

where

$$D(\omega, \epsilon) = -\frac{1}{\pi} \mathrm{Im} \frac{1}{\gamma(\omega) - \epsilon} = \frac{\gamma_I/\pi}{(\gamma_R - \epsilon)^2 + \gamma_I} ,$$

$\gamma(\omega) = \gamma_R + i\gamma_I$ and $\gamma_I \geqslant 0$. Thus,

$$\begin{aligned} \sigma(\omega) =& \frac{\sigma_0}{\pi^2 \omega} \int_{-\infty}^{0} d\omega' \gamma_I(\omega') \gamma_I(\omega + \omega') \times \\ & \int_{-\infty}^{\infty} \frac{d\epsilon \rho_0(\epsilon)}{\left[(a_1 - \epsilon)^2 + b_1^2\right] \left[(a_2 - \epsilon)^2 + b_2^2\right]} , \end{aligned} \tag{6.27}$$

where $a_1 = \gamma_R(\omega)$, $b_1 = \gamma_I(\omega)$, $a_2 = \gamma_R(\omega + \omega')$ and $b_2 = \gamma_I(\omega + \omega')$. Assuming a wide, flat band for simplicity, $\rho_0(\epsilon) = \frac{1}{2W}\theta(W - |\epsilon|)$, we can carry out the integral over ϵ exactly to find

$$\sigma(\omega) = \frac{\sigma_0}{2\pi^2 \omega W} \int_{-\omega}^{0} d\omega' \frac{\pi Q}{2\sqrt{b_1 b_2}} (B + \frac{1}{B}) \tag{6.28}$$

where $A = \frac{a_1 - a_2}{2\sqrt{b_1\ b_2}}$ and $B^2 = \frac{b_1}{b_2}$. In the limit of $\omega \to 0$, the integrand may be Taylor expanded about the zero frequency limit using the Taylor expansion of the CPA self-energies. This finally yields the following expression for the zero temperature optical conductivity:

$$\sigma(\omega) = \frac{\sigma_0}{4\pi W \bar{\gamma}_I} \frac{1}{(\omega/2\bar{\gamma}_I Z_{cR}^{CPA})^2 + 1} \tag{6.29}$$

where $\bar{\gamma}_I = \gamma_I(0)$ is just the static part of the CPA self-energy.

We see from the above equation that the low frequency form of $\sigma(\omega; T = 0)$

is a Drude peak that has a Lorentzian shape. In the clean limit ($x = 0$) and at zero temperature, the imaginary part of $\Sigma_c^{CPA}(0)$ vanishes, and Z_{cR}^{CPA} is a finite positive number. Thus, we recover a Dirac delta functional form of the Drude peak in the clean limit. For finite x, the $\bar{\gamma}_I$ becomes finite, and hence the Drude peak broadens into a Lorentzian, with an integrated spectral weight remaining proportional to Z_{cR}^{CPA}. As will be seen later, the Z_{cR}^{CPA} crosses zero and becomes negative beyond a certain x_c, thus marking the complete destruction of the Drude peak, and hence a complete crossover to the single-impurity regime. At the present level of approximation in Eq. (6.28), we do not find a explicit contribution of the imaginary part of the QpW, i.e. Z_{cI}^{CPA}, although as shown in section 6.3.2, even the real part of the Z_c^{CPA} depends on the real *and* imaginary parts of Z_f^{CPA}. However, we conjecture that a higher order Taylor expansion in Eq. (6.28) will certainly lead to a manifestation of the Z_{cI}^{CPA} and a deviation from the Lorentzian form.

6.5 Results and discussion

The previous section was entirely focused on getting analytical insights into the manifestation of the anomalous form of the CPA self-energy in transport quantities. We were able to analyse the clean and dilute limits for the CPA self-energy in section 6.3, and find the low temperature and low frequency forms of the DC conductivity and optical conductivity respectively. In order to explore the nFL behaviour quantitatively in the full range of dopant concentration and at all energy scales, we have carried out detailed calculations for the Kondo hole disordered PAM within DMFT. The local moment approach (LMA) has been used to solve the effective impurity problem arising within DMFT. Within LMA, which is a diagrammatic perturbation theory based approach, the f- self-energy is ensured to

have a FL form, since adiabatic continuity to the non-interacting limit is imposed as a constraint. The reader is referred to chapter 1 and references within for the detailed implementation of the LMA within DMFT for the clean PAM. The coherence peak in the resistivity of clean heavy fermions is found to be at $T \sim \omega_L$, where $\omega_L = ZV^2/t_*$ is the low energy scale of the local Fermi liquid [40]. We focus on the frequency region $\omega \ll \omega_L$, since the nFL behaviour is found experimentally at temperatures much below the coherence peak [7, 118].

In the main panel of figure (6.1), we show (through fitting) that the $\mathrm{Im}\Sigma_c^{CPA}(\omega)$ does indeed have the quadratic polynomial form of Eq. (6.11) for all $x \in [0, 1]$. Nevertheless, we observe that a power law of the form $C + D\mathrm{sgn}(\omega)|\omega|^\alpha$ may also be fit upto a certain upper cutoff $\omega_c \sim \mathcal{O}(0.1\omega_L)$. This is shown in the inset of figure 6.1 (for $\omega > 0$). Hence the low temperature resistivity, as obtained through

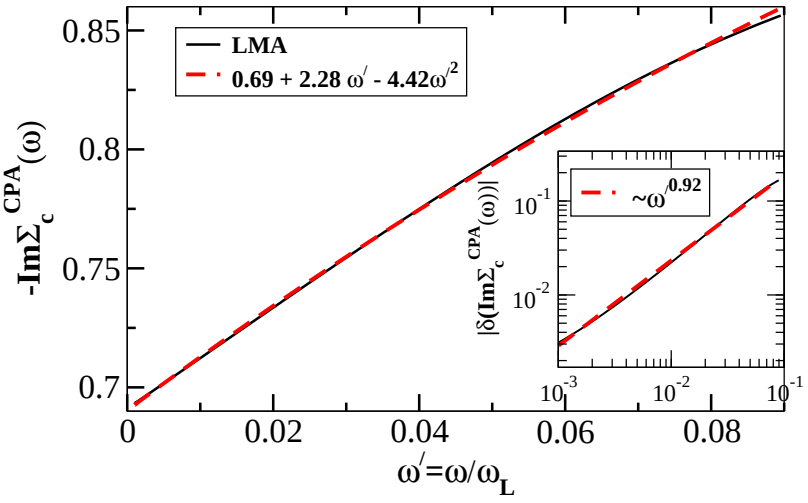

Fig. 6.1: In the main panel, the $\mathrm{Im}\Sigma_c^{CPA}(\omega)$ as a function of scaled frequency $\omega' = \omega/\omega_L$ has been shown with solid line for $x = 0.5$. The dashed line is the quadratic fit (Eq. 6.11). In the inset, the solid line represents $|\delta(\mathrm{Im}\Sigma_c^{CPA}(\omega))| = |\mathrm{Im}(\Sigma_c^{CPA}(\omega) - S_0)|$. The dashed line is a power law fit $D(\omega')^\alpha$, that yields a sub-linear $\alpha \simeq 0.92$. The model parameters for this calculation are $U = 5.30, V^2 = 0.6, \epsilon_c = 0.5$ and $\epsilon_f \sim -U/2$; the occupancies are $n_f \simeq 0.98, n_c \simeq 0.57$ and doping concentration is $x = 0.5$.

the scattering rate, is susceptible to a power law interpretation, with the exponent

being a function of disorder (see below). We have verified that the quadratic and power law fits are equally good for the entire range of doping.

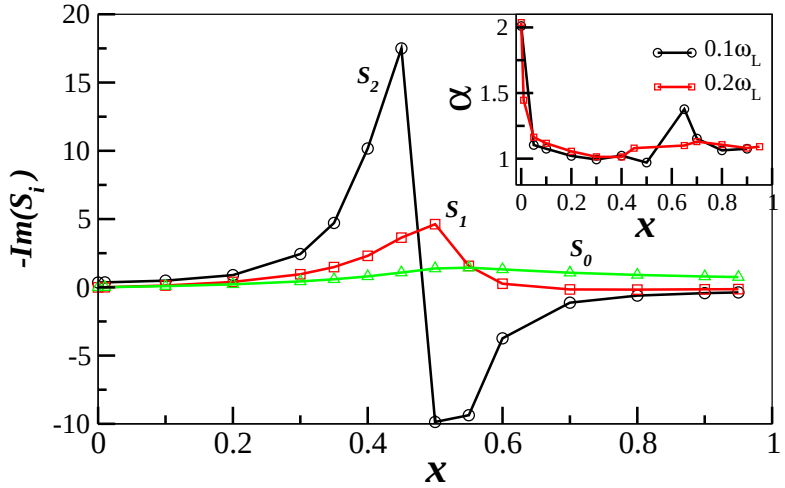

Fig. 6.2: The main panel shows $\mathrm{Im}(-S_0)$ (triangles), $\mathrm{Im}(-S_1)$ (squares) and $\mathrm{Im}(-S_2)$ (circles) per magnetic atom (Eq. 6.11). The inset shows the exponent α as a function of x, obtained through a power law fitting of the low frequency $\Im(\Sigma_c^{CPA}(\omega)$ for cutoff equal to $\sim 0.1\omega_L$ (circles) and $\sim 0.2\omega_L$ (squares). The model parameters for these results are the same as those for figure (6.1).

We now consider the dependence of the fitting parameters of the quadratic form of the CPA self-energy (Eq. (6.11)) on x. The $\mathrm{Im}(-\{S_i\})$ (Eq. (6.11)) per magnetic atom, as a function of x are shown in the main panel of figure (6.2). The first two ($i = 0, 1$) vanish for $x \to 0$, but remain finite for all other x including $x \to 1$. To explain this, we recapitulate that the coefficients, S_0 and S_1 develop finite imaginary parts due to disorder averaging in the CPA, which represents the effects of potential scattering. For any $x \neq 0$, Kondo holes will be in random positions, thus impurity scattering will be present, and will lead to the result seen in figure (6.2). The static part follows a Nordheim rule like behaviour, while the linear and quadratic coefficients show an apparent divergence before switching sign abruptly at $x \sim 1 - n_c \sim 0.43$. Although we see that the linear term is non-zero over the entire range of $x \in (0, 1]$, it becomes significant only in the neighbourhood

of $x \sim 1 - n_c$. We have also seen numerically (as well as from Eqs. (6.16) and (6.18)) that for a system which is close to the particle-hole symmetric limit, such nFL behaviour would be so weak that it would not show up. The inset of figure (6.2) shows the power law exponent α for two cutoff values, namely $\omega_c \sim 0.1\omega_L$ (circles) and $0.2\omega_L$ (squares). The power law fit depends sensitively on the cutoff ω_c, which is ambiguous. The exponent α is seen to be x-dependent and close to 1 over a large range of x. Many theoretical studies have pointed out the crossover of collective to single-impurity behaviour at $x \sim 1 - n_c$ [74, 107, 129], and we see from figure (6.2) that indeed dramatic changes could happen in the CPA quantities as x is tuned through this crossover.

Although the CPA quantities display remarkable non-monotonic behaviour on varying x, the local quantities are either monotonic with x or remain almost unchanged. This is shown in the figure (6.3), where we compare the occupancy (top panel) and the f- and c- quasiparticle weights (Z_f: middle panel and Z_c: bottom panel respectively) computed through local $\Sigma_{c/f}(\omega)$ (squares) with the corresponding CPA quantities (circles) using the real part of the CPA self-energies $\Sigma^{CPA}_{c/f}(\omega)$. The local quasiparticle weights show a weak dependence on increasing Kondo hole concentration, while the CPA quantities shows non-monotonic behaviour. The dip in Z^{CPA}_{fR} at $x \sim 1 - n_c$ would manifest as a peak in specific heat coefficient or the effective mass. The occupancy, calculated locally, remains almost unchanged, while the n^{CPA}_{tot}, given by $n_f + n_c - x$, decreases linearly as expected [105]. The c- electrons' CPA quasiparticle weight shows dramatic behaviour as a function of x. At small x, the Z^{CPA}_{cR} is positive, as expected from continuity to the clean limit. As x approaches $1 - n_c$, the Z^{CPA}_{cR} rapidly decreases and becomes negative at $x \gtrsim 1 - n_c$. The vanishing of the CPA QpW will have serious consequences for the optical conductivity. From Eq. (6.29), it is clear that the integrated spectral weight contained

within the Drude peak will vanish.

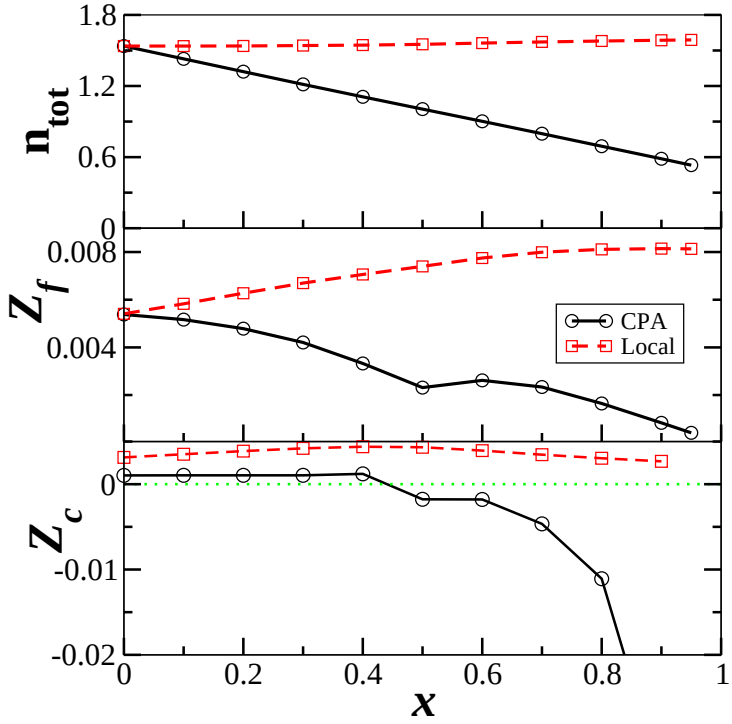

Fig. 6.3: Top panel: The total occupancy, $n_{tot} = n_f + n_c$ as calculated from the local Green's functions (filled squares) and the CPA Green's functions (filled circles) as a function of x. Middle Panel: The quasiparticle weight computed through the local f-self-energy (squares) and the real part of the CPA f- self-energy (circles) with increasing disorder value x. Bottom panel:The quasiparticle weight computed through the local c-self-energy (squares) and the real part of the CPA c- self-energy (circles) with increasing disorder value x. The model parameters are same as in figure (6.1). The green dotted line marks the zero line for the y-axis.

This is borne out by the $T = 0$ optical conductivity results shown in figure (6.4). With increasing x, the mid-infrared peak ($\sim 50\omega_L$) narrows and shifts to lower frequencies. As expected above, the low-frequency Drude peak feature is gradually replaced, with increasing x, by a flat featureless lineshape beyond $x \gtrsim 1 - n_c$.

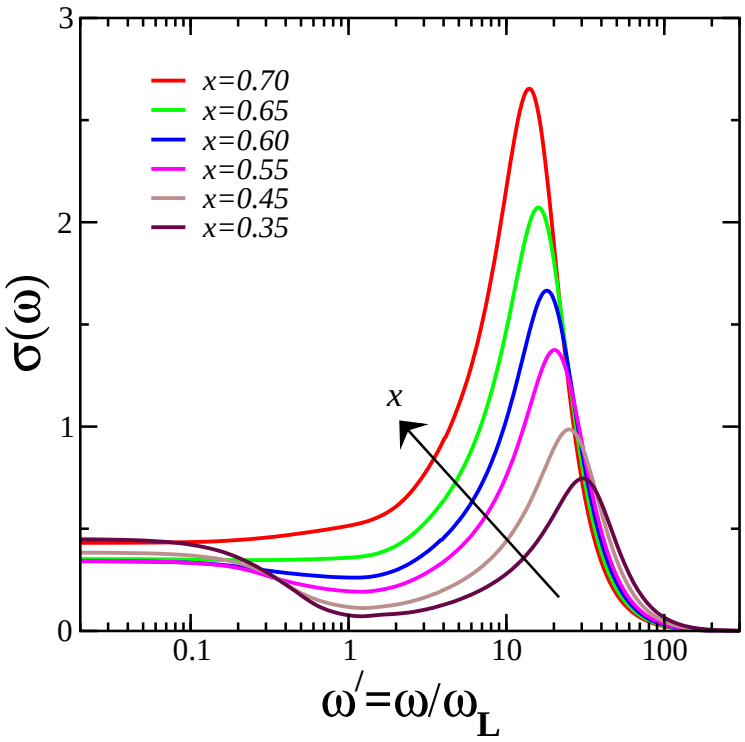

Fig. 6.4: The zero temperature optical conductivity as a function of scaled frequency $\omega' = \omega/\omega_L$ is shown for various values of doping x. The model parameters for this calculation are $U = 5.30, V^2 = 0.6, \epsilon_c = 0.7$ and $\epsilon_f \sim -U/2$; the occupancies are $n_f \simeq 0.97, n_c \simeq 0.43$.

6.5.1 nFL behaviour at finite temperature: Resistivity

We extend our discussion of the nFL at finite temperatures and explore low temperature behaviour of DC resistivity in the presence of disorder. It has been shown analytically in section (6.4.1) that due to disorder averaging, the functional form of DC resistivity picks an additional linear term in temperature and can be expressed as $a_0 + a_1 T + a_2 T^2$ for low temperatures. The analytical calculations presented in the previous sections have been carried out for concentrated and dilute limits only. In this section, we present our numerical results exploring nFL behaviour at finite temperature for full range of disorder concentration from $x = 0$ to 1. In the upper panel of figure 6.5, we have shown the variation of coefficient a_0, a_1, and

a_2 with varying disorder strengths for model parameters mentioned in the figure caption. The variation of coefficient of static part is barely Nordheim *like*, *i.e.* it does not follow Nordheim's rule ($\rho(0) \sim x(1-x)$). The coefficients of the linear and quadratic terms diverge at $x \sim 0.22$ ($x \sim (1-n_c)$). In the lower panel of figure 6.5, we show the DC resistivity for $x = 0.22$ for $0 < T/\omega_L \leq 0.1$ and fit a quadratic polynomial with coefficients mentioned in the legend of the figure. In the inset, we have done a power law fit $C + DT^{\alpha}$ to the resistivity ($x \sim 0.22$) with $\alpha \sim 1.04$. From the above observation, we conclude that power law interpretation, as done for CPA self-energy in section (6.5), holds good for finite temperature response functions too.

The nFL behaviour we find is within the framework of CPA. It is important to know if such behaviour is an artifact of CPA, or would it survive beyond CPA. To understand this in quantitative detail requires the use of an approach more sophisticated than CPA. While such a calculation is beyond the scope of this thesis, we will nonetheless argue qualitatively that the nFL behaviour that we find must manifest in experimental probes. The essence of our findings is that disorder-averaging of local Fermi-liquids induces a linear in ω term in the effective self-energy. Currently, one of the best methods to incorporate local correlations and disorder is the statistical-DMFT [8]. In this method, the local environment of each site is distinct, and is found self-consistently. If there are no unscreened spins, then this method yields all sites to be local Fermi liquids. Nevertheless, since any bulk experimental probe such as optical conductivity or DC resistivity, would be determined by disorder-averaged quantities, we conjecture that these quantities might exhibit nFL properties. In this context, even local optical probes such as infrared microscopy must be considered macroscopic, since the spatial resolution of such probes is $\sim$ 20 nm [130], which would represent a cluster of hundreds of

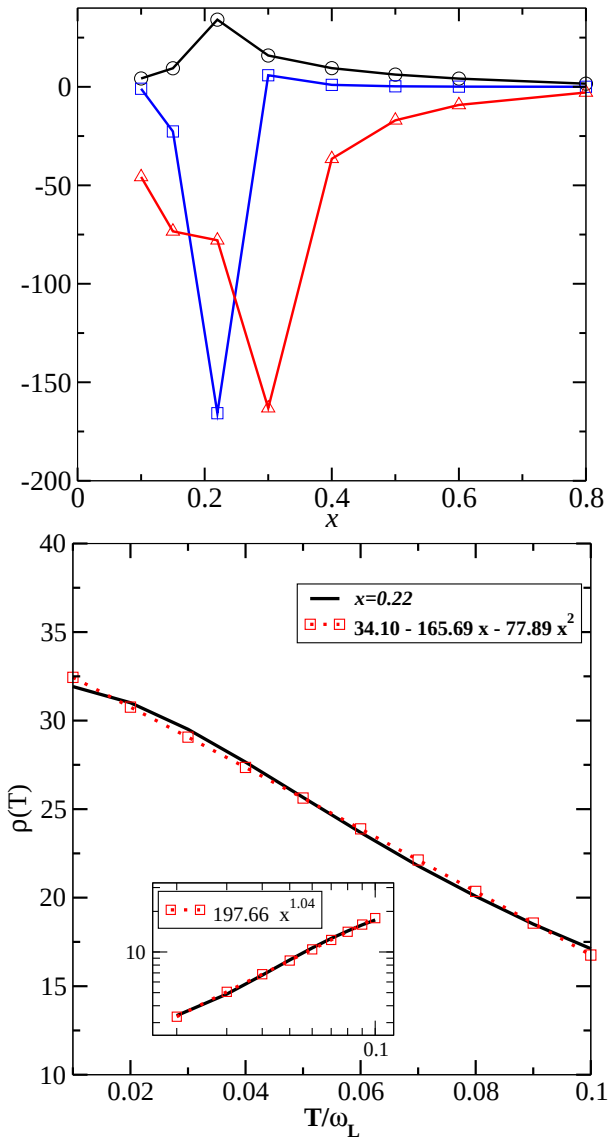

Fig. 6.5: Upper panel: Shows a_0 (circles), a_1 (squares) and a_2 (triangles) of the resistivity $\rho(T) = a_0 + a_1 T + a_2 T^2$. Lower panel: $\rho(T)$ as a function of scaled temperature T/ω_L has been shown with solid line for $x = 0.22$. The dashed line is the quadratic fit $a_0 + a_1 T + a_2 T^2$. In the inset, the solid line represents $|\delta(\rho(T))| = |\rho(T) - a_0)|$. The dashed line is a power law fit $D(T/\omega_L)^\alpha$, that yields almost linear fit given by $\alpha \simeq 1.04$. The model parameters are $U \sim 4.41, V^2 = 0.6, \epsilon_c = 0.2$ for which $n_f \sim 1$ $n_c \sim 0.2$

.

atoms. Only a strictly atomic level probe such as scanning tunneling microscopy, would however be able to distinguish between true nFL behaviour arising due to a breakdown of local Fermi liquid or a disorder-averaging induced nFL behaviour. A full statistical-DMFT calculation of the local Green's functions and self-energy and further calculation of response functions must be carried out to verify our conjecture.

6.6 Conclusions

There have been many recent theoretical studies of substitutional disorder in the Kondo lattice model or the PAM [74,105,107,129]. It was shown by Kaul and Vojta [107] that Griffiths singularities (GS) appear in a wide range of concentrations leading to nFL behaviour. The GS induced nFL has specific 'universal' signatures, albeit dependent on a non-universal exponent λ [120]. The authors also observe unscreened spins, which would imply that certain sites have a vanishing Kondo scale. Such a probability distribution of Kondo scales, where $P(T_K = 0)$ is finite, is also known to yield nFL behaviour [8]. In a recent work, a Lifshitz transition [129] is predicted to occur as a function of x, which could lead to nFL behaviour in the vicinity of the transition. The interaction of spin fluctuations with disorder close to a quantum critical point is also known to lead to power law behaviour, with a disorder-dependent exponent [119]. While inhomogeneities are natural and must be expected in any disordered system, instabilities such as a QCP and singularities such as GS are necessarily non-generic, i.e. they must occur only in specific regions of the phase diagram.

While such singularities do give rise to specific nFL behaviour, our work shows that nFL behaviour can be quite generic and can arise simply as a consequence of

disorder averaging. Hence, attributing the deviations from FL to a specific cause in disordered systems needs care. In $Ce_{1-x}La_xB_6$ for example, we suggest that a quadratic polynomial fit must be carried out for all x instead of a partial power law fit. We predict that the fit parameters would follow the behaviour shown in figure 6.2.

A distinct signature of the nFL behaviour we find is that it is a macroscopic effect, hence local probes such as scanning tunneling microscopy should find local Fermi liquid behaviour while macroscopic response functions would show nFL signatures. However, large area scans would be necessary to rule out unscreened spins or Griffiths singularities.

Appendix A

DC Conductivity

The expression for dynamical conductivity (hypercubic lattice) in [40] is

$$\sigma(\omega;T) = \frac{\sigma_0}{\omega}\int_{-\infty}^{\infty} d\omega_1 \left[n_F(\omega_1) - n_F(\omega_1+\omega)\right] \int_{-\infty}^{\infty} d\epsilon \rho_0(\epsilon) D^c(\omega;\omega_1) D^c(\epsilon;\omega+\omega_1). \tag{A.1}$$

where $D^c(\epsilon;\omega_1) = -\mathrm{Im}G^(\epsilon;\omega)/\pi; G^c(\epsilon;\omega) = (\gamma(\omega)-\epsilon)^{-1}$ and $\gamma(\omega)$ is defined below Eq. (2.4). The identity $\mathrm{Im}z_1\mathrm{Im}z_2 = \mathrm{Re}(z_1^* z_2 - z_1 z_2)/2$ for $z_1, z_2 \in \mathbb{C}$ may be used to get

$$D^c(\epsilon;\omega_1)D^c(\epsilon;\omega+\omega_1) = \frac{1}{2\pi^2}\mathrm{Re}\Big(\frac{G^{c*}(\omega+\omega_1) - G^c(\omega_1)}{\gamma^*(\omega+\omega_1)-\gamma(\omega)} - \frac{G^c(\omega+\omega_1) - G^c(\omega_1)}{\gamma^*(\omega+\omega_1)-\gamma(\omega)}\Big). \tag{A.2}$$

The integral over ϵ in equation Eq. (A.1) may be carried out to give the expression Eq. (2.5). The $\omega \to 0$ limit of Eq. (2.5) yields the dc conductivity. The second term can be simplified using the L'Hospital rule which in turn requires the knowledge of $dG^c(\omega)/d\gamma$, which we derive below. The c- Green's function is given by a

Hilbert transform over the Gaussian DOS. The result is expressed in terms of the complementary error function as [16]

$$G^c(\omega) = H[\gamma] = -is\sqrt{\pi}\exp(-\gamma^2)\mathrm{erfc}\,(-is\gamma) \tag{A.3}$$

where $s = sgn(\mathrm{Im}\gamma) = +1$ for the retarded functions considered here. The derivative of this with respect to γ is straightforward and is given as

$$\frac{dG^c(\omega)}{d\gamma} = -2\gamma G^c(\omega) - is\sqrt{(\pi)}\exp(-\gamma^2)(-is)\frac{d\mathrm{erfc}\,(x)}{dx}|_{x=-is\gamma}$$

$$= 2(1 - \gamma G^c(\omega))\,, \tag{A.4}$$

which gives Eq. (2.6).

Appendix B

Particle-hole symmetry

The extended periodic Anderson model (EPAM) is given by

$$\begin{aligned}\hat{H} =&\epsilon_c \sum_{i,\sigma} c^\dagger_{i,\sigma} c_{i\sigma} - t \sum_{(i,j),\sigma} c^\dagger_{i,\sigma} c_{j,\sigma} + V \sum_{i,\sigma} (f^\dagger_{i,\sigma} c_{i,\sigma} + H.c.) \\ &+ \sum_{i,\sigma} (\epsilon_f + \frac{U}{2} f^\dagger_{i,-\sigma} f_{i,-\sigma}) f^\dagger_{i,\sigma} f_{i,\sigma} + U_{fc} \sum_{i,\sigma,\sigma'} n^c_{i,\sigma} n^f_{i,\sigma'}. \end{aligned} \tag{B.1}$$

With the following particle hole transformation, Eq. (B.1) transforms to

$$\begin{aligned} c_{i,\sigma} \rightarrow c^\dagger_{i,\bar{\sigma}} \text{ and } c^\dagger_{i,\sigma} \rightarrow c_{i,\bar{\sigma}} \\ f_{i,\sigma} \rightarrow f^\dagger_{i,\bar{\sigma}} \text{ and } f^\dagger_{i,\sigma} \rightarrow f_{i,\bar{\sigma}} \end{aligned} \tag{B.2}$$

$$\begin{aligned}\hat{H}' =&\epsilon_c \sum_{i,\bar{\sigma}} c_{i,\bar{\sigma}} c^\dagger_{i\bar{\sigma}} - t \sum_{(i,j),\bar{\sigma}} c_{i,\bar{\sigma}} c^\dagger_{j,\bar{\sigma}} + V \sum_{i,\bar{\sigma}} (f_{i,\bar{\sigma}} c^\dagger_{i,\bar{\sigma}} + H.c.) \\ &+ \sum_{i,\bar{\sigma}} (\epsilon_f + \frac{U}{2} f_{i,\sigma} f^\dagger_{i,\sigma}) f_{i,\bar{\sigma}} f^\dagger_{i,\bar{\sigma}} + U_{fc} \sum_{i,\bar{\sigma},\bar{\sigma'}} f_{i,\bar{\sigma}} f^\dagger_{i,\bar{\sigma}} c_{i,\bar{\sigma'}} c^\dagger_{i,\bar{\sigma'}}. \end{aligned} \tag{B.3}$$

Using the commutation relations,$[c_{i\sigma}, c^{\dagger}_{j\sigma'}] = \delta_{ij,\sigma\sigma'}$ and $[f_{i\sigma}, f^{\dagger}_{j\sigma'}] = \delta_{ij,\sigma\sigma'}$ we can rewrite the above Hamiltonian as

$$\begin{aligned}\hat{H}' =&\epsilon_c \sum_{i,\sigma}(1 - c^{\dagger}_{i,\sigma}c_{i,\sigma}) + t\sum_{(j,i),\sigma}(c^{\dagger}_{j,\sigma}c_{i,\sigma} + H.c.) + V\sum_{i,\sigma}(f^{\dagger}_{i,\sigma}c_{i,\sigma} + H.c.) + \sum_{i,\sigma}\epsilon_f(1 - f^{\dagger}_{i,\sigma}f_{i,\sigma}) \\ &+ \sum_{i} U(1 - f^{\dagger}_{i,\downarrow}f_{i,\downarrow})(1 - f^{\dagger}_{i,\uparrow}f_{i,\uparrow}) + U_{fc}\sum_{i,\sigma,\sigma'}(1 - f^{\dagger}_{i,\sigma}f_{i,\sigma})(1 - c^{\dagger}_{i,\sigma'}c_{i,\sigma'})\,. \quad \text{(B.4)}\end{aligned}$$

With further simplification, we get

$$\begin{aligned}\hat{H}' =&\epsilon_c \sum_{i,\sigma} 1 + (-\epsilon_c - 2U_{fc})\sum_{i,\sigma} c^{\dagger}_{i,\sigma}c_{i,\sigma} - t\sum_{ij,\sigma}(c^{\dagger}_{i,\sigma}c_{i,\sigma} + H.c) + V\sum_{i,\sigma}(f^{\dagger}_{i,\sigma}c_{i,\sigma} + H.c) \\ &+ (-\epsilon_f - U - 2U_{fc})\sum_{i,\sigma} f^{\dagger}_{i,\sigma}f_{i,\sigma} + \sum_{i} 1 + U\sum_{i} f^{\dagger}_{i,\downarrow}f_{i,\downarrow}f^{\dagger}_{i,\uparrow}f_{i,\uparrow} \\ &+ U_{fc}\sum_{i,\sigma,\sigma'} f^{\dagger}_{i,\sigma}f_{i,\sigma}c^{\dagger}_{i,\sigma}c_{i,\sigma}\,. \quad \text{(B.5)}\end{aligned}$$

For the Hamiltonian to be invariant under particle-hole symmetry $\hat{H} = \hat{H}'$ (upto constant terms), the following conditions are obtained:

$$\begin{aligned}\epsilon_c &= -U_{fc} \quad \text{(B.6)} \\ \epsilon_f &= -(U_{fc} + \frac{U_{ff}}{2})\,. \quad \text{(B.7)}\end{aligned}$$

The multiorbital SIAM can be written in standard second quantized notation as

$$\begin{aligned}\hat{H} =&\sum_{\mathbf{k},m}\epsilon_{\mathbf{k}}c^{\dagger}_{\mathbf{k},m}c_{\mathbf{k},m} + \sum_{i}\big[V\sum_{\mathbf{k},\sigma}(f^{\dagger}_{i,\sigma}c_{\mathbf{k},i,\sigma} + h.c) \\ &+ \epsilon_f\sum_{\sigma} n^{f}_{i,\sigma} + Un_{i,\uparrow}n_{i,\downarrow}\big] + \frac{U'}{2}{\sum_{i,j}}' n_i n_j \quad \text{(B.8)}\end{aligned}$$

where $n_i = \sum_{\sigma} n_{i\sigma}$. We choose $V_{\mathbf{k}} = V$ for simplicity. The condition which makes

the Hamiltonian particle-hole invariant is found to be

$$\epsilon_f = -\frac{U}{2} - (N-1)U' \tag{B.9}$$

with which we can define an asymmetry parameter as $\eta = 1 + \frac{2\epsilon_f}{U+(2N-2)U'}$.

Appendix C

Low frequency analysis for concentrated and dilute limit

Concentrated limit $p \to 0$

Static term : $\omega = 0$

Starting from Eq. (6.14) and substituting $\omega = 0$, we get

$$S_0(\Sigma_{c0} - S_0)\Big[- \epsilon_c(S_0 - \Sigma_{c0}(1-x)) - x\Sigma_{c0}S_0\Big] \\ -(S_0 - \Sigma_{c0}(1-x))^2 = 0\,. \tag{C.1}$$

For a symmetric bare conduction band, $\epsilon_c = 0$, hence

$$S_0(\Sigma_{c0} - S_0)\Big[x\Sigma_{c0}S_0\Big] + (S_0 - \Sigma_{c0}(1-x))^2 = 0\,. \tag{C.2}$$

Assuming $S_0 = \Sigma_{c0}(1-x) + \delta\Sigma$ and neglecting $\mathcal{O}(\delta\Sigma)^3$ terms

$$x[\Sigma_{c0}(1-x) + \delta\Sigma]^2(x\Sigma_{c0} - \delta\Sigma)\Sigma_{c0} + (\delta\Sigma)^2 = 0\,. \tag{C.3}$$

Further, we get

$$\begin{aligned}(\delta\Sigma)^2\Big[1 + x^2\Sigma_{c0}^2 - 2x\Sigma_{c0}^2(1-x)\Big] + 2(\delta\Sigma)\Big[x^2\Sigma_{c0}^3(1-x) \\ -\frac{1}{2}p(1-x)^2\Sigma_{c0}^3\Big] + x^2(1-x)^2\Sigma_{c0}^4 = 0\,.\end{aligned} \tag{C.4}$$

If $(\delta\Sigma) \sim \mathcal{O}(x)$, then the above equation simplifies to

$$(\delta\Sigma)^2 - (\delta\Sigma)x(1-x)^2\Sigma_{c0}^3 + x^2(1-x)\Sigma_{c0}^4 = 0\,. \tag{C.5}$$

This can be easily solved to get

$$(\delta\Sigma) = \frac{x(1-x)^2\Sigma_{c0}^3 \pm \sqrt{x^2(1-x)^4\Sigma_{c0}^6 - 4x^2(1-x)^2\Sigma_{c0}^4}}{2}\,. \tag{C.6}$$

The imaginary part can only arise through from the square root term, hence

$$\Im(\delta\Sigma) \simeq -x(1-x)\Sigma_{c0}^2\Big[1 - \frac{(1-x)^2\Sigma_{c0}^2}{4}\Big]^{\frac{1}{2}}\,, \tag{C.7}$$

while

$$\mathrm{Re}(\delta\Sigma) = \frac{x(1-x)^2\Sigma_{c0}^3}{2}\,. \tag{C.8}$$

Thus for a BL and $\epsilon_c = 0$, the static CPA self-energy is given in $p \to 0$ limit by

$$\begin{aligned} S_0 =& \Sigma_{c0}(1-x) + \frac{x(1-x)^2\Sigma_{c0}^3}{2} \\ & - ix(1-x)\Sigma_{c0}^2\left[1 - \frac{(1-x)^2\Sigma_{c0}^2}{4}\right]^{\frac{1}{2}} . \end{aligned} \tag{C.9}$$

Dynamics; Linear term

Using $\epsilon_c = 0$ and $x \to 0$ in Eq. (6.14) and collecting the linear term only

$$\begin{aligned} & \bar{S_1}\Big[xS_0^2\Sigma_{c0} - 2(S_0 - \Sigma_{c0})\Big] \\ & = -\Big[- x\Sigma_{c0}^2 S_0^2 - x\Sigma_{c0}S_0 \\ & (\Sigma_{c0} - S_0) + 2\Sigma_{c0}(S_0 - \Sigma_{c0})\Big] . \end{aligned} \tag{C.10}$$

where $\bar{S_1} = Z\epsilon_f^* S_1$ Using Eq.(C.3)

$$\begin{aligned} & \bar{S_1}\left[\frac{-(\delta\Sigma)^2}{\Sigma_{c0} - S_0} - 2(S_0 - \Sigma_{c0})\right] \\ & = -\left[(\delta\Sigma)^2 + \frac{(\delta\Sigma)^2\Sigma_{c0}}{\Sigma_{c0} - S_0} + 2(S_0 - \Sigma_{c0})\right] \end{aligned} \tag{C.11}$$

with $S_0 = \Sigma_{c0}(1-x) + \delta\Sigma$

$$\text{and } \delta\Sigma \cong \frac{-x(1-x)\Sigma_{c0}^2}{2}[(1-x)\Sigma_{c0} + 2i] . \tag{C.12}$$

From Eq (6.15), we get

$$S_0 - \Sigma_{c0} \simeq -x\Sigma_{c0}\left[1 - \frac{(1-x)^2\Sigma_{c0}^2}{2} + i(1-x)\Sigma_{c0}^2\right] . \tag{C.13}$$

The x dependence of $\bar{S_1}$ can be extracted as

$$\bar{S_1}\left[\frac{-x^2(\delta\bar{\Sigma})^2}{x(\Sigma_{c0}-\delta\bar{\Sigma})}-2x(\delta\bar{\Sigma}-\Sigma_{c0})\right] \\ =-\left[x^2(\delta\bar{\Sigma})^2+\frac{-x^2(\delta\bar{\Sigma})^2\Sigma_{c0}}{x(\Sigma_{c0}-\delta\bar{\Sigma})}+2x\Sigma_{c0}(\delta\bar{\Sigma}-\Sigma_{c0})\right] \quad \text{(C.14)}$$

Simplifying, we get

$$\bar{S_1}=\Sigma_{c0}+x\frac{\delta\bar{\Sigma}^2(\Sigma_{c0}-\delta\bar{\Sigma})}{(\delta\bar{\Sigma}^2)-2(\delta\bar{\Sigma}-\Sigma_{c0})^2}\,. \quad \text{(C.15)}$$

Thus for $\Sigma_c^{CPA}(\omega)=S_0+S_1\omega$

$$\mathrm{Im}(S_1)\simeq\frac{x}{Z\epsilon_f^*}\mathrm{Im}\left[\frac{\delta\bar{\Sigma}^2(\Sigma_{c0}-\delta\bar{\Sigma})}{(\delta\bar{\Sigma}^2)-2(\delta\bar{\Sigma}-\Sigma_{c0})^2}\right], \quad \text{(C.16)}$$

and

$$\mathrm{Re}(S_1)=\frac{1}{Z\epsilon_f^*}\left[\Sigma_{c0}+x\mathrm{Re}\left[\frac{\delta\bar{\Sigma}^2(\Sigma_{c0}-\delta\bar{\Sigma})}{(\delta\bar{\Sigma}^2)-2(\delta\bar{\Sigma}-\Sigma_{c0})^2}\right]\right]. \quad \text{(C.17)}$$

$f-$ CPA self-energy in $x\to 1$

In the concentrated ($x\to 0$) limit, the CPA self-energies must coincide with the local self-energy. Thus the coefficient of the w^2 term in the $x\to 0$ limit arises purely through $\mathrm{Im}\Sigma_f(\omega)$ and hence must be negative. While in the other extreme ($x\to 1$), the CPA self-energy for f-electron is given by

$$\omega-\epsilon_f-\Sigma_f^{CPA}=\frac{1}{1-x}(\omega-\epsilon_f-\Sigma_f)-\frac{pV^2}{1-p}g_0(\omega)\,. \quad \text{(C.18)}$$

where $g_0(\omega) = \frac{1}{\omega^+ - \epsilon_c - S(\omega)} = \mathcal{H}(\omega^+ - \epsilon_c)$ and $\mathcal{H}(z)$ is Hilbert transform of z with respect to the non-interacting density of state $\rho_0(\epsilon)$. Thus the CPA self-energy for c-electrons will be

$$\Sigma_c^{CPA} = \frac{V^2(1-x)}{\omega^+ - \epsilon_f - \Sigma^f(\omega) - x\Delta_0}\,, \tag{C.19}$$

where $\Delta(\omega) = V^2 g_0(\omega)$. Expanding $\Sigma^f(\omega)$, we can write

$$\Sigma_c^{CPA} \cong \frac{V^2(1-x)}{\frac{\omega}{Z} - \tilde{\epsilon_f^*} - x\bar{\Delta}_0} \tag{C.20}$$

where $\tilde{\epsilon_f^*} = \epsilon_f + \Sigma_f(0) + p\Delta_R(0)$ and $\Delta_0 = \pi V^2 \rho_0(\omega - \epsilon_c)$. Using a Taylor expansion of Σ_c^{CPA} from Eq. (C.20), static, linear and quadratic terms may be easily found.

Bibliography

[1] N. Grew and steglich F., *Handbook on the Physics and Chemistry of Rare Earths*, 14 ed k a gschneider jr. and l l eyring ed. (Elsevier, Amsterdam, 1991).

[2] P. Wacher, *Handbook on the Physics and Chemistry of Rare Earths*, 19 ed k a gschneider and l l eyring ed. (Elsevier, Amsterdam, 1994).

[3] A. C. Hewson, *The Kondo Problem to Heavy Fermions* (Cambridge University Press, Cambridge, 1993).

[4] P. Coleman, *Physica* B **259-261**, 353 (1999).

[5] P. Gegenwart *et al.*, Nature Physics **4**, 186 (2008).

[6] Y. Onishi and K. Miyake, *J. Phys. Soc. Japan* **69**, 3955 (2000).

[7] G. R. Stewart, *Rev. Mod. Phys.* **73**, 797 (2001).

[8] V. Dobrosavljevic and all, *Conductor Insulator Quantum Phase Transitions* (Oxford University Press, Oxford, 2013).

[9] G. Aeppli and Z. Fisk, *Comm. Condens. Matter Phys.* **16**, 155 (1992).

[10] C. M. Varma, *Rev. Mod. Phys.* **48**, 219 (1976).

[11] G. R. Stewart, *Rev. Mod. Phys.* **56**, 755 (1984).

[12] P. S. Risebourough, *Adv. Phys.* **49**, 257 (2000).

[13] L. Degiorgi, *Rev. Mod. Phys.* **71**, 687 (1999).

[14] K. Anders *et al.*, *Phys. Rev. Lett.* **35**, 1975 (1975).

[15] C. Kittel, *Introduction to Solid State Physics*, 7 ed. (John Wiley and Sons, New york, 1996).

[16] A. Georges *et al.*, *Rev. Mod. Phys.* **68**, 13 (1996).

[17] P. W. Anderson, *Phys. Rev.* **124**, 41 (1961).

[18] J. R. Schrieffer and P. A. Wolf., *Phys. Rev.* **149**, 491 (1966).

[19] A. M. Tsvelik and P. B. Wiegmann, *Adv. Phys.* **32**, 453 (1983).

[20] H. R. Krisnamurthy *et al.*, *Phys. Rev.* B **21**, 1003 (1980).

[21] D. E. Logan *et al.*, *J. Phys.: Condens. Matter* **10**, 2673 (1998).

[22] M. T. Glossop and D. E. Logan, *J. Phys.: Condens. Matter* **14**, 6737 (2002).

[23] H. J. Leder and B. Muhlschlegel, *Z. Physik.* B **29**, 341 (1978).

[24] G. Czycholl and H. J. Leder, *Z. Physik.* B **44**, 1981 (1981).

[25] T. M. Rice and K. Ueda, *Phys. Rev. Lett.* **55**, 995 (1985).

[26] P. Coleman, *Phys. Rev.* B **28**, 5255 (1983).

[27] P. Coleman, *Phys. Rev.* B **35**, 5072 (1987).

[28] N. Read and D. M. Newns, *Adv. Phys.* **36**, 799 (1987).

[29] I. N. Karnaukhov, *Phys. Rev.* B **56**, R4314 (1997).

[30] T. Pruschke *et al.*, *Adv. Phys.* **44**, 187 (1995).

[31] J. L. Smith and Q. Si, arXiv:cond-mat/9705140v1 (1997).

[32] T. Maier *et al.*, *Rev. Mod. Phys.* **77**, 1027 (2005).

[33] R. Scalettar *et al.*, *Phys. Rev.* B **31**, 7316 (1985).

[34] T. Pruschke *et al.*, *Phys. Rev.* B **61**, 12799 (2000).

[35] M. Jarrell, *Phys. Rev.* B **51**, 7429 (1995).

[36] M. J. Rozenberg, *Phys. Rev.* B **52**, 7369 (1995).

[37] N. S. Vidhyadhiraja *et al.*, *Eur. Phys. Lett.***49**, 459 (2000).

[38] N. S. Vidhyadhiraja and D. E. Logan, *Eur. Phys. J.* B **39**, 313 (2004).

[39] S. J. Sun *et al.*, *Phys. Rev.* B **48**, 16127 (1993).

[40] D. E. Logan and N. S. Vidhyadhiraja, *J. Phys.: Condens. Matter* **17**, 2935 (2005).

[41] N. S. Vidhyadhiraja and D. E. Logan, *J. Phys.: Condens. Matter* **17**, 2959 (2005).

[42] P. Sun and G. Kotliar, *Phys. Rev. Lett.* **95**, 016402 (2005).

[43] E. N. Economou, *Green's Functions in Quantum Mechanics* (Springer, Berlin, 2006).

[44] P. Kumar and N. S. Vidhyadhiraja, *J. Phys.: Condens. Matter* **23**, 485601 (2011).

[45] R. Bulla *et al.*, *J. Phys.: Condens. Matter* **12**, 4899 (2000).

[46] V. E. Smith, Ph.D. thesis, Balliol College, Oxford, University of Oxford, UK, 2004.

[47] D. E. Logan *et al.*, *J. Phys.: Condens. Matter* **14**, 3605 (2002).

[48] A. V. Pushkov *et al.*, *J. Phys.: Condens. Matter* **8**, 10049 (1996).

[49] N. S. Vidhyadhiraja and P. Kumar, *Phys. Rev.* B **88**, 195120 (2013).

[50] P. Kumar and N. S. Vidhyadhiraja, *J. Phys. Soc. Japan* Suppl (2013).

[51] Z. Fisk *et al.*, *Physica* B **223**, 409 (1996).

[52] D. Jaccard *et al.*, *Rev. High Pressure Sci. Technol* **7**, 412 (1998).

[53] M. Ocko *et al.*, *Phys. Rev.* B **64**, 195107 (2001).

[54] E. Bauer *et al.*, *Phys. Rev.* B **48**, 15873 (1993).

[55] T. Kagayama *et al.*, *Physica* B **230**, (1997).

[56] T. Iizuka *et al.*, *J. Phys. Soc. Japan* **79**, 123703 (2010).

[57] H. Yuan *et al.*, *Phys. Rev.* B **74**, 212403 (2006).

[58] G. Knebel *et al.*, *J. Phys.: Condens. Matter* **13**, 10935 (2001).

[59] M. Matsunami *et al.*, *Phys. Rev. Lett.* **103**, 237202 (2009).

[60] D. Kaczorowski and A. Slebarski, *Phys. Rev.* B **81**, 214411 (2010).

[61] D. T. Adroja and B. D. Rainford, *J. Magn. Magn. Mater.* **119**, 54 (1992).

[62] D. Kaczorowski *et al.*, *J. Phys.: Condens. Matter* **22**, 215601 (2010).

[63] J. G. Sereni, *J. Phys. F: Metal Phys.* **10**, 2831 (1980).

[64] W. Franz *et al.*, *Z. Physik* B **31**, 7 (1978).

[65] W. Franz *et al.*, *Journal De Physique* **c5**, 342 (1979).

[66] L. Chandran *et al.*, *J. Phys.: Condens. Matter* **4**, 7067 (1992).

[67] N. Grewe *et al.*, *Z. Phys. B: Condens. Matt.* **71**, 75 (1988).

[68] D. L. Cox and N. Grewe, *Z. Phys. B: Condens. Matt.* **71**, 321 (1988).

[69] P. Coleman, *Phys. Rev.* B **29**, 3035 (1984).

[70] N. S. Vidhyadhiraja *et al.*, *J. Phys.: Condens. Matter* **15**, 4045 (2003).

[71] A. Gilbert *et al.*, *J. Phys.: Condens. Matter* **19**, 106220 (2007).

[72] J. K. Freericks and V. Zlatic, *Phys. Rev.* B **64**, 245118 (2001).

[73] B. H. Bernhard and B. Coqblin, *Physica* B **404**, 3021 (2009).

[74] S. Watanabe *et al.*, *J. Phys. Soc. Japan* **75**, 043710 (2006).

[75] T. Sugibayashi and D. S. Hirashima, *J. Phys. Soc. Japan* **75**, 244 (2006).

[76] E. R. Ylvisaker *et al.*, *Phys. Rev. Lett.* **102**, 246401 (2009).

[77] K. Shin-ichi, *Phys. Rev.* B **80**, 073103 (2009).

[78] T. Iizuka *et al.*, *J. Phys. Soc. Japan* **79**, 123703 (2010).

[79] A. D. Christianson *et al.*, *Phys. Rev.* B **66**, 054410 (2002).

[80] C. Mazumdar *et al.*, *Phys. Rev.* B **46**, 9009 (1992).

[81] S. L. Bud'ko *et al.*, *J. Phys.: Condens. Matter* **10**, 8815 (1998).

[82] A. Fuse *et al.*, *Physica* B **281& 282**, 175 (2000).

[83] J. D. Thompson and Z. Fisk, *Phys. Rev.* B **31**, 389 (1985).

[84] Z. Hossain *et al.*, *Phys. Rev.* B **72**, 094411 (2005).

[85] J. Custers *et al.*, Nature **424**, 524 (2003).

[86] H. Q. Yuan *et al.*, Science **302**, 2104 (2003).

[87] P. Coleman, Nature Material 185 (2012).

[88] Y. Onishi and K. . Miyake, *J. Phys. Soc. Japan* **69**, 3955 (2000).

[89] A. . C. Hewson, *Solid State Communications* **22**, 379 (1977).

[90] Y. Saiga *et al.*, *J. Phys. Soc. Japan* **77**, 114710 (2008).

[91] T. Yoshida and N. Kawakami, *Phys. Rev.* B **85**, 235148 (2012).

[92] J. P. Rueff *et al.*, *Phys. Rev. Lett.* **106**, 186405 (2011).

[93] C. Grenzebach *et al.*, *Phys. Rev.* B **74**, 195119 (2006).

[94] R. Sato *et al.*, *J. Phys. Soc. Japan* **73**, 1864 (2008).

[95] A. Koga *et al.*, *Phys. Rev.* B **77**, 045120 (2008).

[96] M. R. Galpin *et al.*, *J. Phys.: Condens. Matter* **21**, 375602 (2009).

[97] Y. Onuki *et al.*, *J. Phys. Soc. Japan* **54**, 1964 (1985).

[98] N. Sato *et al.*, *J. Phys. Soc. Japan* **54**, 1923 (1985).

[99] U. Kohler, *Phys. Rev.* B **77**, 04412 (2008).

[100] H. v. Lohneysen H., *Phys. Rev. Lett.* **72**, 3262 (1994).

[101] B. Andraka and G. R. Stewart, *Phys. Rev.* B **47**, 3208 (1993).

[102] V. Janis and D. Vollhardt, *Phys. Rev.* B **46**, 15712 (1992).

[103] V. Dobrosavljevic and G. Kotliar, *Phys. Rev. Lett.* **71**, 3218 (1992).

[104] P. Ulmke *et al.*, *Phys. Rev.* B **51**, 10411 (1995).

[105] C. Grenzebach *et al.*, *Phys. Rev.* B **77**, 115125 (2008).

[106] T. Mutou, *Phys. Rev.* B **64**, 245102 (2001).

[107] R. K. Kaul and M. Vojta, *Phys. Rev.* B **75**, 132407 (2007).

[108] S. Burdin and P. fulde, *Phys. Rev.* B **76**, 104425 (2007).

[109] S. Wembter, *Physica* B **230-232**, 463 (1997).

[110] T. A. Costi, *Physica* B **199-200**, 81 (1994).

[111] N. W. Ashcroft and N. D. Mermin, *Solid state physics* (Harcourt, orlando, 1976).

[112] S. V. Dordevic *et al.*, *Phys. Rev. Lett.* **86**, 684 (2001).

[113] S. Kimura *et al.*, *Phys. Rev.* B **74**, 132408 (2006).

[114] H. Okumura *et al.*, *J. Phys. Soc. Japan* **73**, 2045 (2003).

[115] T. A. costi *et al.*, *J. Phys.: Condens. Matter* **6**, 2519 (1994).

[116] M. S. Kim *et al.*, *J. Phys. Soc. Japan* **75**, 064704 (2006).

[117] M. Jarrell and H. R. Krishnamurthy, *Phys. Rev.* B **63**, 125102 (2000).

[118] M. B. Maple *et al.*, *J. Low Temp. Phys.* **161**, 4 (2010).

[119] A. Rosch, *Phys. Rev. Lett.* **82**, 4280 (1999).

[120] D. Nozadze and T. Vojta, *Journal of Physics: Conference Series* **391**, 012162 (2011).

[121] S. Schmitt, *Phys. Rev.* B **82**, 155126 (2010).

[122] A. M. Chang and J. C. Chen, *Rep. Prog. Phys.* **72**, 096501 (2009).

[123] J. Paglione *et al.*, Nature physics **3**, 703 (2007).

[124] C. M. Varma *et al.*, *Physics Reports* **361**, 267417 (2002).

[125] S. Nakamura *et al.*, *Phys. Rev. Lett.* **97**, 237204 (2006).

[126] L. Degiorgi *et al.*, *Phys. Rev.* B **54**, 6065 (1996).

[127] M. Potthoff and M. Balzer, *Phys. Rev.* B **75**, 125112 (2007).

[128] M. Laad *et al.*, *Phys. Rev.* B **64**, 195114 (2001).

[129] S. Burdin and C. Lacroix, *Phys. Rev. Lett.* **110**, 226403 (2013).

[130] M. M. Qazilbash *et al.*, Science **318**, 1750 (2007).